

# Adaptive Strategies for Exponential Shape Functions in Fracture Phase Field Models

vom Fachbereich Maschinenbau und Verfahrenstechnik  
der Rheinland-Pfälzischen Technischen Universität Kaiserslautern-Landau  
zur Verleihung des akademischen Grades  
Doktor-Ingenieur (Dr.-Ing.)  
genehmigte Dissertation

von  
M.Eng. Darius Olesch  
aus Landshut

Hauptreferent: Prof. Dr.-Ing. Ralf Müller  
Korreferent: Prof. Dr.-Ing. Wolfgang Dornisch  
Vorsitzender: Prof. Dr.-Ing. Eberhard Kerscher  
Dekan: Prof. Dr. rer. nat. Roland Ulber

Tag der Einreichung: 23.05.2024  
Tag der mündlichen Prüfung: 09.12.2024

Pentling, 2024

D 386

**Herausgeber**

Lehrstuhl für Technische Mechanik  
Rheinland-Pfälzische Technische Universität Kaiserslautern-Landau  
Gottlieb-Daimler-Straße  
Postfach 3049  
67653 Kaiserslautern

© Darius Olesch

Ich danke der “Prof. Dr. Hans Georg und Liselotte Hahn Stiftung” für die finanzielle Unterstützung bei der Drucklegung.

**Druck**

Rheinland-Pfälzische Technische Universität Kaiserslautern-Landau  
Hauptabteilung 5/ Bau-Technik-Energie  
Abteilung 5.6 Foto-Repro-Druck

Alle Rechte vorbehalten, auch das des auszugsweisen Nachdrucks, der auszugsweisen oder vollständigen Wiedergabe (Photographie, Mikroskopie), der Speicherung in Datenverarbeitungsanlagen und das der Übersetzung.

ISBN 978-3-942695-26-8

# Vorwort

Die vorliegende Arbeit entstand während meiner Tätigkeit als wissenschaftlicher Mitarbeiter am Lehrstuhl für Technische Mechanik der Technischen Universität Kaiserslautern.

Als Erstes möchte ich mich bei Dr.-Ing. Charlotte Kuhn sowie bei Prof. Dr.-Ing. Ralf Müller für die Ermöglichung dieser Arbeit und die hervorragende Betreuung bedanken.

Genauso danke ich Prof. Dr.-Ing. Eberhard Kerscher für die Übernahme des Vorsitzes sowie Prof. Dr.-Ing. Wolfgang Dornisch für die Übernahme der Berichterstattung.

Allen meinen Kollegen am LTM danke ich für die tolle Arbeitsatmosphäre, ihre Hilfsbereitschaft und die schöne Zeit in Kaiserslautern. Den Mitgliedern des SPP 1748 danke ich für die interessanten Projekttreffen.

Meiner Familie danke ich für die Unterstützung. Einem besonderen Dank gilt meiner Frau Parisa, die mich darüber hinaus unterstützt hat. Sowie meiner Tochter Pariya und meinem Sohn Parham, die mich durch die Ziellinie begleitet haben.

## Zusammenfassung

Brüche sind eine Erscheinungsform entstehender Oberflächen eines festen Körpers und werden normalerweise als Beschädigung von Strukturen angesehen. Der Bereich der Mechanik, der sich mit diesen Phänomenen befasst, ist ein wichtiger Aspekt bei der Konstruktion von Bauteilen, da er einen großen Einfluss auf die Sicherheit hat. Die physikalisch umfassende Beschreibung der Bruchmechanik ist für den Ingenieurbereich unpraktisch, daher wurden unterschiedliche Strategien von der Mikroskala über das Aufbrechen von Atombindungen bis hin zu einem reduzierten Modell in Form einer Kontinuumsanalyse verfolgt. A.A. Griffith, einer der Begründer der Bruchmechanik, erwog ein auf einem Energiekriterium basierendes Modell, das in verschiedenen Behandlungen zur Beschreibung der Rissausbreitung verwendet wurde. Sein Modell definierte eine Oberflächenenergie, die die Rissoberfläche als einen energetisch günstigeren Zustand im Vergleich zu einem Material unter einer bestimmten mechanischen Belastung beschrieb. Risse im numerischen Modell bereiten aufgrund diskontinuierlicher Eigenschaften Schwierigkeiten bei ihrer Approximation. Ein Ansatz, dies zu vermeiden, wurde von Bourdin mit einer regularisierten Version entwickelt. In seinem entwickelten Bruchmodell wird der Riss Teil des Festkörpers und wird durch eine neue Phase oder einen neuen Zustand mit stark reduzierter Steifigkeit angenähert. Dieses Phasenfeldmodell, das allgemein bei Erstarrungs- oder Transformationsprozessen zur mathematischen Beschreibung des Übergangs einer Materialphase in eine andere verwendet wird, hat einen neuen Anwendungsfall erhalten. Dabei werden die beiden Phasen durch die Parameterübertragung einer Ordnung vom gesunden Material zum geschädigten Material bzw. zum Riss gesteuert. Die vorgestellte Arbeit konzentriert sich auf die Verbesserung des Bruchphasenfeldes durch Verbesserung der Näherungsmethode unter Zuhilfenahme Verwendung spezieller Formfunktionen, die von Kuhn und Müller in Bruchphasenfeldmodelle eingeführt wurden. Auch wenn die eingeführten speziellen Formfunktionen hervorragende Ergebnisse bei der Approximation von Bruchflächen in Phasenfeldmodellen zeigten, fehlt es ihnen ohne weitere Anpassung an Allgemeingültigkeit und Genauigkeit. Das Problem der Genauigkeit ergibt sich aus der Ordnung der Formfunktionen, die im folgenden Fall unendlich ist, da die angewendeten Sonderfunktionen exponentiell sind. Im Rahmen der Finite-Elemente-Methode wird das Gebiet lokal numerisch integriert und würde für ein optimales Ergebnis unendlich viele Integrationspunkte erfordern was aus Gründen der Umsetzbarkeit begrenzt werden muss, jedoch sollte die verwendete Anzahl ein Kompromiss aus Effizienz und Genauigkeit darstellen. Die größte Herausforderung bei der Nutzung der exponentiellen Formfunktionen zur Approximation des Bruchfeldes ist das Problem der Unsymmetrie. Phasenfeldmodelle bilden Rissflanken symmetrisch ab, die eingeführten exponentiellen Formfunktionen besitzen diese Eigenschaft jedoch nicht. Daher müssen die Formfunktionen an gegenüberliegenden Rissflächen neu ausgerichtet werden. Vor der Simulation bestimmter Lastfälle ist der Rissverlauf unbekannt. Um beliebig wachsende Risse berechnen zu können, ist daher ein adaptiver Algorithmus erforderlich, der ein entsprechend definiertes Rissphasenfeld liefert. Abschließend wird der entwickelte Algorithmus für verschiedene Lastfälle analysiert und auf seine Effizienz hin diskutiert.

## Abstract

Fractures are a manifestation in emerging surfaces of a solid body and are normally viewed as damage in mechanical structures. The field of mechanics devoted to these phenomena is an important aspect of the design of structures. The physically comprehensive description of fracture mechanics is impractical for the field of engineering, therefore different strategies have been pursued from the microscale and breaking atom bonds to a reduced model in the form of a continuum analysis. A. A. Griffith, a founding father of fracture mechanics, considered a model based on an energy criterion, which is used in a variety of treatments to describe crack propagation. His model defined surface energy, which described the crack surface as an energetically favourable state compared to the material under a certain level of mechanical stress. Cracks in numerical models cause difficulties in their approximation, because of discontinuous properties. An approach to avoid this was made by Bourdin with a regularized version. In the fracture model that he developed, the crack becomes part of the solid body and is approximated by a new phase or state with a drastically reduced stiffness. Phase field models were used initially for solidification or transformation processes to mathematically describe the transition of one material phase into another, and gained a new application case for the description of fracturing. Thereby, the two phases, controlled by one order parameter shift from sound material to damaged material or respectively crack. The presented work focuses on the flexible utilisation of an improved approximation, which uses special shape functions for the fracture phase field model. The application of these shape functions for a phase field fracture model has first been introduced by Müller and Kuhn. Even though the introduced special shape functions show great results in approximating fracture surfaces in phase field models, they lack generality and accuracy without further adaptation. The issue of accuracy is a result of the order of the shape functions, which is in the following case infinite because the applied special functions are exponential. In the framework of the Finite Element Method, the domain is locally numerically integrated and would require infinitely fine integration which for an optimal result should be controlled to offer an accurate but efficient solution. The greatest challenge of the utilization of the exponential shape functions for the approximation of fracture field is the problem of asymmetry. The correct approximation of cracks by phase field models is symmetrical, but the introduced exponential shape functions do not have this characteristic. Therefore, the crack path and the required orientation of the shape functions are unknown. To compute arbitrary growing cracks, an adaptive algorithm has been developed and implemented to provide an appropriately defined crack phase field orientation. The presented algorithm is described and tested for different load case scenarios, followed by an analysis and discussion of the results.



# Contents

<b>1</b>	<b>Introduction</b>	<b>3</b>
1.1	Motivation . . . . .	3
1.2	Objectives and Outline . . . . .	5
<b>2</b>	<b>Continuum Mechanics</b>	<b>7</b>
2.1	Kinematics . . . . .	7
2.2	Strain measures for small deformations . . . . .	8
2.3	Stress . . . . .	9
2.4	Balance Laws . . . . .	11
2.4.1	Conservation of Mass . . . . .	11
2.4.2	Conservation of Linear and Angular Momentum . . . . .	11
2.4.3	Conservation of Energy and Caloric Equation of State . . . . .	12
2.4.4	Entropy . . . . .	13
2.4.5	Linear Elasticity . . . . .	14
<b>3</b>	<b>Linear Elastic Fracture Mechanics</b>	<b>15</b>
3.1	Basic premise . . . . .	15
3.2	K-concept . . . . .	16
3.3	Energy Concept by Griffith . . . . .	17
3.4	The Variational Formulation . . . . .	18
<b>4</b>	<b>A Phase Field Model for Static Fractures</b>	<b>19</b>
4.1	Variational Formulation of the Fracture Phase Field Models . . . . .	19
4.2	Evolution Law . . . . .	21
4.2.1	Thermodynamical Background . . . . .	21
4.2.2	Irreversibility . . . . .	23
4.3	Consideration of the Tension and Compression Asymmetry of Cracks . . . . .	23
	Volumetric-Deviatoric Decomposition of the Strain Energy Density . . . . .	24
	Spectral Decomposition of the Strain Energy Density . . . . .	24
<b>5</b>	<b>Finite Element Implementation</b>	<b>27</b>
5.1	Weak Forms and Spatial Discretization . . . . .	27
5.2	Time Discretization and Iterative Solution . . . . .	30
5.3	2d/3d Isoparametric Representation . . . . .	32
5.4	Exponential Finite Elements . . . . .	33
5.4.1	Introduction . . . . .	33
5.4.2	2d Exponential Shape Functions . . . . .	36
5.4.3	Extension to 3d . . . . .	38
5.4.4	Numerical Test . . . . .	40
<b>6</b>	<b>Adaptive Numerical Integration</b>	<b>43</b>
6.1	Numerical Integration . . . . .	43
6.1.1	Numerical Integration with Gauß-Legendre Formulas . . . . .	44

6.1.2	Adaptive Quadrature . . . . .	45
	Localization for Adaptivity . . . . .	45
	Order Adaptivity of the Numerical Integration . . . . .	46
	Double Exponential Formula . . . . .	50
6.1.3	Numerical Results . . . . .	51
6.2	Summary and Outlook . . . . .	53
<b>7</b>	<b>Adaptive Shape Functions</b>	<b>55</b>
7.1	Basics of Adaptive FE . . . . .	55
7.2	Concept . . . . .	57
7.3	Continuity . . . . .	58
7.4	Blending Elements . . . . .	59
7.5	Application Limits . . . . .	62
7.6	Exponential Crack Tip Influence . . . . .	63
7.7	Marking Strategy . . . . .	64
7.8	Process Sequence . . . . .	67
7.9	Evaluation . . . . .	69
	7.9.1 Local Exponential Solution . . . . .	69
	7.9.2 Halved Tension Test . . . . .	73
	7.9.3 Simple Shear Test . . . . .	76
	7.9.4 Halved Peel-off Test . . . . .	79
<b>8</b>	<b>Conclusion and Outlook</b>	<b>83</b>
	<b>Bibliography</b>	<b>87</b>

## Nomenclature

### Notation – representation of scalars, tensors

$g, G, \gamma, \Gamma$	Scalar quantity
$\underline{g}, \underline{G}, \underline{\gamma}, \underline{\Gamma}$	Vectorial quantity, second- and higher order tensors

### Mathematics – operators and functions

$\partial(\bullet)/\partial t$	Partial time derivative
$d(\bullet)/dt$	Total time derivative
$\text{tr}(\bullet)$	Trace of $\bullet$
$\nabla$	Gradient operator vector
$\otimes$	Dyadic product
$\exp$	Exponential function
$\text{sign}$	Sign function
$\tanh$	Hyperbolic tangent function

### Physics

$\mathcal{B}$	Domain of body
$\underline{\underline{B}}^s$	Differential operator matrix $s$
$\underline{\underline{B}}^u$	Differential operator matrix $u$
$\mathcal{C}$	Crack set
$\mathbb{C}$	Elasticity tensor
$\underline{\underline{D}}$	Damping matrix
$\underline{d}$	vector of degrees of freedom
$E$	Young's modulus
$\underline{\underline{E}}$	Green-Lagrange strain tensor
$E^e$	Elastic energy
$e$	Strain deviator
$\underline{\underline{F}}$	Deformation gradient
$\underline{f}$	Body force vector
$h$	Element size
$\mathcal{G}$	Energy release rate
$\mathcal{G}_c$	Crit. energy release rate or crack resistance
$\underline{\underline{J}}$	Jacobian matrix
$\underline{\underline{K}}$	Stiffness matrix
$K_{I,II,III}$	Stress intensity factors
$r_m$	Production of mass
$L$	Simulation domain size
$\underline{L}$	Velocity gradient
$l_c$	Crack field width
$N_I$	Shape functions of node $I$
$n_{\text{GP}}$	Number of Gauß points
$M$	Mobility factor
$\underline{P}$	Global internal force vector
$\underline{q}^m$	Mass flux
$\underline{q}^\theta$	Heat flux
$\underline{t}$	Cauchy stress vector

$s$	Fracture phase field
$\underline{\mathbf{R}}^s$	Residual of $s$
$\underline{\mathbf{R}}^u$	Residual of $\mathbf{u}$
$\underline{\mathbf{S}}$	Tangent matrix
$\mathcal{S}$	Entropy
$t$	Time
$\mathbf{u}$	Displacement vector
$w_p, w_k$	Weight of integration point
$\mathbf{x}, \mathbf{X}$	Actual and spatial position
$\gamma$	External micro force
$\Gamma$	Surface energy
$\delta$	Parameter of exponential shape functions
$\delta_{ij}$	Kronecker $\delta$
$\varepsilon$	Infinitesimal strain tensor
$\eta$	Residual Stiffness parameter
$\vartheta$	Temperature
$\lambda, \mu$	Lamé constants
$\nu$	Poisson's ratio
$\xi$	Natural coordinates
$\pi$	Internal micro force
$\rho$	Mass density
$\boldsymbol{\sigma}$	Cauchy stress tensor
$\psi$	Helmholtz free energy density
$\psi^e$	Elastic energy
$\psi^s$	Surface energy density
$\Omega$	Open region of $\mathcal{B}$
$\mathbf{1}$	Identity matrix

## Chapter 1

# Introduction

### 1.1 Motivation

Fracture is described as the entire or partial separation of a previously undamaged solid body due to the application of excessive loads. The main design driver of engineering structures is the assurance to prevent failure, which ultimately results in the fracture analysis of mechanical systems. Therefore, the development process of products with certain mechanical properties requires verification via different approaches like analytical, experimental and numerical methods. All methods have their merits and inferiorities, e.g. an analytical approach gives an elegant and continuous solution but reaches the limits of its applicability even for simple systems very quickly, an experimental approach contains all occurring physical effects but is comparably expensive and time-consuming and a numerical approach is adaptable but lacks accuracy. The numerical analysis became the dominant one despite its weaknesses because of its efficiency, speed and expandability. It achieved a triumphal march also in the durability evaluation, but reliable fracture models are still an ongoing topic in research.

The original mechanical theories were not sufficient enough to describe fracturing, which was the main driver for the motivation to find a solution for the description of fracture mechanics. The origin of modern fracture mechanics goes back to A. A. Griffith and the time of World War I. He established the fundamental principles of fracture mechanics in [30]. Griffith described cracking not from the micro to the macro scale and neglected the breaking of atomic bonds, but used a top-down approach and defined the macro scale of the crack with an additional energy term. The connection of Griffith's newly defined crack or crack surface energy with continuum mechanics was an accomplishment by Irwin in [38]. This offered the possibility of new approaches to fracture mechanics.

Although Griffith's and Irwin's fundamental laws laid the foundation stone for fracture mechanics, they lack certain aspects, e.g. branching, nucleation and deflection of cracks. In 1998 G. A. Francfort and J.-J. Marigo introduced in [26] a variational model for a brittle fracture by implementing Griffith's approach. The total energy of the system is the sum of the elastic energy, depending on the displacement, and the surface energy, describing the crack.

Physical models require a numerical adaptation, for an efficient solution to practical problems, which is also a concern in fracture mechanical models. In mesh-based methods, there are two types of approaches to describe fracturing: discrete and diffusive. The particle finite element method (PFEM) [63] and the extended finite element method (XFEM) [53], [10], [27] and [70] fall under the category of discrete models. Diffusive models require an additional field variable or order parameter to define fractures. This additional variable achieves a smooth and continuous transition of the stiffness within the domain from damaged to undamaged areas. In 2000 B. Bourdin introduced a numerical approach for fracture mechanics in [15] of the regularized form based on the variational setting by Francfort and Marigo [26],

which became a starting point for many publications and extensions, see [40], [50] and [13]. The diffusive fracture models became linked to phase field models, because of their similar formulation, which defines the transformation of material or physical properties. Phase field models appeared first in the context of phase transition processes, where they allow for describing various processes in heterogeneous continua, that range from solidification [11] and phase transformation in a solid [65] to the modeling of ferroelectric materials [66]. The biggest advantage of the phase field models for fracture is the smooth interpolation between the crack and the intact material, which can be handled better using finite elements. Furthermore, they can be easily expanded in physical and material behaviour, i.e. to dynamic [64], fatigue [67] [48] plastic [57] [23] [51] [2], viscoelastic [20], higher order deformation [75], shells [39] and composites [62].

The state-of-the-art method in the numerical analysis of structures and solids is the Finite Element Method (FEM) which proves itself in different descriptions of physical models as an efficient and robust method. The extension of the FEM to different fields of application is of interest in engineering, for example, fluid-, contact-, friction- and biomechanics. The discretization procedure is basically the partitioning of the domain or geometry into a number of elements. Then the analytical solution of the field variables is numerically approximated by shape functions within each element. Although the implementation of phase field models in general and particularly fracture field methods poses little effort, there are still challenges to tackle, as described by De Lorenzis in [21]. Therein, the problems are divided into non-convexity, irreversibility and FE mesh quality. The first issue results in convergence problems when the weak form is solved of the displacement and phase field monolithically. A remedy is the promising staggered scheme, which is more robust but is computationally expensive, see e.g. [3]. The second issue is based on the formulation of fracture phase field models as variational inequality, which requires a solution of a constrained minimization problem. There are different options for constraint enforcement, see e.g. [28]. This work's focus on the importance of the spatial discretization of fracture phase field models lies in the approximation of the transition zone. All phase field models eventually have to describe transition zones to separate different material or physical states, which in the case of the fracture field are the fracture surfaces of the crack. The transition zone or fracture surface is defined by a length scale parameter, which has to be sufficiently small to approximate the shape crack within the geometry appropriately. In order to describe the transition zone or in the case of the fracture phase field, the fracture field, numerically accurately, the spatial discretization in the form of Finite Elements must be adequately small or in other words, the mesh has to be dense in these areas of high phase field gradients. Ultimately, the classical approach of increasing the mesh density increases accuracy but decreases efficiency. A different approach is to increase the order of the shape functions, which are used to approximate the fields. The approach is called  $p$ -refinement and tailored high-order polynomials are used to approximate the solution. It is accompanied by an increase in the number of nodes, which increases the band width of the tangent matrix.

Another kind of higher-order method is the Isogeometric Analysis (IGA), which implements (high-order) B-splines or non-uniform rational B-splines (NURBS) to approximate the solution. The NURBS discretization can be based on the models available from Computer Aided Design (CAD) software. The advantage is higher inter-element continuity and increased accuracy per degree of freedom, which is also demonstrated for phase field models [12]. This is also implemented for the fracture phase field method in the context of an adaptive refinement scheme in [17].

A combined refinement strategy is the  $hp$ -refinement method, which in addition to an element size reduction ( $h$ ) in certain areas, uses transition elements between elements with different order, see e.g. [6]. These transition elements have different numbers of nodes ( $p$ ) on different element edges.

In the case of a changing solution, refinement is required to be adaptive. The basic form of adaptive finite element methods is initiated by error estimators, which support the marking of optimal local element sizes. Thereby, marking strategies identify elements with the potential for improved approximation. The process can be done as a step-by-step adjustment of the refinement.

All methods that are mentioned are capable of improving the approximation in general, which is also valid for transition zones in the fracture phase field. Unlike arbitrary solutions, the shape of these transition zones is a priori known and described by an exponential shape, with the steepness defined by the regularization parameter. In 2011, Kuhn and Müller [42] constructed shape functions that approximates the crack surface ideally. Thereby, they could reduce the demand for a finer discretization by increasing neither the number of elements nor the nodes. Unfortunately, the application of these special shape functions also comes with additional effort, i.e. a higher order numerical integration and reorientation for symmetry purposes. The objective presented in the work is to investigate the application of these shape functions to resolve these deficits.

## 1.2 Objectives and Outline

This work can be viewed as an extension of Kuhn's and Müller's work on the phase field model for brittle quasi-static fracture, but more specifically the exponential shape functions implemented in [42], [43] and [40]. The application of these exponential shape functions requires additional effort because of the open issues of which two are addressed in this work. These are the orientation problem and integration issues. This work describes the formulation of adaptive algorithms to fix the orientation issue and improve the numerical integration scheme.

In the first step, the necessary fundamentals of continuum mechanics are introduced in chapter 2. Thereby, the most basic mechanical material behaviour, linear elasticity for small deformations is described. This limitation is applied in the remainder of the work. The following chapter 3 recapitulates the field of linear fracture mechanics and closes the gap between the original aspects and the newly developed numerical models. The variational formulation of brittle fracture initiates the presentation of the fracture phase field model. Chapter 4 describes the fracture phase field model in the form of [40], with the extension of the tension-compression models described more thoroughly in [64]. The main novel content of this work starts in chapter 6. Here, the numerical integration for exponential shape functions is analysed. Thereby, two strategies are pursued, a higher order Gauß-Legendre and a double exponential formula for the numerical integration. Both methods require, for a better approximation of the exponential shape functions, a higher number of integration points, and therefore the emphasis lies on numerical efficiency. The influence of the phase field on the choice of integration points is thereby considered in a straightforward approach. The core objective of this work is the reorientation algorithm for exponential shape functions. The high priority of this aim lies in its necessity for the application of these special shape functions for the computation of arbitrary crack paths. While the conditions of the correct orientation are well-defined for a static crack, in a crack propagation case, this becomes more difficult. For a reduced effort of the approach, the algorithm's goals are extended to a strategy that implements linear shape functions in regions with a constant phase field. The algorithm is tested and evaluated in different scenarios.

Chapter 8 summarizes the work and is followed by a view of possible improvements and suggestions for future work.



## Chapter 2

# Continuum Mechanics

In this work, the static fracture mechanical behaviour is studied in the framework of continuum mechanics. The purpose of this chapter is to present the required basic principles for the following work, but it does not claim to provide a complete discussion of continuum mechanics. More comprehensive introductions to various aspects can be found in the literature, for instance in the textbooks Holzapfel [36], Altenbach [1], Gross and Becker [9] and Gurtin [33].

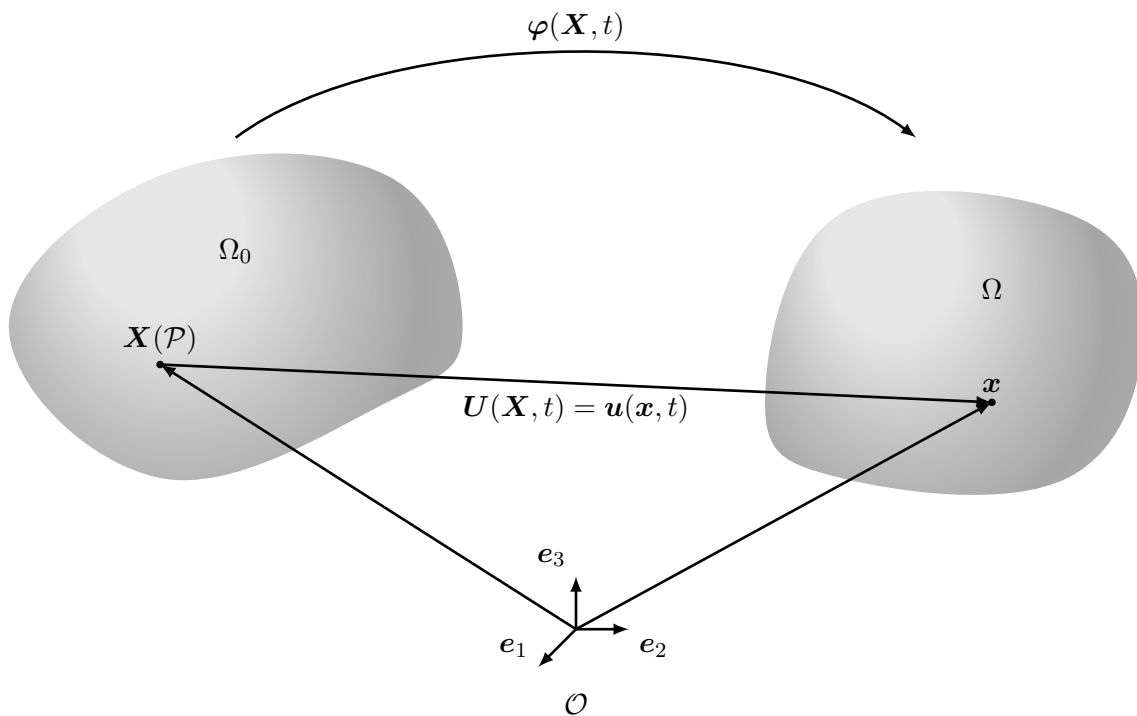


FIGURE 2.1: Reference and actual configuration.

### 2.1 Kinematics

Material points are described by their spatial position  $\mathbf{X}$ , which are the position vectors in a reference configuration  $\Omega_0$  for the body  $\mathcal{B}$ , see Fig. 2.1. The transition of the material points to their actual position  $\mathbf{x}$  in the current configuration  $\Omega$  is given by the deformation mapping

$$\mathbf{x} = \varphi(\mathbf{X}, t), \quad (2.1)$$

where the variable  $t$  describes time. The mapping is generally non-linear and is assumed to be uniquely invertible.

For better readability capital and lowercase letters indicate values defined in the reference and current configuration, respectively. For example, the displacement of an arbitrary point  $\mathcal{P}$  can be defined in both configurations as  $U(\mathbf{X}, t)$  or  $u(\mathbf{x}, t)$ , i.e.

$$U(\mathbf{X}, t) = \varphi(\mathbf{X}) - \mathbf{X} = \mathbf{x} - \varphi^{-1}(\mathbf{x}, t) = \mathbf{u}(\mathbf{x}, t). \quad (2.2)$$

The material gradient of the mapping  $\varphi$

$$\mathbf{F} = \frac{\partial \varphi(\mathbf{X}, t)}{\partial \mathbf{X}} = \frac{\partial \mathbf{x}}{\partial \mathbf{X}} \quad (2.3)$$

is termed a deformation gradient. Besides the definition, the deformation gradient possesses the property to be described by symmetric positive definite stretch tensors  $\mathbf{A}$  or  $\mathbf{B}$  multiplied by a rotation tensor  $\mathbf{R}$ , i.e.

$$\mathbf{F} = \mathbf{R}\mathbf{A} = \mathbf{B}\mathbf{R}. \quad (2.4)$$

## 2.2 Strain measures for small deformations

In order to describe the deformation of continua, a suitable measure becomes necessary. Unfortunately, the deformation gradient is not sufficient because it includes rigid body motions. A common quantity is the Green-Lagrange strain tensor  $\mathbf{E}$ , which is defined in the reference configuration by

$$\mathbf{E} = \frac{1}{2} (\mathbf{F}^T \mathbf{F} - \mathbf{1}). \quad (2.5)$$

In many technical applications, the deformation can be assumed to be small, which holds also true for the models analysed in this work. This assumption enables the equivalent treatment of the current and the reference configuration. Thus,

$$J = \det(\mathbf{F}) \approx 1 \quad (2.6)$$

makes the differentiation of volume and the density in the actual and reference configuration redundant, i.e.

$$dv \approx dV, \quad \rho \approx \rho_0. \quad (2.7)$$

Considering small deformations entails a linearization that reduces the strain tensor to be of the form

$$\boldsymbol{\varepsilon} = \frac{1}{2} \left( \frac{\partial \mathbf{u}}{\partial \mathbf{x}} + \left( \frac{\partial \mathbf{u}}{\partial \mathbf{x}} \right)^T \right), \quad (2.8)$$

which is the linearised strain tensor. Further, in this case, deformation is small, the volume change of an infinitesimal volume element  $dV$  is equal to the trace of the linearized strain tensor

$$\varepsilon_V = \text{tr}(\varepsilon) = \varepsilon_{kk} = \frac{\Delta dV}{V}, \quad (2.9)$$

which is also known as the volume dilatation. The linearized strain tensor in an  $n$ -dimensional space can be split additively into a volumetric part and a deviatoric part by

$$\varepsilon = \frac{\text{tr}(\varepsilon)}{n} \mathbf{1} + \mathbf{e} \quad (2.10)$$

## 2.3 Stress

The dual quantities of the strains are the stresses. Although stresses or forces are not visible, they build the basis of applied mechanics. We consider a body  $\mathcal{B}$  which is loaded by an external force  $\mathbf{t}^*$  on the boundary  $\partial\Omega_t$  and external displacements  $\mathbf{u}^*$  on the boundary  $\partial\Omega_u$ , see Fig. 2.2. To gain information about the stress state in the continuum, a sectional view is used. On the section the stress vector  $\mathbf{t}$  of any arbitrary infinitesimal areas  $dA$  can be gained by

$$\mathbf{t}^* = \frac{d\mathbf{f}}{dA}, \quad (2.11)$$

where  $\mathbf{f}$  is the force on the sectional surface.

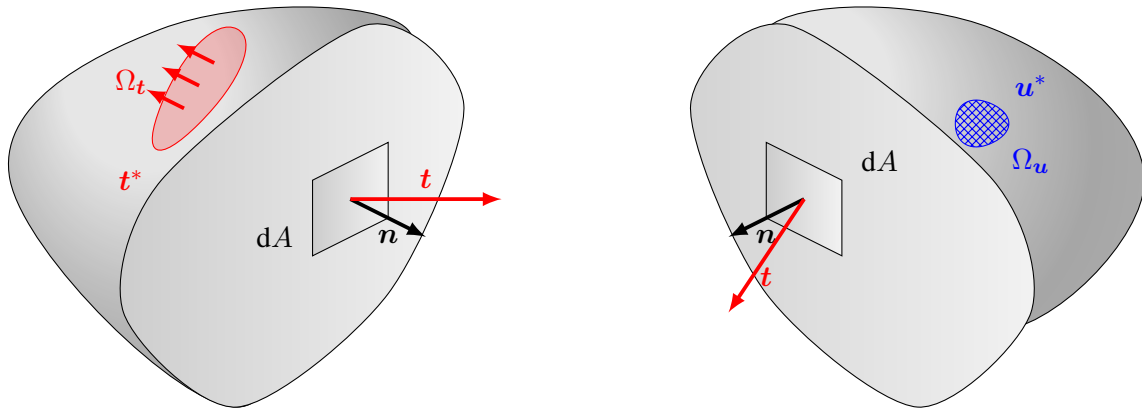


FIGURE 2.2: External condition and traction vector for arbitrary point.

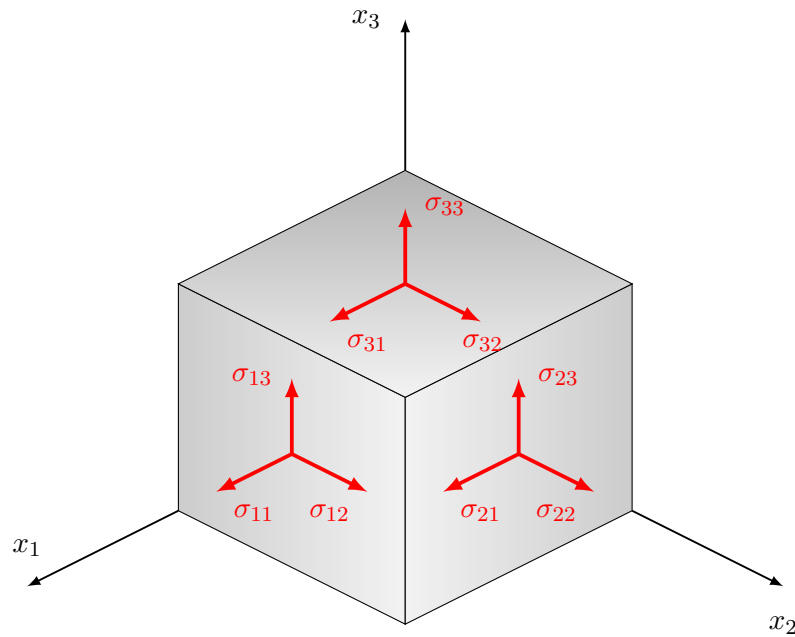


FIGURE 2.3: Stress state of a volume element.

The stress state at any point  $\boldsymbol{x}$  for a 3d Cartesian coordinate system can be described by considering 3 surfaces. It is convenient to consider that the normal vectors  $\boldsymbol{n}$  of these surfaces are orthogonal to each other. In Fig. 2.3, the most obvious choice for the normal vectors in the form of coordinate axes is depicted. The stress tensor can be represented by the following matrix structure

$$\boldsymbol{\sigma} = \begin{bmatrix} \sigma_{11} & \sigma_{12} & \sigma_{13} \\ \sigma_{21} & \sigma_{22} & \sigma_{23} \\ \sigma_{31} & \sigma_{32} & \sigma_{33} \end{bmatrix}. \quad (2.12)$$

The Cauchy-theorem states that the Cauchy stress tensor  $\boldsymbol{\sigma}$  projects the normal vector  $\boldsymbol{n}$  to the traction vector  $\boldsymbol{t}$ , i.e.

$$\boldsymbol{t} = \boldsymbol{\sigma}^T \boldsymbol{n}. \quad (2.13)$$

## 2.4 Balance Laws

In continuum mechanics, balance laws for different physical quantities such as mass, moment, angular momentum are formulated. The axiomatic law for a physical quantity  $\varphi$  integrated over a observed control volume  $\mathcal{P}_t$ , is balanced by the flux of the quantity. The volume also encounters a production  $r_\varphi$  and supply  $s_\varphi$ , i.e.

$$\frac{d}{dt} \int_{\mathcal{P}_t} \varphi \, dV = \int_{\partial\mathcal{P}_t} \mathbf{q}_\varphi \cdot \mathbf{n} \, dA + \int_{\mathcal{P}_t} (r_\varphi + s_\varphi) \, dV \quad (2.14)$$

The quantity field is assumed to be continuous and smooth. Therefore, using the Reynold's transport theorem

$$\frac{d}{dt} \int_{\mathcal{P}_t} \varphi \, dV = \int_{\mathcal{P}_t} \frac{\partial\varphi}{\partial t} \, dV + \int_{\partial\mathcal{P}_t} \varphi \mathbf{v} \cdot \mathbf{n} \, dA \quad (2.15)$$

and the Gauß's divergence theorem

$$\int_{\partial\mathcal{P}_t} \varphi \mathbf{v} \cdot \mathbf{n} \, dA = \int_{\mathcal{P}_t} \operatorname{div}(\varphi \mathbf{v}) \, dV \quad (2.16)$$

which local form of the equation results in,

$$\dot{\varphi} + \varphi \operatorname{div}(\mathbf{v}) = \operatorname{div}(\mathbf{q}_\varphi) + r_\varphi + s_\varphi. \quad (2.17)$$

### 2.4.1 Conservation of Mass

In a closed system, mass is constant and there is no mass production  $r_m = 0$ , supply  $s_m = 0$  or flux  $\mathbf{q}_m = 0$ . The mass balance over a material domain  $\mathcal{P}$  with the mass density  $\rho$  and velocity  $\mathbf{v}$  in its global form is

$$\frac{d}{dt} \int_{\partial\mathcal{P}} \rho \, dV = 0. \quad (2.18)$$

The local form of it is

$$\dot{\rho} + \rho \operatorname{div}(\mathbf{v}) = 0. \quad (2.19)$$

### 2.4.2 Conservation of Linear and Angular Momentum

The spatial global form of the conservation of linear momentum is given by

$$\int_{\partial\mathcal{P}} \mathbf{t}(\mathbf{n}) \, dA + \int_{\mathcal{P}} \mathbf{f} \, dV = \int_{\mathcal{P}} \rho \dot{\mathbf{v}} \, dV. \quad (2.20)$$

The global form of angular momentum has the form

$$\int_{\partial\mathcal{P}} \mathbf{x} \times \mathbf{t}(\mathbf{n}) \, dA + \int_{\mathcal{P}} \mathbf{x} \times \mathbf{f} \, dV = \int_{\mathcal{P}} \mathbf{x} \times \rho \dot{\mathbf{v}} \, dV. \quad (2.21)$$

The local form of the linear momentum can be obtained by employing the mass balance (2.18), the Cauchy-theorem (2.13) and Gauß-theorem, which results in

$$\rho \dot{\mathbf{v}} = \operatorname{div}(\boldsymbol{\sigma}^T) + \mathbf{f}. \quad (2.22)$$

Following a similar procedure for the angular momentum with the Eq. (2.22), Eq. (2.18) and Eq. (2.13) yields

$$\boldsymbol{\sigma} = \boldsymbol{\sigma}^T, \quad (2.23)$$

which shows that the Cauchy stress tensor is symmetric.

### 2.4.3 Conservation of Energy and Caloric Equation of State

The first law of thermodynamics is a formulation of the law of conservation of energy. The rate of total energy consists of internal energy  $E(\mathcal{P}_t)$  and kinetic energy  $K(\mathcal{P}_t)$  defined for a volume  $\mathcal{P}_t$  in the actual configuration, as it reads

$$\frac{d}{dt}(E(\mathcal{P}_t) + K(\mathcal{P}_t)) = \mathcal{W}(\mathcal{P}_t) + \mathcal{Q}(\mathcal{P}_t). \quad (2.24)$$

This is equal to the sum of the power of the external forces  $\mathcal{W}(\mathcal{P}_t)$  and the heat supply  $\mathcal{Q}(\mathcal{P}_t)$ .

The temporal derivative of the total energy

$$\frac{d}{dt}(E(\mathcal{P}_t) + K(\mathcal{P}_t)) = \frac{d}{dt} \int_{\mathcal{P}_t} \rho \left( \mathcal{U}^* + \frac{\|\mathbf{v} \cdot \mathbf{v}\|}{2} \right) \, dV = \int_{\mathcal{P}_t} \rho \left( \dot{\mathcal{U}}^* + \mathbf{v} \cdot \dot{\mathbf{v}} \right) \, dV \quad (2.25)$$

contains the specific internal energy  $\mathcal{U}^*$  and the squared norm of the velocity  $\mathbf{v}$  integrated over any arbitrary volume  $\mathcal{P}_t$ .

The power of external forces and the external thermal power are given by

$$\mathcal{W}(\mathcal{P}_t) = \int_{\mathcal{P}_t} \mathbf{f} \cdot \mathbf{v} \, dV + \int_{\partial\mathcal{P}_t} \mathbf{t} \cdot \mathbf{v} \, dA \quad (2.26)$$

and

$$\mathcal{Q}(\mathcal{P}_t) = \int_{\mathcal{P}_t} \rho s_{\theta}^* \, dV + \int_{\partial\mathcal{P}_t} \mathbf{q}^{\theta} \cdot \mathbf{n} \, dA, \quad (2.27)$$

respectively. In its local form, the energy balance yields

$$\rho \dot{\mathcal{U}}^* = \rho s_{\theta}^* + \boldsymbol{\sigma} : \mathbf{d} - \operatorname{div}(\mathbf{q}^{\theta}), \quad (2.28)$$

which requires the application of the Gauß' divergence theorem and the balance law for linear momentum, Eq. (2.20).

### 2.4.4 Entropy

In its global form, the balance of an entropy  $\mathcal{S}$  with the entropy density and the entropy production  $\mathcal{S}^*$  and  $r_{\mathcal{S}}$ , reads

$$\frac{d}{dt} \int_{\mathcal{P}_t} \rho \mathcal{S}^* dV = - \int_{\partial \mathcal{P}_t} \frac{\mathbf{q}^\theta}{\theta} \cdot \mathbf{n} dA + \int_{\mathcal{P}_t} \left( r_{\mathcal{S}} + \rho \frac{\dot{\mathcal{S}}^*}{\theta} \right) dV. \quad (2.29)$$

On the right-hand side, the heat flux over the surface  $\partial \mathcal{P}_t$  and the supply over the domain  $\mathcal{P}_t$  are normalized by the absolute thermodynamic temperature. They are assumed to be the entropy flux and supply. The second law of thermodynamics states that the production of the entropy  $r_{\mathcal{S}}$  can not be negative, i.e.

$$r_{\mathcal{S}} \geq 0. \quad (2.30)$$

This leads to the local formulation of Eq. (2.29),

$$\rho \dot{\mathcal{S}}^* + \operatorname{div} \left( \frac{\mathbf{q}^\theta}{\theta} \right) + \frac{1}{\theta} \left( -\operatorname{div}(\mathbf{q}^\theta) - \rho \dot{\mathcal{U}}^* + \boldsymbol{\sigma} : \mathbf{d} \right) \geq 0. \quad (2.31)$$

With the rearranged identity

$$\operatorname{div} \left( \frac{\mathbf{q}^\theta}{\theta} \right) - \frac{1}{\theta} \operatorname{div}(\mathbf{q}^\theta) = -\frac{1}{\theta^2} \mathbf{q}^\theta \nabla_{\mathbf{x}} \theta \quad (2.32)$$

and the Helmholtz free energy,

$$\psi^* = \mathcal{U}^* - \theta \mathcal{S}^*, \quad (2.33)$$

$$\dot{\psi}^* = \dot{\mathcal{U}}^* - \dot{\theta} \mathcal{S}^* - \theta \dot{\mathcal{S}}^*, \quad (2.34)$$

Eq. (2.31) yields the Clausius-Duhem inequality

$$\left( -\rho \dot{\psi}^* - \operatorname{div}_{\mathbf{x}}(\mathbf{q}^\theta) - \rho \dot{\mathcal{U}}^* + \boldsymbol{\sigma} : \mathbf{d} \right) = r_{\mathcal{S}} \geq 0. \quad (2.35)$$

By multiplying the above inequality (2.35) with the absolute temperature  $\theta$  and integrating it over the domain  $\mathcal{P}_t$ , gives

$$\int_{\mathcal{P}_t} \left( \boldsymbol{\sigma} : \mathbf{d} - \rho \left( \dot{\psi} + \mathcal{S}^* \dot{\theta} \right) + \frac{1}{\theta} \mathbf{q}^\theta \nabla_{\mathbf{x}} \theta \right) dV \geq 0, \quad (2.36)$$

which can be divided in

$$\mathcal{D}_{\text{con}} = - \int_{\mathcal{P}_t} \frac{1}{\theta} \mathbf{q}^\theta \nabla_{\mathbf{x}} \theta dV \geq 0 \quad \text{and} \quad (2.37)$$

$$\mathcal{D}_{\text{loc}} = - \int_{\mathcal{P}_t} \boldsymbol{\sigma} : \mathbf{d} - \rho \left( \dot{\psi} + \mathcal{S}^* \dot{\theta} \right) dV \geq 0, \quad (2.38)$$

the conductive and local part. Assuming that the Helmholtz free energy per unit volume  $\psi = \rho \psi^*$  is a function of the deformation gradient  $\mathbf{F}$  and the temperature  $\theta$

$$\psi = \rho \psi^*(\mathbf{F}, \theta), \quad (2.39)$$

and the local form of the Clausius-Planck inequality (Eq. 2.39) results in,

$$\left( \mathbf{P} - \frac{\partial \tilde{\psi}}{\partial \mathbf{F}} \right) : \dot{\mathbf{F}} + \left( -\mathcal{S} - \frac{\partial \tilde{\psi}}{\partial \theta} \right) \dot{\theta} \geq 0. \quad (2.40)$$

This implies the constitutive relations,

$$\mathbf{P} = \frac{\partial \tilde{\psi}}{\partial \mathbf{F}} \quad \text{and} \quad (2.41)$$

$$\mathcal{S} = \frac{\partial \tilde{\psi}}{\partial \theta}. \quad (2.42)$$

In case of small deformation, the linearized  $\varepsilon$  is considered instead of the deformation gradient  $\mathbf{F}$  and the Helmholtz free energy  $\psi = \rho\psi^*(\varepsilon, \theta)$  becomes dependent on  $\varepsilon$ . Further the symmetric part of the velocity gradient,  $\mathbf{d}$ , approximates into the rate of the strain tensor  $\dot{\varepsilon}$ . Thus,

$$\left( \mathbf{P} - \frac{\partial \tilde{\psi}}{\partial \varepsilon} \right) : \dot{\varepsilon} + \left( -\mathcal{S} - \frac{\partial \tilde{\psi}}{\partial \theta} \right) \dot{\theta} \geq 0. \quad (2.43)$$

## 2.4.5 Linear Elasticity

In this work, the materials that are considered are brittle and therefore linear elastic until the cracks emerge. A state constraint is the isothermal conditions ( $\dot{\theta} = 0$ ), which provides the free energy density

$$\psi = \frac{1}{2} \varepsilon : [\mathbf{C} \varepsilon]. \quad (2.44)$$

The free energy density contains

$$\boldsymbol{\sigma} = \mathbf{C} \varepsilon = \frac{\partial \psi}{\partial \varepsilon}, \quad (2.45)$$

Hooke's law of elasticity. The fourth order tensor  $\mathbf{C}$  is the elasticity tensor and its symmetry is a result of the symmetry of the stress, strain tensors and the constitutive relation (Eq. 2.45). The tensor can be reduced to 21 components

$$\mathbf{C}_{ijkl} = \mathbf{C}_{jikl} = \mathbf{C}_{ijlk} = \mathbf{C}_{klij}. \quad (2.46)$$

A material that shows the same behaviour in every direction is isotropic and in this case the stiffness tensor  $\mathbf{C}$  can be reduced to two constants  $\lambda$  and  $\mu$

$$\mathbf{C}_{ijkl} = \lambda \delta_{ij} \delta_{kl} + \mu (\delta_{ik} \delta_{jl} + \delta_{il} \delta_{jk}), \quad (2.47)$$

the Lamé constants. These can be used to calculate two more practical elasticity parameters, the Young's modulus  $E$  and the Poisson's ratio  $\nu$ ,

$$E = \frac{\mu(3\lambda + 2\mu)}{\lambda + \mu} \quad \text{and} \quad \nu = \frac{\lambda}{2(\lambda + \mu)}. \quad (2.48)$$

## Chapter 3

# Linear Elastic Fracture Mechanics

This chapter gives an introduction to the analysis of static fracture of brittle materials within the framework of continuum mechanics. For a detailed scope, textbooks on fracture mechanics such as Gross and Seelig (2011) [31], Kuna [45] can be recommended.

### 3.1 Basic premise

Fracturing is a complex process, which includes many facets, from the macro to the microscale. To describe the phenomena of cracking on all involved scales, complex processes e.g. bond breaking need to be modeled. On a macro scale, this approach would become infeasible. Therefore, the focus lies on developing an applicable approach within the framework of continuum mechanics. So, from this point, every solid body that is analysed can be seen as a continuum continuously filled with material. Thereby, the complexity is reduced by describing microscopic processes during crack growth with a comparable macroscopic crack material behaviour, which is an indirect representation.

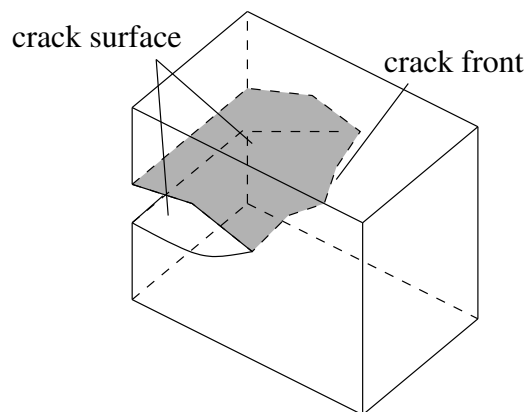


FIGURE 3.1: Crack model.

The geometry of a crack is defined as a small gap between two surfaces that were in a prior state of the body connected, see Fig. 3.1. In models with a reduced set of dimensions like 2d or 1d the crack only contains lines or even points. The gap between two surfaces is mathematically described as a discontinuity. In the process of cracking the final stage is a total separation of a body. In the intermediate stage of the crack growth, there is a crack front, which is a line and in a reduced form (2d), a point. In the model, the crack surfaces are the point of interest and are in the following cases always free of external loads.

The fundamental material property in mechanics is linear elasticity. This can be combined with e.g. plasticity and viscosity, but also with a fracturing behaviour. This results in linear

elastic fracture mechanics for which the entire region is assumed to be linear elastic. An exclusion must be made in the so-called process zone, which is the nucleus of new fracture surfaces or cracks. Cracks or more specifically crack tips in the linear elastic theory cause singularities in the stress and strain fields. Therefore classical failure criteria are useless. The process zone doesn't exhibit singularity, but an inelastic material behaviour, which limits the stress and strain fields to a finite value. In the far field of the crack front, the linear elastic description of the material is admissible and yields plausible results.

### 3.2 K-concept

The opening of a crack essentially depends on the form of the load and therefore a characterization of crack modes is given. The basic forms are depicted in Fig. 3.2 and are named crack modes or crack opening modes. The first mode, Mode I is the only symmetric form and causes an opening between the crack surfaces. The mode II represents a sliding of the crack surfaces in opposite directions, leading to in-plane shear stresses. While mode I and II can be represented in a plane, the loading of mode III is perpendicular to the plane.

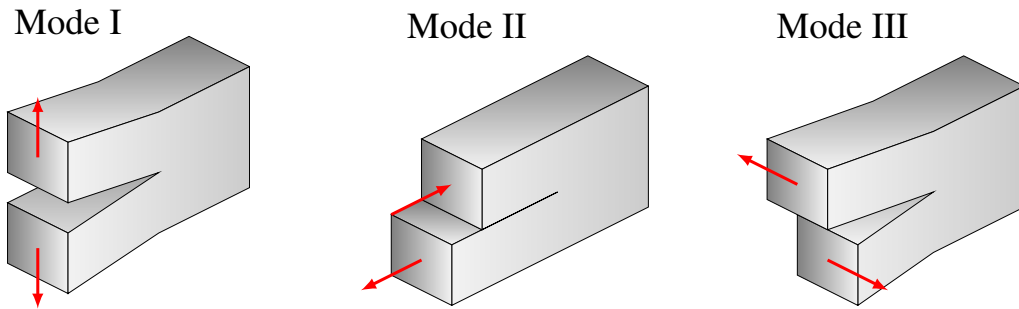


FIGURE 3.2: Crack modes I, II and III.

The stresses of the different modes outside of the process zone are best described in polar coordinates, see Fig. 3.3. The formula of the stress can be achieved by considering a 2d setting. In dependence on the radial coordinate  $r$ , the stress fields at the crack tip have the form

$$\sigma_{ij} \sim \frac{1}{\sqrt{r}} f_{ij}(\varphi). \quad (3.1)$$

The stress components differ for Mode I and II to Mode III, while the first two modes only result in a plane stress field ( $\sigma_{xx}$ ,  $\sigma_{yy}$  and  $\tau_{xy}$ ), the third mode results only in stresses in anti-plane shear stresses ( $\tau_{xz}$ ,  $\tau_{yz}$ ). But all contain trigonometric functions depending on the angle  $\varphi$ .

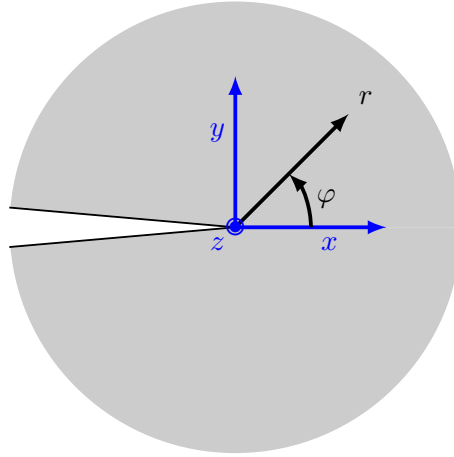


FIGURE 3.3: Coordinate systems,  $x, y, z$  and  $r, \varphi, z$  of the crack tip.

In [38], this is introduced as a fracture criterion, also known as  $K$ -concept, which defines the crack propagation by the stress intensity factors to a material specific value. The essential parameter of this  $K$ -concept is the stress intensity factors. They describe the asymptotic stress behaviour at the crack tip. In a pure mode I, the  $K$ -criterion can be describe by

$$K_I = K_{Ic}. \quad (3.2)$$

Thereby, the value  $K_{Ic}$  is a material parameter, the fracture toughness. In superimposed cases of more than one mode, the formulation has a general form

$$f(K_I, K_{II}, K_{III}) = 0 \quad (3.3)$$

### 3.3 Energy Concept by Griffith

A different approach for the assessment of fracture processes is an energy approach, layed out by Griffith [30], which is also the foundation of the fracture phase field method, used in this work. Therefore, the energy balance (Eq. 2.24) is expanded by an additional term  $\Gamma$ ,

$$\dot{E} + \dot{K} + \dot{\Gamma} = \dot{\mathcal{W}} + \dot{\mathcal{Q}}, \quad (3.4)$$

where  $\Gamma$  is called surface energy based on the crack surface  $A$  and reads

$$\Gamma = \mathcal{G}_c A. \quad (3.5)$$

$\mathcal{G}_c$  is a material parameter representing the crack resistance. The Eq. (3.4) can be reduced by assuming a quasi-static isothermal fracture ( $\dot{\mathcal{Q}} = \dot{K} = 0$ ) and conservative external forces ( $\dot{E} - \dot{\mathcal{W}} = \dot{\Pi}$ ). Thus an infinitesimal crack area extension  $dA$ , results in

$$\left( \frac{d\Pi}{dt} + \frac{d\Gamma}{dt} \right) \frac{dA}{dt} = 0. \quad (3.6)$$

This can be redefined in the form

$$(\mathcal{G}_c - \mathcal{G}) \dot{A} = 0, \quad (3.7)$$

where  $\mathcal{G}$  is the energy release rate, the derivative of the total potential with respect to the infinitesimal crack extension  $dA$ . The first term of Eq. (3.7) expresses the Griffith's criterion

$$\mathcal{G} = \mathcal{G}_c, \quad (3.8)$$

which is the requirement for the crack propagation. A transition to the  $K$ -concept can be defined for straight growing cracks, where the energy release rate is defined by

$$\mathcal{G} = \frac{1 - \nu^2}{E} (K_I^2 + K_{II}^2) + \frac{K_{III}^2}{2G}. \quad (3.9)$$

The values  $E$  and  $G$  are the Young's and shear modulus.

### 3.4 The Variational Formulation

The energy concept of Griffith laid the foundation for modern fracture mechanics and it became a fundamental column of fracture mechanics. Despite its benefits, the theory cannot describe the bifurcation and nucleation of cracks and unstable crack growth ( $\mathcal{G} > \mathcal{G}_c$ ). Its insufficiencies require a further extension, which is proposed in different approaches e.g. a maximum hoop stress criterion [25] or a maximum energy release rate criterion [77]. A variational reformulation of the classical Griffith criterion proposed by Francfort and Marigo [26], avoids these kinds of extension by creating a universal framework, which possesses the property to approximate advanced crack propagation possibilities. The starting point is the principle of global minimality of the total energy, which is, in the case in the theory of Griffith, the sum of surface (fracture) energy, strain energy and the potential of the external forces. The body  $\Omega$  is regarded to be  $n$ -dimensional, elastic and under isothermal condition with a smooth boundary  $\partial\Omega$ . For the restriction of crack healing, the crack set  $\mathcal{C}$  can't decrease over time, i.e.

$$\mathcal{C}(t_a) \subset \mathcal{C}(t_b) \quad \text{for all } t_a < t_b \quad (3.10)$$

and thus becomes irreversible. The surface energy  $\Gamma$  of the crack set  $\mathcal{C} \subset \mathcal{B}$  adopted from Griffith theory becomes

$$\Gamma(\mathcal{C}) = \mathcal{G}_c \mathcal{H}^{n-1}(\mathcal{C}) \quad (3.11)$$

and is proportional to the occupied area  $\mathcal{H}^{n-1}$ , which is the  $n - 1$ -dimensional Hausdorff measure. It is a measure for usual surfaces with sufficiently smooth hypersurfaces. Areas without cracks are characterized by linear elastic behaviour with small strains, i.e.

$$E^e(\mathcal{C}, \mathbf{u}) = \int_{\Omega \setminus \mathcal{C}} \frac{1}{2} \boldsymbol{\varepsilon}(\mathbf{u}) : (\mathbf{C} \boldsymbol{\varepsilon}(\mathbf{u})) dV. \quad (3.12)$$

Furthermore, the boundary can be subjected to displacement boundary conditions  $\mathbf{u}^*$  e.g.

$$\mathbf{u}(\mathbf{x}, t) = \mathbf{u}^*(\mathbf{x}, t) \quad \text{on } \partial\Omega_u \mathcal{C}(t). \quad (3.13)$$

The variational formulation of brittle fracture defines the criterion

$$E(\mathcal{C}, \mathbf{u}) = E^e(\mathcal{C}, \mathbf{u}) + \Gamma(\mathcal{C}) \quad (3.14)$$

with the pair of global minimizer  $\mathcal{C}, \mathbf{u}$ , being the crack set and the displacement, respectively.

## Chapter 4

# A Phase Field Model for Static Fractures

The fracture phase field, which will be used in the following, should be recapitulated at this point. A. A. Griffith [30] gave the impetus for the following model with the energy principle for cracks in 1921, whereby an energy functional is to be minimized. The presented model is the phase field model proposed by Kuhn and Müller in 2010 [41].

### 4.1 Variational Formulation of the Fracture Phase Field Models

Fracture phenomena can be described by the variational formulation of brittle fracture [26]. For a unified framework, a numerical implementation is required to use it in various fracture cases. But, this is not achieved without challenges, because an infinite number of arbitrary crack set evolutions exist and rely on preceding information about the crack. This was solved by Bourdin [15] and Bourdin and Chambolle [14] by adopting the regularized formulation by Ambrosio and Tortorelli [4] of the image segmentation of the Mumford-Shah functional [55]. Thereby, to describe the crack without any geometrical or functional changes of the model, a variable is allocated. This ansatz is called phase field method. The field variable is the crack condition of the local domain and is assigned the parameter  $s$ , which is dependent on the position  $x$  and the time  $t$ . The crack field  $s$  manifests two physical conditions of the bulk by fracture for 0 or unfractured for 1. This fracture phase field  $s(x, t)$  approximates the discrete crack  $\mathcal{C}$ . This also eliminates the need to track the crack. The extended equation of the energy functional by the additional smooth  $s$ -field yields

$$E(\boldsymbol{\varepsilon}, s) = \int_{\Omega} (\psi^e(\boldsymbol{\varepsilon}, s) + \psi^s(s)) \, dV. \quad (4.1)$$

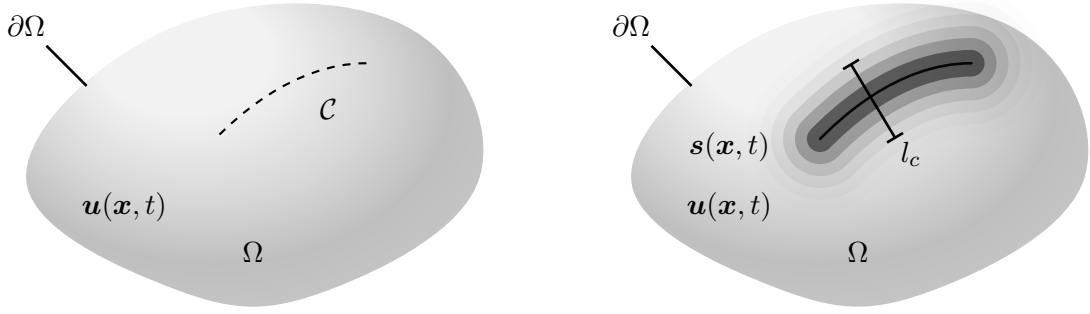


FIGURE 4.1: A solid body with a discontinuity (sharp crack)  $\mathcal{C}$  (left) and approximation of the same discontinuity by an order parameter field  $s(x, t)$  (right).

The regularized phase field model for brittle fracture includes two energy densities, the surface energy density  $\psi^s$  and the elastic energy density  $\psi^e$ . The smooth transition of the two conditions of the domain is described by a parameter  $l_c$ , see Fig. 4.1. The linear elastic model is complemented by another energy term, the surface energy. The formulation of its density is

$$\psi^s(s) = \mathcal{G}_c \gamma^s, \quad \gamma^s = \frac{1}{2c_w} \left( \frac{w(s)}{4l_c} + l_c |\nabla s|^2 \right). \quad (4.2)$$

The normalization constant  $c_w$  is a parameter ensuring the correct surface measure as  $l_c \rightarrow 0$ , c.f. (3.3). The order parameter potential  $w(s)$  can have different forms, see [15] [24]. For example, the double well potential

$$w(s) = 16s^2 + (1 - s^2)^2 \quad (4.3)$$

or the monotonous function

$$w(s) = (1 - s)^2. \quad (4.4)$$

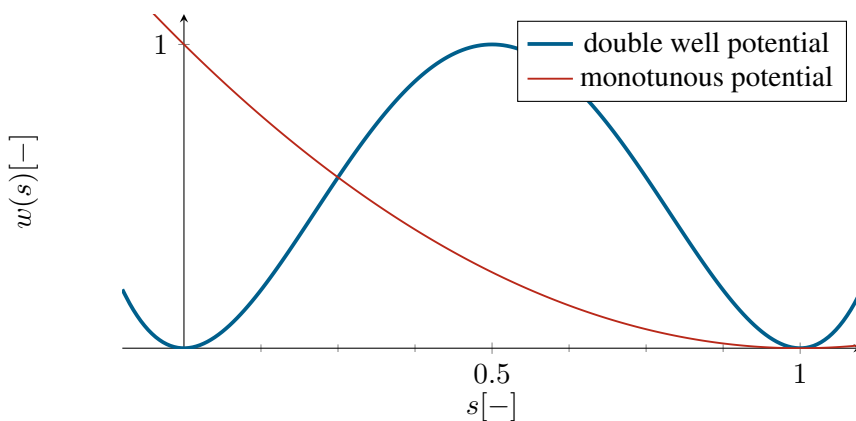


FIGURE 4.2: Potential functions for the fracture field model.

Their functional form is different in the approach to model the crack. While the double well potential incorporates a barrier between the conditions, the monotonous function does

not. The latter function is chosen here because the double well function causes an unphysical widening of cracks. For the use of the monotonous potential function, an additional modification discussed in section 4.2.2 is required to ensure the irreversible behaviour of the fracture state change and the normalization constant is required to be  $c_w = 0.5$ .

The second part of the surface energy density is dependent on the gradient of the fracture field. It ensures a minimality for the number of crack surfaces by penalizing it energetically. Both depend quadratically on the fracture field  $s$ , introduced as the order parameter of the material integrity. The surface energy also depends on its gradient ( $\nabla s$ ).

$$\psi^e(\boldsymbol{\varepsilon}, s) = (s^2 + \eta) \frac{1}{2} \boldsymbol{\varepsilon} : [\mathbf{C}\boldsymbol{\varepsilon}]. \quad (4.5)$$

The material behaviour is described by the linear elasticity tensor  $\mathbf{C}$ , the cracking resistance  $\mathcal{G}_c$  as well as the parameters  $\eta$  and  $l_c$ . The parameter  $\eta$  is a stabilizing parameter providing a residual stiffness of the cracked areas. The formula for the total energy density is

$$\psi(\boldsymbol{\varepsilon}, s) = \underbrace{\frac{1}{2}(s^2 + \eta)\boldsymbol{\varepsilon} : [\mathbf{C}\boldsymbol{\varepsilon}]}_{\psi^e(\boldsymbol{\varepsilon}, s)} + \underbrace{\mathcal{G}_c \left( \frac{(1-s)^2}{4l_c} + l_c |\nabla s|^2 \right)}_{\psi^s(s)}. \quad (4.6)$$

As primary fields in the domain  $\Omega$  we consider the displacements  $\mathbf{u}$ , which affect the energy density by the linearized strain tensor  $\boldsymbol{\varepsilon}$ , and the phase field variable  $s$ . The boundary conditions of the domain are tractions at  $\partial\Omega_t$  and displacements at  $\partial\Omega_u$ . The geometrically important parameter for a sufficient approximation of cracks is  $l_c$ , which controls the width of the continuous representation of cracks.

In essence, the energy density functional  $\psi$  is based on Griffith's theory of fractures, which states that the energy density that is consumed by an increase of the crack surface must be obtained from the released elastic energy during crack growth. In addition, the elastic energy density contains the parameter  $\eta$  for numerical stabilization to ensure a minimal stiffness in case of a total body rupture ( $s = 0$ ). The first field equation included in the model is the balance of momentum. Due to the stationary of the energy and the neglect of gravity, the divergence of the Cauchy stress tensor  $\boldsymbol{\sigma}$  is zero,

$$\operatorname{div}(\boldsymbol{\sigma}) = \mathbf{0} \quad , \quad \text{where} \quad \boldsymbol{\sigma} = \frac{d\psi}{d\boldsymbol{\varepsilon}} = (s^2 + \eta) \mathbf{C} \boldsymbol{\varepsilon}. \quad (4.7)$$

## 4.2 Evolution Law

The variational formulation of brittle fracture by Bourdin [14] is similar to a phase field model. For the propagation of the crack interface, an evolution equation is required and was derived by the work of [34].

### 4.2.1 Thermodynamical Background

The consistent material law for the evolution equation of the order parameter is based on the work of [19]. Thereby, the material model depends on the free energy on the internal variable

and its gradient. The process starts with the consideration of the micro force system with the stress vector  $\boldsymbol{\xi}$  and the internal and external forces  $\pi$  and  $\gamma$ , respectively. The work of the system for a considered volume  $\mathcal{P}_t$  is

$$\mathcal{W}_{\text{mic}}(\mathcal{P}_t) = \int_{\partial\mathcal{P}_t} \boldsymbol{\xi} \cdot \mathbf{n} \dot{s} \, dA + \int_{\mathcal{P}_t} \gamma_{\text{mic}} \dot{s} \, dV. \quad (4.8)$$

The work of the internal micro force  $\pi$  does not enter this external work. The system of micro forces is consistent with the global micro force balance

$$\int_{\partial\mathcal{P}_t} \boldsymbol{\xi} \cdot \mathbf{n} \, dA + \int_{\mathcal{P}_t} (\gamma_{\text{mic}} + \pi) \, dV, \quad (4.9)$$

or equivalently the local micro force balance

$$\text{div}(\boldsymbol{\xi}) + \gamma_{\text{mic}} + \pi = 0 \quad (4.10)$$

The sum of the work of the mechanical forces (Eq. 4.8) and the micro forces (Eq. 4.9) and therefore the Clausius-Planck inequality (Eq. 2.37) yields

$$\mathcal{D}_{\text{loc}} = \int_{\mathcal{P}_t} \left[ \boldsymbol{\sigma} : \mathbf{d} + \boldsymbol{\xi} \cdot \nabla \dot{s} - \pi \dot{s} - \rho \left( \dot{\psi}^* + \dot{\theta} S^* \right) \right] dV \geq 0. \quad (4.11)$$

This can be simplified to

$$\mathcal{D}_{\text{loc}} = \int_{\mathcal{P}_t} \left( \boldsymbol{\sigma} : \mathbf{d} + \boldsymbol{\xi} \cdot \nabla \dot{s} - \pi \dot{s} - \dot{\psi} \right) dV \geq 0 \quad (4.12)$$

by assuming small strains and isothermal conditions. The free energy density  $\psi$  is considered a function with dependence on the strain  $\boldsymbol{\varepsilon}$ , crack field  $s$  and gradient  $\nabla s$ , which results in its time derivative

$$\dot{\psi}(\boldsymbol{\varepsilon}, s, \nabla s) = \frac{\partial \psi}{\partial \boldsymbol{\varepsilon}} : \dot{\boldsymbol{\varepsilon}} + \frac{\partial \psi}{\partial \nabla s} : \nabla \dot{s} + \frac{\partial \psi}{\partial s} \cdot \dot{s}. \quad (4.13)$$

Eq. (4.12) gains the form

$$\int_{\mathcal{P}} \left[ \left( \boldsymbol{\sigma} - \frac{\partial \psi}{\partial \boldsymbol{\varepsilon}} \right) : \dot{\boldsymbol{\varepsilon}} + \left( \boldsymbol{\xi} - \frac{\partial \psi}{\partial \nabla s} \right) : \nabla \dot{s} - \left( \pi + \frac{\partial \psi}{\partial s} \right) \cdot \dot{s} \right] dV \geq 0 \quad (4.14)$$

by inserting Eq. (4.13). The inequality yields the constitutive relation with the assumption that the strain rate is independent of fracture field rate. The fracture field dependent terms form

$$- \int_{\mathcal{P}} \left[ \frac{\partial \psi}{\partial s} - \text{div} \left( \frac{\partial \psi}{\partial \nabla s} \right) + \underbrace{(-\gamma_{\text{mic}})}_{=\nabla \cdot \boldsymbol{\xi} + \pi} \right] \dot{s} \, dV + \int_{\partial\mathcal{P}} \left( \boldsymbol{\xi} - \frac{\partial \psi}{\partial \nabla s} \right) \dot{s} \cdot \mathbf{n} \, dA \geq 0 \quad (4.15)$$

with the divergence theorem. The micro stress  $\boldsymbol{\xi}$  yield

$$\boldsymbol{\xi} = \frac{\partial \psi}{\partial \nabla s} = 2l_c \nabla s \quad (4.16)$$

to fulfil the Eq. (4.15) independent of the fracture field rate. The variational derivative of  $\psi$  with respect to the fracture field is

$$-\frac{\partial\psi}{\partial s} - \operatorname{div} \left( \frac{\partial\psi}{\partial \nabla s} \right) = -\frac{\delta\psi}{\delta s} \geq 0 \quad (4.17)$$

for cases without external micro forces. A subsequent consistent evolution equation in its most general form [34] is

$$\dot{s} = -M \frac{\delta\psi}{\delta s} = -M \left[ s \boldsymbol{\varepsilon} \cdot [\mathbf{C} \boldsymbol{\varepsilon}] - \mathcal{G}_c \left( 2l_c \nabla s + \frac{1-s}{2l_c} \right) \right] \quad (4.18)$$

and corresponds to the Ginzburg-Landau Equation. The symbol " $\delta$ " represents the variational derivation. This means, that the rate  $\dot{s}$  requires the variational derivative of the total energy density. Another quantity is the mobility parameter  $M$ , which controls the rate of the phase field and the dissipation in the process zone [40]. For the analysis of Griffith-like fracture problems, the value  $M$  has to be sufficiently large, [42].

### 4.2.2 Irreversibility

At last, an irreversibility condition should be implemented. There are two major approaches that are extensively used in the literature to prevent crack healing in phase field models: the imposition of a Dirichlet boundary condition or an enforced negative sign of the phase field time derivate  $\dot{s} < 0$ . In the following work we apply a Dirichlet boundary condition, see e.g. [40] for details.

In comparison to other phase field models, the fracture phase field is of an irreversible type. In general, the two formulations are thermodynamically consistent and can ensure the irreversibility of the model. The straightforward approach is the restriction of the direction of the phase transformation by demanding a phase field time derivative smaller than zero, e.g.

$$\dot{s} \leq 0. \quad (4.19)$$

This was proposed by Miehe et al. [52] and [13]. The condition is physically sound but very restrictive and therefore brings technical difficulties, e.g., a slow convergence rate in numerical simulations, which is the result of the prevention of minimal increases in phase field values in areas with no crack representation. Therefore, Kuhn [40] presented another procedure to ensure irreversibility

$$s(\boldsymbol{x}, t > t^*) = 0 \quad \text{if} \quad s(\boldsymbol{x}, t^*) = 0. \quad (4.20)$$

In the following, the second definition is applied.

## 4.3 Consideration of the Tension and Compression Asymmetry of Cracks

The original form is based on assumptions targeting linear elastic material, small deformation and quasi-static cases. One major deficiency is the missing difference in the material separation due to the tension and compression of the material. This property becomes relevant in cases of region under compression near crack surfaces or propagating cracks but can be tolerated in case of pure tension. The reason for this extension lies in the prevention of unphysical

model behaviour, e.g. penetrability of crack surface in case of contact and crack growth in a purely compressed region. To consider this, two approaches, the deviatoric decomposition [5] (VDD) and spectral decomposition [52] (SD) are shortly discussed in the following. The approaches are widely used and do not require a crack surface tracking, which also accounts for their efficiency. They rely on the decomposition of the strain energy density into a positive and negative part, which is first presented in Del Piero et al. [22]. The mentioned formulations are variationally consistent and are independent of the crack orientation.

$$\langle x \rangle_{+/-} = \begin{cases} x & \text{if } x \geq / < 0 \\ 0 & \text{else} \end{cases} \quad (4.21)$$

The following introduced derived models are not  $\Gamma$ -convergent, in contrast to the original phase field model [26].

### Volumetric-Deviatoric Decomposition of the Strain Energy Density

The key value for the assumption of crack opening or crack closing for the VDD by [5] is the volume dilatation

$$\varepsilon_V = \text{tr}(\varepsilon). \quad (4.22)$$

The evaluation condition is a if-condition, i.e.

$$\text{tr}(\varepsilon) \geq 0, \quad \Rightarrow \quad \text{open crack} \quad (4.23)$$

$$\text{tr}(\varepsilon) < 0, \quad \Rightarrow \quad \text{closed crack.} \quad (4.24)$$

The crack closes in case the volume elements are under volume contraction, the regions near the crack becomes closed. Otherwise, the crack is open. The energy functional reads

$$\psi^e = g(s) \left( \underbrace{\frac{K}{2} \langle \text{tr}(\varepsilon) \rangle_+^2 + \mu (\mathbf{e} : \mathbf{e})}_{\psi_+^e} \right) + \underbrace{\frac{K}{2} \langle \text{tr}(\varepsilon) \rangle_-^2}_{\psi_-^e}. \quad (4.25)$$

The associated constitutive law gains the form

$$\boldsymbol{\sigma} = \frac{\partial \psi_e}{\partial \boldsymbol{\varepsilon}} = g(s) [K \langle \text{tr}(\varepsilon_-) \rangle_+ \mathbf{1} + 2\mu \mathbf{e}] + K \langle \text{tr}(\varepsilon) \rangle_- \mathbf{1}. \quad (4.26)$$

However, a positive volumetric deformation is not sufficient for a crack to open, but a simple shear sliding motion of the crack faces is accompanied by a purely deviatoric deformation which allows the VDD formulation as a satisfactory model to describe Mode II fracture.

### Spectral Decomposition of the Strain Energy Density

The spectral decomposition (SD) proposed in [52] relies on the spectral decomposition of the linearised elastic strain tensor

$$\boldsymbol{\varepsilon} = \sum_{i=1}^n \varepsilon_i \mathbf{n}_i \otimes \mathbf{n}_i, \quad (4.27)$$

whereby  $\varepsilon_i$  is the  $i$ -th eigenvalue of the strain tensor  $\boldsymbol{\varepsilon}$  and  $\mathbf{n}_i$  is the associated normalized eigenvector. The strain energy density yields

$$\psi^e = g(s) \left( \underbrace{\frac{\lambda}{2} \langle \text{tr}(\boldsymbol{\varepsilon}) \rangle_+^2 + \mu(\boldsymbol{\varepsilon}_+ : \boldsymbol{\varepsilon}_+)}_{\psi_+^e} \right) + \frac{\lambda}{2} \underbrace{\langle \text{tr}(\boldsymbol{\varepsilon}) \rangle_-^2 + \mu(\boldsymbol{\varepsilon}_- : \boldsymbol{\varepsilon}_-)}_{\psi_-^e} \quad (4.28)$$

The positive or negative strain components of the spectral decomposition are defined by

$$\boldsymbol{\varepsilon}_{+/-} = \sum_{i=1}^n \{\varepsilon_i\}_{+/-} \mathbf{n}_i \otimes \mathbf{n}_i. \quad (4.29)$$

The constitutive law for the SD formulation yields

$$\boldsymbol{\sigma} = g(s) \left[ \lambda \langle \text{tr}(\boldsymbol{\varepsilon}) \rangle_+ \mathbf{1} + 2\mu \boldsymbol{\varepsilon}_+ \right] + \lambda \langle \text{tr}(\boldsymbol{\varepsilon}) \rangle_- \mathbf{1} + 2\mu \boldsymbol{\varepsilon}_-. \quad (4.30)$$

Since the model partly shares the crack closure criterion of the VDD formulation, it also keeps the previously mentioned weaknesses. The choice of the tension-compression asymmetry for the following is the volumetric-deviatoric decomposition.



## Chapter 5

# Finite Element Implementation

This chapter provides the layout for the implementation of the fracture phase field, for 2d and 3d problems, using the numerical framework of the Finite Element Method (FEM). For this, (4.7) (4.18), (4.26), (2.8) and (4.30) are used. The foundation for the FEM can be found in Bathe and Mohasseb [8], Zienkiewicz, Taylor and Zhu [79], Wriggers [76] and Hughes [37]. Furthermore, the main topic of this work, the exponential shape functions, is introduced in this chapter.

### 5.1 Weak Forms and Spatial Discretization

The FEM solution scheme begins with an approximation of the domain  $\mathcal{B}$ ,

$$\mathcal{B} \approx \mathcal{B}^e = \bigcup_{e=1}^{n_e} \Omega_e \quad (5.1)$$

with  $n_e$  number of finite elements  $\Omega_e$ , which are a decomposition of the discretized domain  $\mathcal{B}^e$ . It is based on the associated variational formulation or on a weak formulation. The equations used in the model are the equilibrium of the mechanical forces and the evolution equation. The weak form is produced by multiplying these equations with a test function  $\delta \mathbf{u}$  and  $\delta s$  of the displacement  $\mathbf{u}$  and fracture phase field  $s$ . In the second step, the result is integrated over the space. To reduce the order of the derivatives to a minimum integration by parts is used. This results in

$$\int_{\Omega} [-(\nabla \delta \mathbf{u})^T : \boldsymbol{\sigma} + \delta \mathbf{u} \cdot \mathbf{f}] dV + \int_{\partial \Omega_t} \delta \mathbf{u} \cdot \mathbf{t}^* dA = 0 \quad (5.2)$$

and

$$\int_{\Omega} - \left[ \delta s \frac{\dot{s}}{M} + \nabla \delta s \cdot 2 \mathcal{G}_c l_c \nabla s + \delta s \left( s \boldsymbol{\varepsilon} : [\mathbf{C} \boldsymbol{\varepsilon}] - \frac{\mathcal{G}_c}{2l_c} (1 - s) \right) \right] dV = 0 \quad (5.3)$$

For the approximation of the variable values  $\mathbf{u}$ ,  $\delta \mathbf{u}$ ,  $s$  and  $\delta s$  over the domain  $\Omega$ , scalar shape functions  $N_I$  are used. In general, these functions are independent from each other and can be chosen separately. In the standard case the shape functions are the same. In the following case, the shape functions of the virtual and real values are chosen to be identical, but they can differ for the primary fields  $\mathbf{u}$  and  $s$ . The notation with an underbar and represented in matrix notation are used for the discretized quantities, which are on the element level

$$\underline{\mathbf{u}}_h = \sum_{I=1}^N N_I^u \underline{\mathbf{u}}_I, \quad \delta \underline{\mathbf{u}}_h = \sum_{I=1}^N N_I^{\delta u} \delta \underline{\mathbf{u}}_I, \quad (5.4)$$

$$s_h = \sum_{I=1}^N N_I^s s_I, \quad \text{and} \quad \delta s_h = \sum_{I=1}^N N_I^{\delta s} \delta s_I. \quad (5.5)$$

Due to the second-order weak form, the gradients of  $\mathbf{u}$  and  $s$  are required. The discretized form requires the derivatives of the shape functions. For the 3-dimensional case, the derivatives can be written as

$$\underline{\mathbf{B}}_I^u = \begin{bmatrix} N_{I,1}^u & 0 & 0 \\ 0 & N_{I,2}^u & 0 \\ 0 & 0 & N_{I,3}^u \\ 0 & N_{I,3}^u & N_{I,1}^u \\ N_{I,3}^u & 0 & N_{I,1}^u \\ N_{I,2}^u & N_{I,1}^u & 0 \end{bmatrix} \quad \text{and} \quad \underline{\mathbf{B}}_I^s = \begin{bmatrix} N_{I,1}^s \\ N_{I,2}^s \\ N_{I,3}^s \end{bmatrix}. \quad (5.6)$$

The highlighted rows and columns are omitted in the case of a 2-dimensional problem. The weak form of Eq. (5.2) and Eq. (5.3) reads

$$\sum_{I=1}^N (\delta \underline{\mathbf{u}}_I)^T \left[ \int_{\Omega} \left( - [\underline{\mathbf{B}}_I^{\delta u}]^T \underline{\boldsymbol{\sigma}}_h + N_I^{\delta u} \underline{\mathbf{f}}_h \right) dV + \int_{\partial\Omega_t} N_I^{\delta u} \underline{\mathbf{t}}_h^* dA \right] = 0 \quad (5.7)$$

and

$$\sum_{I=1}^N \delta s_I \left[ - \int_{\Omega} N_I^{\delta s} \left( \frac{\dot{s}_h}{M} + s_h \underline{\boldsymbol{\varepsilon}}_h^T : [\underline{\mathbf{C}} \underline{\boldsymbol{\varepsilon}}_h] - \frac{\mathcal{G}_c}{2l_c} (1 - s_h) \right) + 2 [\underline{\mathbf{B}}_I^s]^T \mathcal{G}_c l_c \nabla s_h dV \right] = 0. \quad (5.8)$$

The terms (5.7) and (5.8) described the solution for the whole domain, while in practice, the equations are evaluated element-wise. The contribution of node  $I$  of element  $e$  to the total residual are

$$\underline{\mathbf{R}}_{I,e}^u = - \underbrace{\int_{\Omega_e} [\underline{\mathbf{B}}_I^{\delta u}]^T \underline{\boldsymbol{\sigma}}_h dV}_{\underline{\mathbf{P}}_{I,e}^u} + \underbrace{\int_{\Omega_e} N_I^{\delta u} \underline{\mathbf{f}}_h dV + \int_{\partial\Omega_e \cap \partial\Omega_t} N_I^{\delta u} \underline{\mathbf{t}}_h^* dA}_{\underline{\mathbf{F}}_{I,e}^u} \quad (5.9)$$

and

$$R_{I,e}^s = \underbrace{- \int_{\Omega_e} \left[ \mathbf{N}_I^{\delta s} \left( \frac{\dot{s}_h}{M} + s_h \underline{\boldsymbol{\varepsilon}}_h^T : [\underline{\mathbf{C}} \underline{\boldsymbol{\varepsilon}}_h] - \frac{\mathcal{G}_c}{2l_c} (1 - s_h) \right) + 2[\mathbf{B}_I^s]^T \mathcal{G}_c l_c \nabla s \right] dV}_{P_{I,e}^s}. \quad (5.10)$$

$\underline{\mathbf{P}}_{I,e}^u$  and  $P_{I,e}^s$  are the contributions resulting from the internal forces and  $\underline{\mathbf{F}}_{I,e}^u$  represents the external forces. The mechanical and crack field residuals are first assembled to

$$\underline{\mathbf{R}}_{I,e} = \left[ (\underline{\mathbf{R}}_{I,e}^u)^T \quad R_{I,e}^s \right]^T \quad (5.11)$$

and each nodal contribution is then again assembled to

$$\underline{\mathbf{R}}_e = \left[ (\underline{\mathbf{R}}_{I,e})^T \quad (\underline{\mathbf{R}}_{J,e})^T \quad \dots \right]^T \quad (5.12)$$

where the number of contributions depends on the number of nodes per element ( $n_{nen}$ ), which is in the used cases of quadrilateral ( $n_{nen} = 4$ ) or hexahedron ( $n_{nen} = 8$ ). The global residuum vector can be written as

$$\underline{\mathbf{R}} = \bigcup_{e=1}^{n_e} \underline{\mathbf{R}}_e = \left[ (\underline{\mathbf{R}}_1)^T \quad \dots \quad (\underline{\mathbf{R}}_N)^T \right]^T \quad (5.13)$$

and includes contributions from all elements. The nodal residuals are formed by

$$\underline{\mathbf{R}} = \sum_{e \in \mathcal{E}_I} \underline{\mathbf{R}}_{I,e}. \quad (5.14)$$

It is a sum of contributions from elements adjacent to node  $I$  and  $\mathcal{E}_I$  is the set of all elements of the domain  $\Omega_I$ . Besides the residual, the nodal values and their virtual counterparts are also assembled, i.e.,

$$\delta \underline{\mathbf{d}} = \left[ (\delta \underline{\mathbf{d}}_I)^T \quad \dots \quad (\delta \underline{\mathbf{d}}_N)^T \right]^T \quad \text{with} \quad \delta \underline{\mathbf{d}}_I = \left[ (\delta \underline{\mathbf{u}}_I)^T \quad s_I \right]^T \quad (5.15)$$

A concise form of (5.7) and (5.8) can be written as

$$(\delta \underline{\mathbf{d}})^T \underline{\mathbf{R}} = 0. \quad (5.16)$$

The virtual quantities  $\delta \underline{\mathbf{d}}$  stated in (5.16) must hold for any choice of  $\delta \underline{\mathbf{d}}$ , so for the residual of the global system of equations it has to hold that

$$\underline{\mathbf{R}} = \underline{\mathbf{0}} \quad \Leftrightarrow \quad \underline{\mathbf{R}}_I = \underline{\mathbf{0}} \quad \text{for} \quad I = 1, \dots, N. \quad (5.17)$$

## 5.2 Time Discretization and Iterative Solution

In order to employ the finite element method to numerically solve a phase field fracture problem, we have to derive the weak forms of (5.2) and (5.3). The approximation of actual and virtual fields of the displacement and crack state is done via  $C_0$  continuous shape functions, which are introduced above. Further details are given in [40]. The global system can be described in form of a residual  $\underline{\mathbf{R}}$  by the equation

$$\underline{\mathbf{R}} = \underline{\mathbf{F}} - \underline{\mathbf{P}}(\underline{\mathbf{d}}, \dot{\underline{\mathbf{d}}}) = \underline{\mathbf{0}}, \quad (5.18)$$

with the internal and external forces  $\underline{\mathbf{P}}$  and  $\underline{\mathbf{F}}$ , respectively. The global vector of degrees of freedom  $\underline{\mathbf{d}}$  is written as

$$\underline{\mathbf{d}} = [(\underline{\mathbf{d}}_I)^T \ \dots \ (\underline{\mathbf{d}}_N)^T]^T \quad \text{with} \quad \underline{\mathbf{d}}_I = [\underline{\mathbf{u}}_I^T \ s_I]^T. \quad (5.19)$$

The non-linear system

$$\underline{\mathbf{R}}_{n+1} = \underline{\mathbf{F}}_{n+1} - \underline{\mathbf{P}}(\underline{\mathbf{d}}_{n+1}, \dot{\underline{\mathbf{d}}}_{n+1}) = \underline{\mathbf{0}}. \quad (5.20)$$

is solved for each time step. For the time integration, an implicit Euler time integration scheme is applied to approximate the velocities of the degrees of freedom as

$$\dot{\underline{\mathbf{d}}}_{n+1} = \frac{\underline{\mathbf{d}}_{n+1} - \underline{\mathbf{d}}_n}{\Delta t_n}. \quad (5.21)$$

With this, the discretized residual at the time  $t_{n+1}$  reads

$$\underline{\mathbf{R}}_{n+1}(\underline{\mathbf{F}}_{n+1}, \underline{\mathbf{d}}_{n+1}, \underline{\mathbf{d}}_n) = \underline{\mathbf{F}}_{n+1} - \underline{\mathbf{P}}(\underline{\mathbf{d}}_{n+1}, \underline{\mathbf{d}}_n) = \underline{\mathbf{0}}. \quad (5.22)$$

The solution  $\underline{\mathbf{d}}_{n+1}$  for the non-linear system of equations is derived by using the Newton-Raphson method. The first step is the initialization with either defined values for the first time step or the result of the previous iteration

$$\underline{\mathbf{d}}_{n+1}^{(k+1)} = \underline{\mathbf{d}}_{n+1}^{(k)} + \Delta \underline{\mathbf{d}}_{n+1}^{(k)}. \quad (5.23)$$

The increment  $\Delta \underline{\mathbf{d}}_{n+1}^{(k)}$  results from the linearized system of equations

$$\underline{\mathbf{R}}_{n+1}^{(k+1)} \approx \underline{\mathbf{R}}_{n+1}^{(k)} - \underline{\mathbf{S}}_{n+1}^{(k)} \Delta \underline{\mathbf{d}}_{n+1}^{(k)} = \underline{\mathbf{0}}. \quad (5.24)$$

Therefore, the system matrix  $\underline{\mathbf{S}}$  is required and is obtained by differentiation of the internal forces  $\underline{\mathbf{P}}$ , i.e.

$$\underline{\mathbf{S}}_{n+1}^{(k)} = \frac{\partial \hat{\underline{\mathbf{P}}}_{n+1}}{\partial \underline{\mathbf{d}}_{n+1}}(\underline{\mathbf{d}}_{n+1}^{(k)}, \underline{\mathbf{d}}_n). \quad (5.25)$$

Due to the transient character of the equations, a time discretization scheme is required, which is achieved by the Euler scheme and yields

$$\underline{\mathbf{S}}_{n+1}^{(k)} = \frac{\partial \hat{\underline{\mathbf{P}}}_{n+1}}{\partial \underline{\mathbf{d}}_{n+1}} = \frac{\partial \underline{\mathbf{P}}_{n+1}}{\partial \underline{\mathbf{d}}_{n+1}}(\underline{\mathbf{d}}_n, \dot{\underline{\mathbf{d}}}_{n+1}) = \underbrace{\frac{\partial \underline{\mathbf{P}}_{n+1}}{\partial \underline{\mathbf{d}}_{n+1}}}_{\underline{\mathbf{K}}} + \frac{1}{\Delta t_n} \underbrace{\frac{\partial \underline{\mathbf{P}}_{n+1}}{\partial \dot{\underline{\mathbf{d}}}_{n+1}}}_{\underline{\mathbf{D}}}. \quad (5.26)$$

The computed system matrix  $\underline{\mathbf{S}}$  contains the stiffness matrix  $\underline{\mathbf{K}}$  as well as a damping matrix  $\underline{\mathbf{D}}$  multiplied by a time increment  $\Delta t$ . In summary, the consideration on element level of the

stiffness matrix

$$\underline{\mathbf{K}}_{IJ,e} = \int_{\Omega_e} \begin{bmatrix} [\underline{\mathbf{B}}_I^{\delta u}]^T (s^2 + \eta) \underline{\mathbf{C}} \underline{\mathbf{B}}_J^u & [\underline{\mathbf{B}}_I^{\delta u}]^T 2 s \underline{\mathbf{C}} \underline{\boldsymbol{\varepsilon}}_h N_J^s \\ N_I^{\delta s} 2 s (\underline{\mathbf{C}} \underline{\boldsymbol{\varepsilon}}_h)^T \underline{\mathbf{B}}_J^u & [\underline{\mathbf{B}}_I^{\delta s}]^T 2 \mathcal{G}_c l_c \underline{\mathbf{B}}_J^s \\ & + N_I^{\delta s} \left( \underline{\boldsymbol{\varepsilon}}_h^T \underline{\mathbf{C}} \underline{\boldsymbol{\varepsilon}} + \frac{\mathcal{G}_c}{2l_c} \right) N_J^s \end{bmatrix} dV, \quad (5.27)$$

the damping matrix

$$\underline{\mathbf{D}}_{IJ,e} = \int_{\Omega_e} \begin{bmatrix} \underline{\mathbf{0}} & \underline{\mathbf{0}} \\ \underline{\mathbf{0}} & N_I^{\delta s} \frac{1}{M} N_J^s \end{bmatrix} dV. \quad (5.28)$$

and the nodal residual

$$\underline{\mathbf{R}}_{I,e} = \int_{\Omega_e} \begin{bmatrix} [\underline{\mathbf{B}}_I^{\delta u}]^T \underline{\boldsymbol{\sigma}} \\ N_I^{\delta s} \frac{\dot{s}}{M} - 2 \mathcal{G}_c l_c [\underline{\mathbf{B}}_I^{\delta s}]^T \nabla s + N_I^{\delta s} \left( s \underline{\boldsymbol{\varepsilon}}_h^T \underline{\mathbf{C}} \underline{\boldsymbol{\varepsilon}} + \frac{\mathcal{G}_c}{2l_c} (s - 1) \right) \end{bmatrix} dV \quad (5.29)$$

are necessary. The indices  $IJ$  denote the contribution of the different nodes. The chapter 6 is concerned with the adaptive numerical integration of these terms. The focus lies on the accurate integration of shape functions  $N_I^s$  and their derivatives  $\underline{\mathbf{B}}_I^s$  that are used for the approximation of the phase field  $s$ .

### 5.3 2d/3d Isoparametric Representation

The conventional element shapes for finite elements are triangles, quadrilaterals, tetrahedrons, prisms, and hexahedrons. This work is limited to quadrilateral and hexahedral elements.

The smallest units of a finite element analysis are its elements. In order to approximate differently shaped domains the elements have to be distorted to approximate the geometry. The geometry of the elements varies, which requires a general approach for a flexible implementation the isoparametric concept is applied, which uses the same shape functions for the representation of the element geometry as for the nodal degrees of freedom. The usual choice is bilinear Lagrangian shape functions for 3d hexahedron elements with the formula

$$N_i^{\text{lin}}(\xi, \eta, \zeta) = \frac{1}{2}(1 + \xi_i \xi) \frac{1}{2}(1 + \eta_i \eta) \frac{1}{2}(1 + \zeta_i \zeta) , \quad i = 1, \dots, n_{\text{element}}. \quad (5.30)$$

Thereby, for each of the nodes, a function exists as indicated by  $i$ . The numbers indicated by  $i$  are used for the element in its natural coordinate system, see Fig. 5.1 for 2d and Fig. 5.2 for 3d. The description of an arbitrary element for its global form is

$$\mathbf{x} = \sum_{i=1}^{n_{\text{element}}} N_i^{\text{lin}}(\xi, \eta, \zeta) \mathbf{x}_i \quad (5.31)$$

whereby each node coordinate  $\mathbf{x}_i$  is multiplied with its corresponding shape function  $N_i$ .

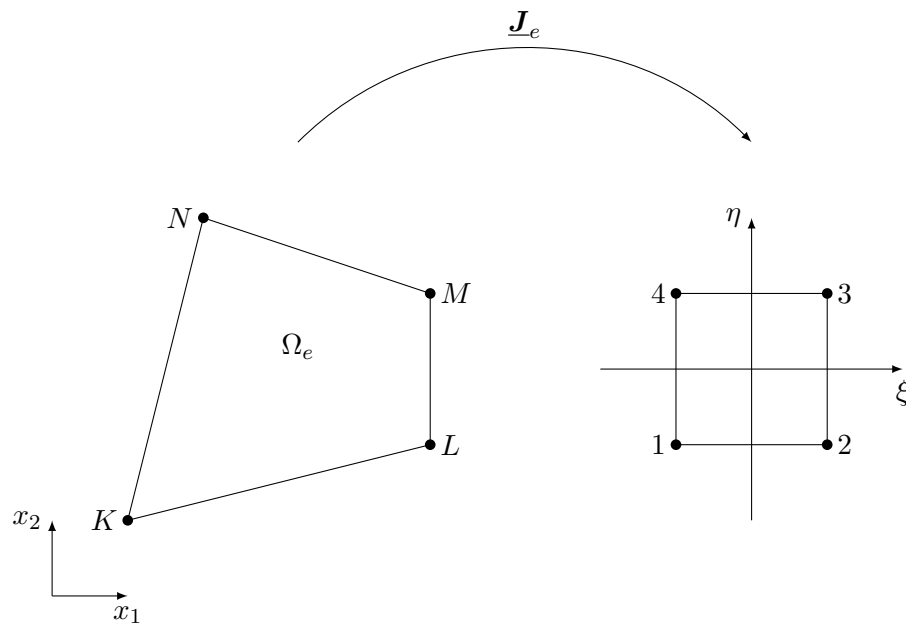


FIGURE 5.1: Actual (left) and 2d Isoparametric(right) of an arbitrarily defined quadrilateral element.

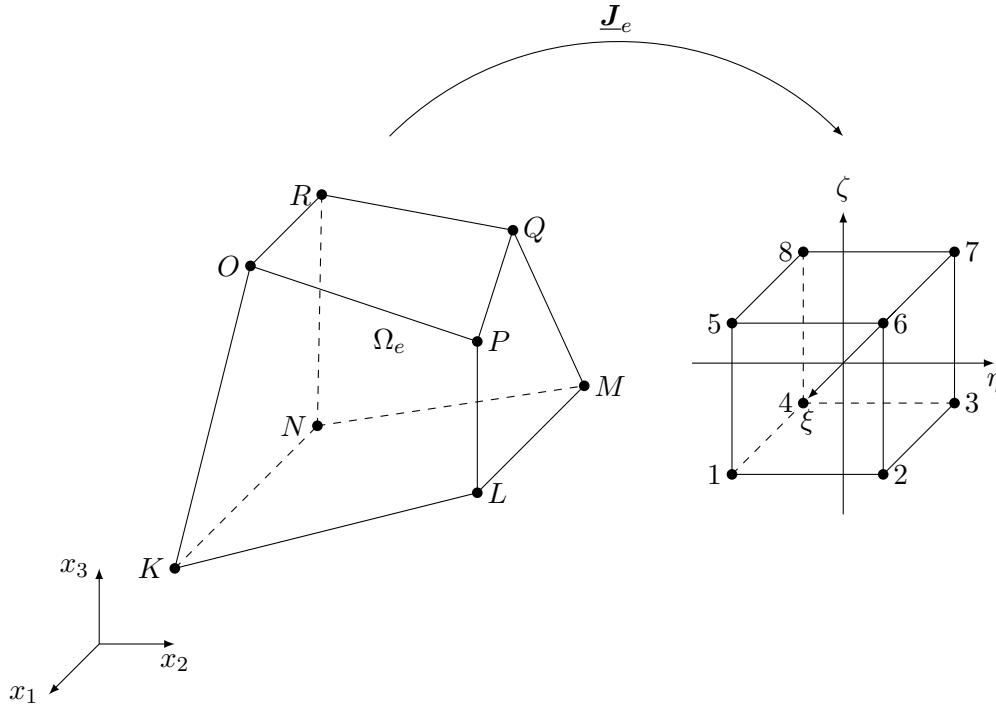


FIGURE 5.2: Actual (left) and 3d Isoparametric (right) of an arbitrarily defined cuboid element.

$$\left[ \frac{\partial N_I}{\partial \xi} \right]^T = \left[ \frac{\partial \underline{x}_e}{\partial \xi} \right]^T \left[ \frac{\partial N_I}{\partial \underline{x}_e} \right]^T = \mathbf{J}_e \left[ \frac{\partial N_I}{\partial \underline{x}_e} \right]^T \quad (5.32)$$

For the description of derivatives in the weak form in the finite element method, the shape functions need to be differentiated concerning the physical coordinates  $\underline{x}_e$ . Since the shape functions are defined in the natural coordinate system  $\xi$ , the chain rule is applied to obtain the required derivatives,

$$\mathbf{J}_e = \sum_{i=1}^{\text{nen}} \begin{bmatrix} N_{i,\xi} x_{1i} & N_{i,\xi} x_{2i} & N_{i,\xi} x_{3i} \\ N_{i,\eta} x_{1i} & N_{i,\eta} x_{2i} & N_{i,\eta} x_{3i} \\ N_{i,\zeta} x_{1i} & N_{i,\zeta} x_{2i} & N_{i,\zeta} x_{3i} \end{bmatrix}. \quad (5.33)$$

The determinant of the Jacobian is positive ( $\det \mathbf{J} > 0$ ), if the mapping is unique, invertible and orientation preserving.

## 5.4 Exponential Finite Elements

### 5.4.1 Introduction

The approximation of cracks with a phase field model requires narrow transition zones, in order to represent a fractured elastic body accurately. Due to the high gradients arising at crack surfaces, a fine discretization is necessary for a sufficient approximation of these gradients and the surface energy. This leads to a high computing time [46][42] [43].

To approximate cracks without a very fine discretization Kuhn and Müller [42] introduced exponential shape functions to approximate the phase field variable. The choice of the exponential functions as shape functions for the fracture phase field is motivated by the analytical solution for a fractured 1d bar, see Fig. 5.3.

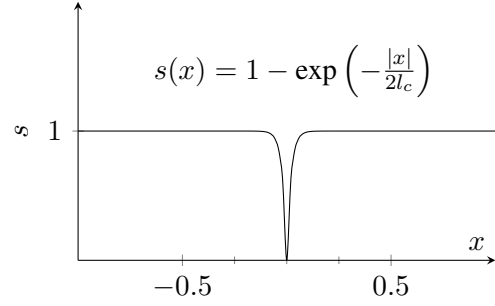


FIGURE 5.3: Analytical 1d solution of a stationary crack.

The 1d linear and exponential shape functions are defined as functions of the natural coordinates  $\xi \in [-1, 1]$ , see Fig. 5.4. They are defined as

$$\begin{aligned} N_1^{\text{lin}}(\xi) &= \frac{1}{2}(1 - \xi), & N_1^{\text{exp}}(\xi, \delta) &= 1 - \frac{\exp(-\delta(1 + \xi)/4) - 1}{\exp(-\delta/2) - 1}, \\ N_2^{\text{lin}}(\xi) &= \frac{1}{2}(1 + \xi) \quad \text{and} & N_2^{\text{exp}}(\xi, \delta) &= \frac{\exp(-\delta(1 + \xi)/4) - 1}{\exp(-\delta/2) - 1}. \end{aligned} \quad (5.34)$$

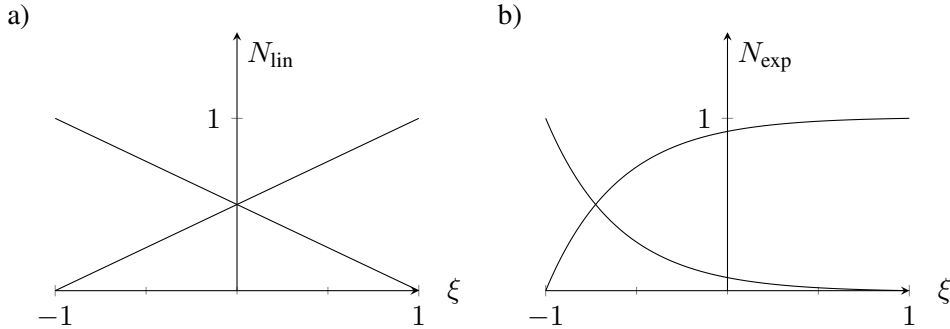


FIGURE 5.4: a) Linear and b) exponential shape functions for a 1d element with two nodes.

The exponential shape functions are parametrized via  $\delta = h/l_c$  in order to capture the typical 1d solution accurately. The applicability of 1d exponential shape functions will be verified by an approximation of the analytical solution of a stationary crack displayed in Fig. 5.3. The analytical solution is derived from the surface energy  $E^s$  of (4.18) with the boundary conditions  $s'(\pm 1) = 0$  and  $s(0) = 0$  in the domain  $x \in [-1, 1]$ . Due to the stationary approximation of a crack, the displacement field becomes irrelevant.

The orientation of the exponential shape functions can be easily chosen for stationary cracks. Depending on the sign of the gradient according to the spatial coordinate direction, the direction can be adapted. In the beginning of an emerging crack, the gradient of the phase field is less steep, therefore the process becomes ambiguous. Since the orientation of the exponential shape functions significantly influences the propagation direction, it should be chosen with caution.

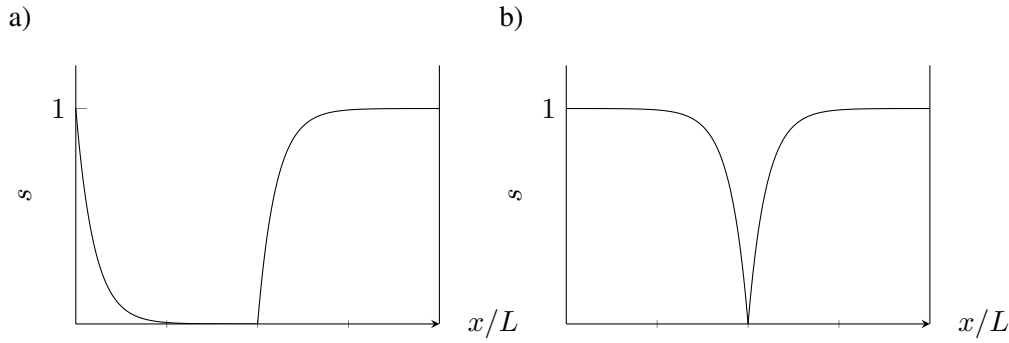


FIGURE 5.5: a) Without reorientation and b) with the orientation of the exponential shape functions at a crack.

In comparison to the linear shape functions, the exponential functions can describe the diffuse 1d crack surface more efficiently, see Fig. 5.6. The graph displays the numerical solutions for a stationary 1D space (elastic body) with a crack at  $x = 0$ , defined by the Dirichlet boundary condition  $s(x = 0) = 0$  for different choices of shape functions.

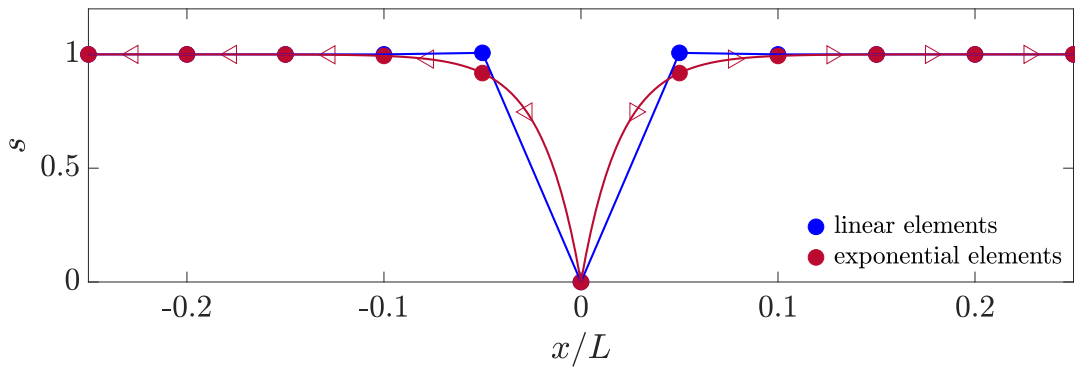


FIGURE 5.6: Fracture field  $s$  for a 1d body with a stationary crack at  $x = 0$ .

To obtain the exponential shape functions for the analysis of two- or three-dimensional problems, the 1d shape functions can simply be composed as described in [79] for Lagrange elements. Thereby, the linear combination of these 1d shape functions is combined for different spatial coordinates and the consideration of the allocation of the 1d nodal shape function to the 2d or 3d node in dependence of the adjoining edges. In this regard, the exponential shape functions need particular attention, because the element edge lengths in the shape functions need to be consistent, see e.g. [42]. The great advantage of the exponential elements is the good approximation of steep gradients even for low mesh densities. Unfortunately, there are some drawbacks. The major problem is that the elements have to be oriented properly. Due to the asymmetry of the exponential shape functions, the fracture field  $s$  would also be incorrectly asymmetrical if the shape functions are not oriented properly. This deficiency can be resolved by an adaptive reorientation of the local coordinates according to the nodal values of  $s$  if necessary, see e.g. [42]. As an example, this simple technique is indicated in Fig. 5.6. The orientation of the elements in the spatial domain  $x < 0$  is illustrated by the orientation of the triangles (normal  $\triangleright$  and reversed  $\triangleleft$  orientation). Accordingly, an orientation is introduced in the description of the phase field variable.

### 5.4.2 2d Exponential Shape Functions

The 2d exponential shape functions can be generated from the linear shape functions by multiplying their 1d form, which results in

$$\begin{aligned}\bar{N}_1^{\text{exp}}(\xi, \eta, \delta_k) &= N_1^{\text{exp}}(\xi, \delta_1) \cdot N_1^{\text{exp}}(\eta, \delta_4), \\ \bar{N}_2^{\text{exp}}(\xi, \eta, \delta_k) &= N_2^{\text{exp}}(\xi, \delta_1) \cdot N_1^{\text{exp}}(\eta, \delta_2), \\ \bar{N}_3^{\text{exp}}(\xi, \eta, \delta_k) &= N_2^{\text{exp}}(\xi, \delta_3) \cdot N_2^{\text{exp}}(\eta, \delta_2) \quad \text{and} \\ \bar{N}_4^{\text{exp}}(\xi, \eta, \delta_k) &= N_1^{\text{exp}}(\xi, \delta_3) \cdot N_2^{\text{exp}}(\eta, \delta_4).\end{aligned}\tag{5.35}$$

Thereby, the elements contain instead of one, four  $\delta$  values for each edge. The variable  $k$  defines the edge number and is used to compute the exponential parameter, according to  $\delta_k = \frac{h_k}{l_c}$ . The convention of the linear element, see Fig. 5.1 can be adopted. The mentioned orientation issue for the 2d case will be discussed in chapter 7. The shape functions possess the Kronecker delta property, i.e.  $\bar{N}_i^{\text{exp}}(\xi_j, \eta_j, \delta_k) = \delta_{ij}$ . Based on the premise that the orientation of all shape functions is in each element equal the continuity of the approximation of the degree of freedom across the mesh is given. Compared to the elements with linear or 2d bilinear shape functions, the exponential shape functions do not always fulfil the partition of unity. In the case

$$\delta_1 \neq \delta_3 \quad \text{or} \quad \delta_2 \neq \delta_4,\tag{5.36}$$

the partition of unity is violated. The description of the partition of unity is the summation of all shape functions in the whole element domain to one. This reads

$$\sum_{i=1}^4 \bar{N}_i^{\text{exp}}(\xi, \eta, \delta_k) = 1 - \underbrace{[N_1^{\text{exp}}(\xi, \delta_1) - N_1^{\text{exp}}(\xi, \delta_3)] \cdot [N_1^{\text{exp}}(\eta, \delta_2) - N_1^{\text{exp}}(\eta, \delta_4)]}_{=R(\xi, \eta, \delta_i)}.\tag{5.37}$$

The residual term  $R$  is required to be zero. An example of a residual  $R$  is depicted in Fig. 5.7. The form of the coloured domain corresponds to the shape of the observed element. The crack width is  $L/5$ . The residual is only zero at the edges.

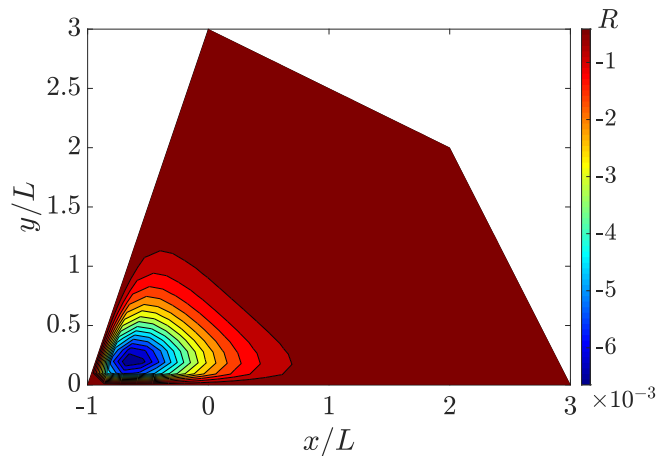


FIGURE 5.7: The residual term  $R$  over the global element geometry for a regular orientated exponential element.

In order to ensure the partition of unity a simple modification is performed by distributing the residual term equally over all shape functions, according to

$$N_i^{\text{exp}}(\xi, \eta, \delta_k) = \bar{N}_i^{\text{exp}}(\xi, \eta, \delta_k) + \frac{1}{4}R(\xi, \eta, \delta_k) \quad \text{for } i = 1, \dots, 4. \quad (5.38)$$

This process ensures the same exponential approximation of the crack surface independent of the shape of the quadrilateral elements, see Fig. 5.8.

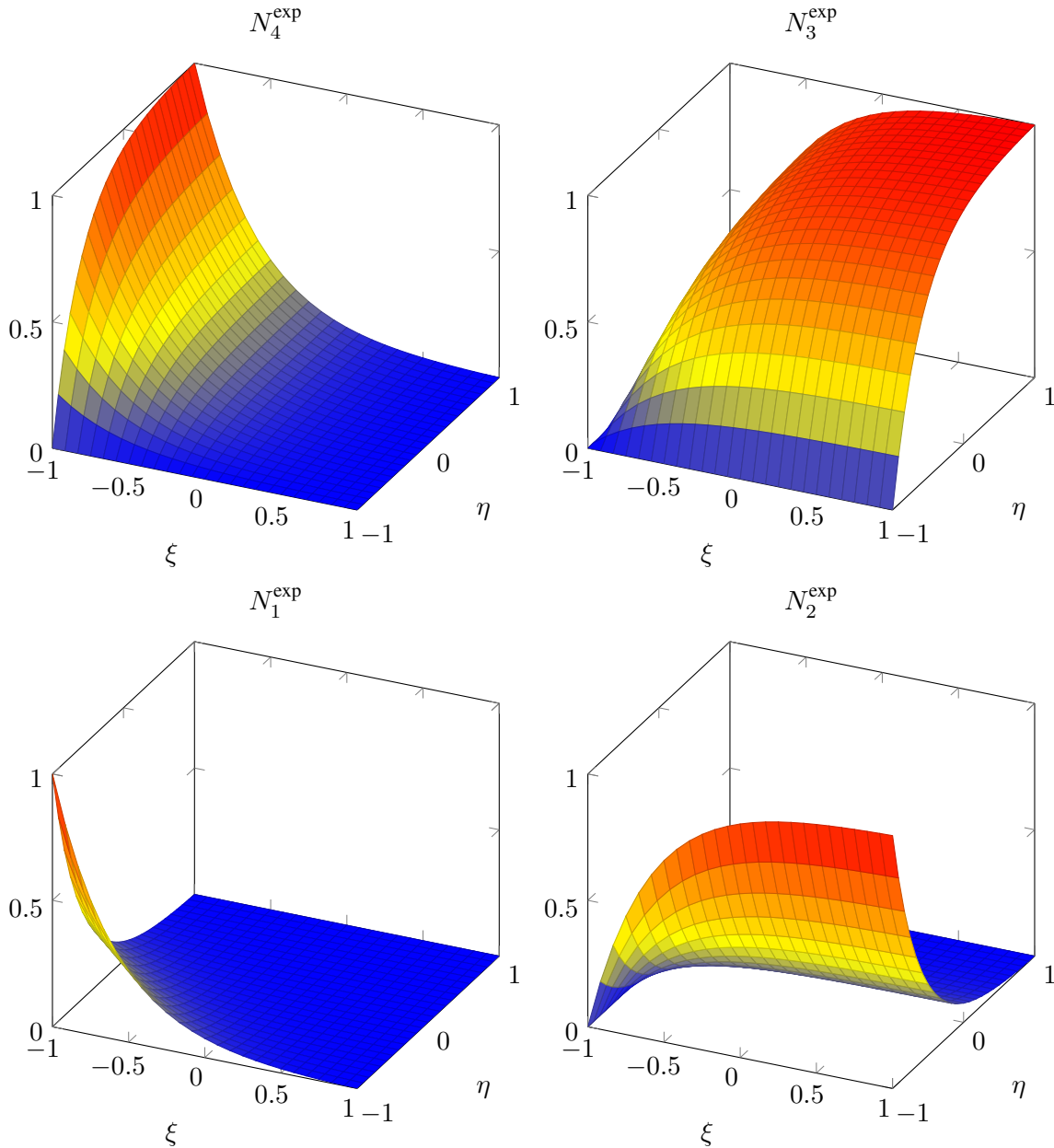


FIGURE 5.8: 2d exponential shape functions in natural coordinates

Besides the shape functions themselves, also their derivatives are required to approximate the gradient of the fracture field. Due to the identical linear approximation of the domain of the linear and exponential elements, the Jacobi matrix in both cases is the same,

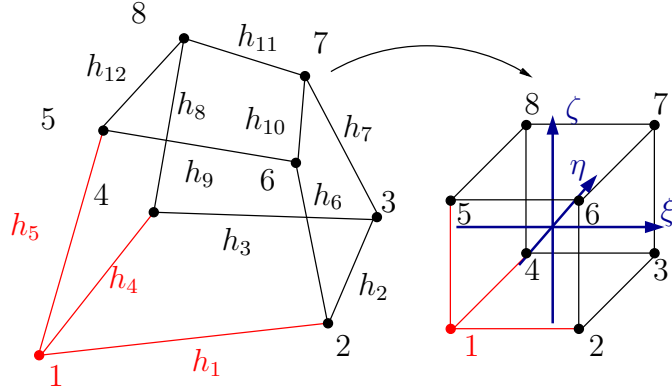


FIGURE 5.9: Node/edge numbering of 3d element in global (left) and natural coordinates (right).

$$\frac{\partial N_i^{\text{exp}}}{\partial \xi} = \frac{\partial N_i^{\text{exp}}}{\partial x} \frac{\partial x}{\partial \xi} + \frac{\partial N_i^{\text{exp}}}{\partial y} \frac{\partial y}{\partial \xi}, \quad (5.39)$$

$$\frac{\partial N_i^{\text{exp}}}{\partial \eta} = \frac{\partial N_i^{\text{exp}}}{\partial x} \frac{\partial x}{\partial \eta} + \frac{\partial N_i^{\text{exp}}}{\partial y} \frac{\partial y}{\partial \eta}. \quad (5.40)$$

### 5.4.3 Extension to 3d

The extension of 1d exponential shape functions to a 2d setting is presented in [42]. A similar approach for the 3d implementation is straightforward. Therefore the 1d exponential shape functions, belonging to adjacent edges of a respective node, are multiplied. This yields

$$\begin{aligned} \overline{N}_1^{\text{exp}}(\xi, \eta, \zeta, \delta_k) &= N_1^{\text{exp}}(\xi, \delta_1) \cdot \overline{N}_1^{\text{exp}}(\eta, \delta_4) \cdot N_1^{\text{exp}}(\zeta, \delta_5), \\ \overline{N}_2^{\text{exp}}(\xi, \eta, \zeta, \delta_k) &= N_2^{\text{exp}}(\xi, \delta_1) \cdot N_1^{\text{exp}}(\eta, \delta_2) \cdot N_1^{\text{exp}}(\zeta, \delta_6), \\ \overline{N}_3^{\text{exp}}(\xi, \eta, \zeta, \delta_k) &= N_2^{\text{exp}}(\xi, \delta_3) \cdot N_2^{\text{exp}}(\eta, \delta_2) \cdot N_1^{\text{exp}}(\zeta, \delta_7), \\ \overline{N}_4^{\text{exp}}(\xi, \eta, \zeta, \delta_k) &= N_1^{\text{exp}}(\xi, \delta_3) \cdot N_2^{\text{exp}}(\eta, \delta_4) \cdot N_1^{\text{exp}}(\zeta, \delta_8), \\ \overline{N}_5^{\text{exp}}(\xi, \eta, \zeta, \delta_k) &= N_1^{\text{exp}}(\xi, \delta_9) \cdot N_1^{\text{exp}}(\eta, \delta_{12}) \cdot N_2^{\text{exp}}(\zeta, \delta_5), \\ \overline{N}_6^{\text{exp}}(\xi, \eta, \zeta, \delta_k) &= N_2^{\text{exp}}(\xi, \delta_9) \cdot N_1^{\text{exp}}(\eta, \delta_{10}) \cdot N_2^{\text{exp}}(\zeta, \delta_6), \\ \overline{N}_7^{\text{exp}}(\xi, \eta, \zeta, \delta_k) &= N_2^{\text{exp}}(\xi, \delta_{11}) \cdot N_2^{\text{exp}}(\eta, \delta_{10}) \cdot N_2^{\text{exp}}(\zeta, \delta_7), \\ \overline{N}_8^{\text{exp}}(\xi, \eta, \zeta, \delta_k) &= N_1^{\text{exp}}(\xi, \delta_{11}) \cdot N_2^{\text{exp}}(\eta, \delta_{12}) \cdot N_2^{\text{exp}}(\zeta, \delta_8), \end{aligned} \quad (5.41)$$

where the element nodes and edges are numbered according to the sketch of the element in the natural coordinates  $(\xi, \eta, \zeta)$  in Fig. 5.9. The red-coloured node in the figure possesses the accordingly colored equation.

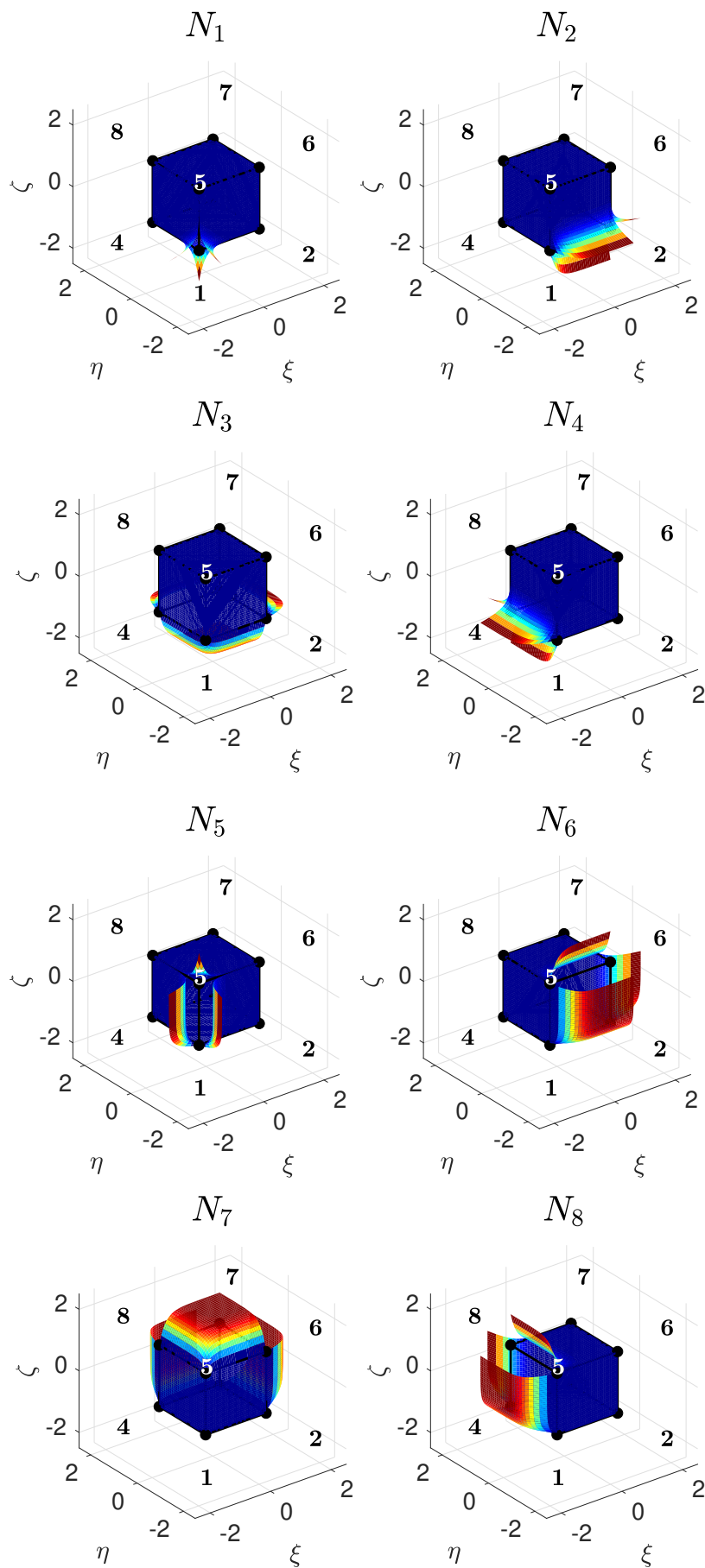


FIGURE 5.10: Shape functions of a 3d exponential element (orientation in local axis direction) with  $\delta_k = 20$ .

Each shape function depends on the ratio  $\delta_k = h_k/l_c$  of all three adjacent element edges and possesses the Kronecker delta property, i.e.  $N_I^{\text{exp}}(\xi, \eta, \zeta, \delta_k) = \delta_{IJ}$ . The partition of unity is ensured by adjusting the shape functions by the correction term

$$R(\xi, \eta, \zeta, \delta_k) = \left( \sum_{i=1}^8 \bar{N}_i^{\text{exp}}(\xi, \eta, \zeta, \delta_k) \right) - 1 \quad (5.42)$$

as for the 2d case. This term is then equally distributed to all shape functions

$$N_i^{\text{exp}}(\xi, \eta, \zeta, \delta_k) = \bar{N}_i^{\text{exp}}(\xi, \eta, \zeta, \delta_k) - \frac{1}{8}R(\xi, \eta, \zeta, \delta_k). \quad (5.43)$$

The form of the 3d exponential shape functions resembles the 2d shape functions on each side of the volume element, see Fig 5.10. The orientation issue of the 3d exponential shape function is more complex compared to 2d element, because of the 8 additional edges. In the scope of this work, the orientation issue of 3d shape functions will not be addressed further, such that all parallel edges in the same natural coordinate direction share the same orientation.

#### 5.4.4 Numerical Test

Due to the fact that only the global orientation of the exponential shape functions can be chosen, only in-plane cracks are possible. In the first test, no mechanical loads are applied. The initial phase field contains a crack with length  $L$ . The considered volume  $[-L, L] \times [-L, L] \times [-L/20, L/20]$  is discretized with a regular mesh of linear hexahedron elements, see Fig. 5.11. The orientation of the elements is only changed in the domain of the negative phase field gradient. The vertical orientation is switched. The plots in Fig. 5.11 show the

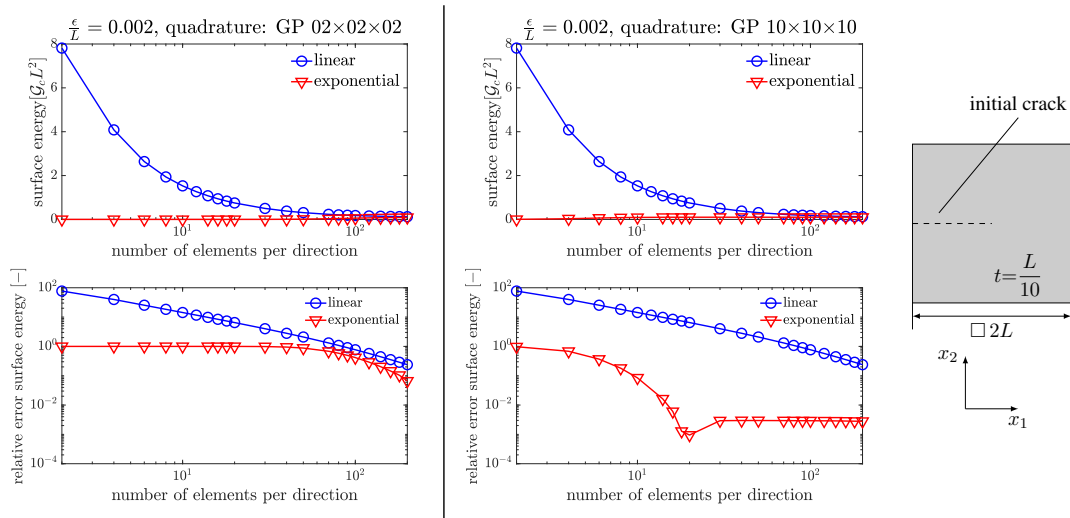


FIGURE 5.11: Surface energy of a stationary crack approximate by 3d linear and exponential shape functions (left). 3d crack in the  $xy$ -plane (right).

surface energy and its relative error of the linear and exponential approximation of the stationary crack for different numbers of elements. The graphs on the left side with  $2 \times 2$  Gauß points indicate the superiority of the exponential shape functions in the approximation of the surface energy, even with a too-low number of quadrature points. The performance of the 3d exponential shape functions is tested in a half-space model of fracture mode I, see Fig. 5.12. The fracture field contains a crack in the symmetry plane. The discretization consists of 1

element in the depth direction, 150 elements in the horizontal direction and a varying number of  $n$  elements in a direction orthogonal to the initial crack.  $5 \times 5$  Gauß points are used in the numerical integration. As in the 2d peel-off test, the presumed crack path along the bottom plane of the model, an additional layer of smaller elements is introduced, see [42].

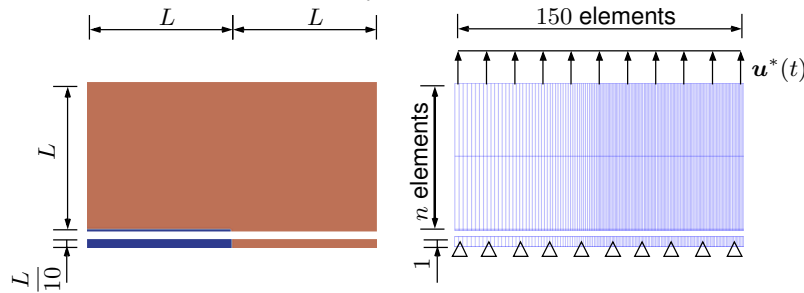


FIGURE 5.12: Comparison of the surface energy for linear (blue) and quadratic approximation of a stationary crack.

While the exponential shape functions underestimate the elastic energy, see Fig. 5.13, neces-

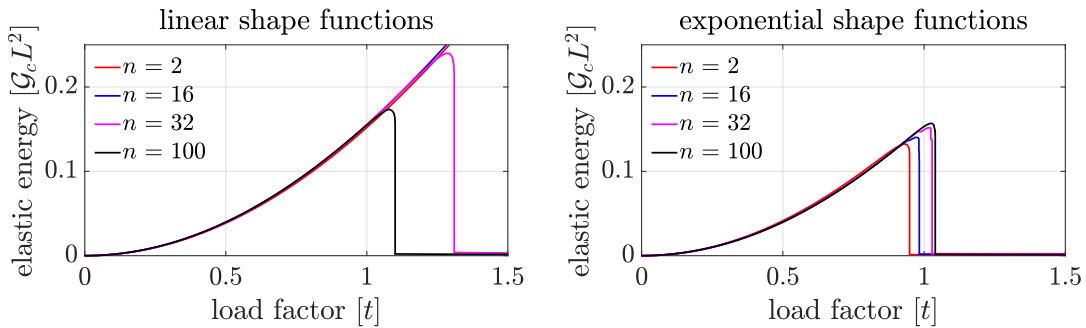


FIGURE 5.13: Elastic energy obtained with linear/exponential shape functions (left/right) for a 3d element.

sary for the cracking, the solution with linear shape functions overestimates the energy. This is due to the reduced integration of the exponential phase field. The crack surface has a very steep gradient in a coarse mesh, which requires a higher number of integration points, for a sufficiently accurate numerical integration. So with increasing integration points the error of surface energy tends towards zero. In comparison, the scaling of the elements or integration points show similar behaviour in that regard. Both increase the accuracy of the surface energy at the transition zone by either reducing the steepness of the exponential shape functions or improving the numerical integration of the steep shape function.



## Chapter 6

# Adaptive Numerical Integration

In the previous chapter, the FE method for linear and exponential spatial approximation was discussed, but the influence of the numerical integration was noticed without further detailed discussion. In general, numerical integration by a Gauß-Legendre quadrature is a standard procedure in FE, which doesn't require excessive explanation. However, in the case of the exponential elements, a detailed analysis is gaining importance. The following chapter is based on the work [59].

### 6.1 Numerical Integration

As mentioned before, the model is discretised by four-node quadrilateral elements, see Fig. 5.1 and 6.1. For a calculation in the natural coordinate system  $\xi - \eta$ , it is necessary to compute the determinant of the Jacobian matrix  $\underline{J}$  according to Eq. 5.33, which converts the local system  $x - y$  to the natural element coordinate system. Since linear shape functions are used for the approximation of the geometry in either case  $\underline{x}_h = \sum N_I^{\text{lin}} \underline{x}_I$ , the Jacobi matrix does not depend on the choice of the approximation of the  $s$ -field.

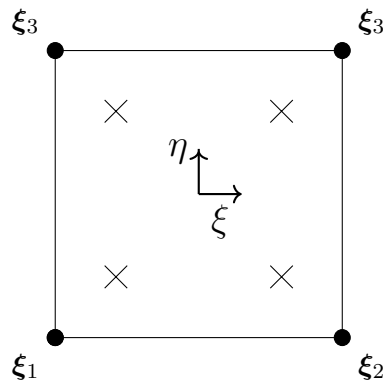


FIGURE 6.1: 2D isoparametric element.

The general equation for the numerical integration of a 2D integral in the parent space can be described by

$$\int_{\Omega_e} f(x, y) dx dy = \int_{\square} f(\xi, \eta) \det(\underline{J}^{-1}) d\xi d\eta \approx \sum_{p=1}^{n_{\text{GP}}} f(\xi_p, \eta_p) \det(\underline{J}_p^{-1}) w_p. \quad (6.1)$$

The square ( $\square$ ) stands for the natural configuration. The function  $f$  represents any arbitrary functions of the coordinates  $\xi, \eta$ . Thus the integral is approximated by a sum and  $f$  needs

only to be evaluated at the quadrature points. These function values are multiplied by their weight  $w_p$  and then summed up over all Gauß points  $n_{GP}$ . As mentioned before, the transformation of the integration in different coordinate systems requires the Jacobian matrix and in particular the inverse matrix  $\underline{J}_p^{-1}$ . The quality of the numerical integration depends on the curvature of the function and the spatial position and number of the quadrature points. In the case of higher-order shape functions, the deviation of the approximation through a quadrature can become noticeable up to unsustainable. This can be prevented by a sufficient number of quadrature points as well as a more suitable quadrature scheme.

### 6.1.1 Numerical Integration with Gauß-Legendre Formulas

In the standard finite element method, the numerical integration is performed by the Gauß-Legendre method, because of its accuracy for polynomial shape functions, see e.g. [79]. In the case of rectangular Lagrange elements with a 1:1 ratio of nodes to Gauß points (6.1) it is even exact. The quadrature of exponential shape functions always results in an error compared, to the exact value where the relative error is dependent on the present  $\nabla s$ . Exponential functions can be expressed as an infinite Taylor series

$$e^x = \sum_{n=0}^{\infty} \frac{x^n}{n!} = 1 + x + \frac{x^2}{2!} + \frac{x^3}{3!} + \frac{x^4}{4!} + \dots \quad (6.2)$$

and would require an infinite number of Gauß points for an analytically exact integration, because of the infinite number of polynomials.

An obvious approach to meet a sufficient accuracy for the quadrature of exponential elements is the increase of Gauß points. Before that, a marking strategy is useful to select the elements that require a modification of the quadrature. Those elements would possess e.g. a threshold gradient of the phase field. In unmarked elements, the amount of Gauß points solely depends on the sufficient approximation of the displacement field and is fixed to the mentioned ratio of 1 : 1.

TABLE 6.1: parameter for the fracture mode I.

model parameter	value
1st Lamé constant $\lambda$	$2.2 \cdot 10^6$
2nd Lamé constant $\mu$	$2.2 \cdot 10^6$
regularization width $l_c$	$1.0 \cdot 10^{-3}$
stabilizing parameter $\eta$	$1.0 \cdot 10^{-5}$
crack resistance $\mathcal{G}_c$	1.0
mobility factor $M$	$1.0 \cdot 10^9$

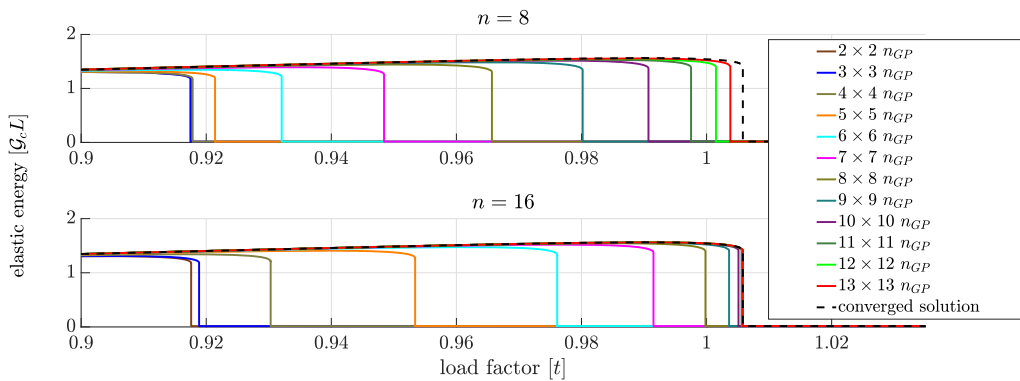


FIGURE 6.2: Elastic energy for crack growth test with different element sizes and Gauß points.

In the next step, the number of Gauß points has to be determined for the marked elements. This requires e.g. a dependency of the precision of the quadrature and parameter. A key parameter of the approximation of the phase field with exponential shape is the parameter  $\delta$ . It defines the maximal possible phase field gradient within the element, due to the formulation of the exponential shape functions. The value of  $\delta$  is calculated from the ratio of the element edge length  $h_i$  and the regularization width  $l_c$ . By computing the number of quadrature points as a function of  $\delta$ , the accuracy of numerical integration would increase by increasing mesh size  $h$  and decreasing crack width  $l_c$ .

For this consideration, we analyze a simple fracture mode I. The 2D model is a square domain with an initial crack with the half length of the probe and positioned in the middle, see Fig. 6.4. To reduce the computational time, the model will be halved along its symmetry, which also halved the initial crack. The model parameters are displayed in table 6.1. The considered quantity for this case is the elastic energy during the crack propagation. For the simulation, different discretization normal to the crack surface with 8 or 16 elements are computed. The number of elements along the crack path stays equal for both cases. Further, the number of Gauß points will be increased from the standard  $2 \times 2$  to  $13 \times 13$ . The results show that while the crack width is equal for both cases the element size normal to the crack surface differs by factor 2 which leads to different elastic energy with an equal number of Gauß points, see Fig. 6.2. Because of this difference, the required number of quadrature points for the same precision varies. This relation will be used for an adaptive scheme for the number of Gauß points.

### 6.1.2 Adaptive Quadrature

Although exponential elements reduce the required mesh density for the approximation of sharp cracks, they require a more precise quadrature. To benefit from the applied advanced discretization technique, an adaptive quadrature shall be implemented. This necessitates an alternation of the quadrature, which can be obtained in different ways. Firstly, the use of a different scheme, secondly, an increase of Gauß points and thirdly, a remeshing. The last approach would defeat the purpose of the exponential shape functions, therefore we will focus on an adaptive choice of Gauß points and a different quadrature scheme.

#### Localization for Adaptivity

Before an adaptive routine is discussed a reasonable precondition should be implemented. While the whole body has a nearly constant intact phase field the regions of high gradients are rather small. Therefore, the adaptivity of the number of Gauß points can be locally constrained to avoid a waste of computational time for a more precise integration, see Fig. 6.7. This is achieved by the condition

$$\prod_{I=1}^N s_I < 0.5 \quad (6.3)$$

which initiate the choice for an adapted number of Gauß points in case the product of the nodal fracture field values within an element is less than 0.5. This condition will be checked in every iteration. So, while the default quadrature rule is  $2 \times 2$  Gauß-Legendre scheme, a different number of Gauß points  $n_{GP}$ -function chosen as a function of  $\delta$  for elements fullfilling (6.3).

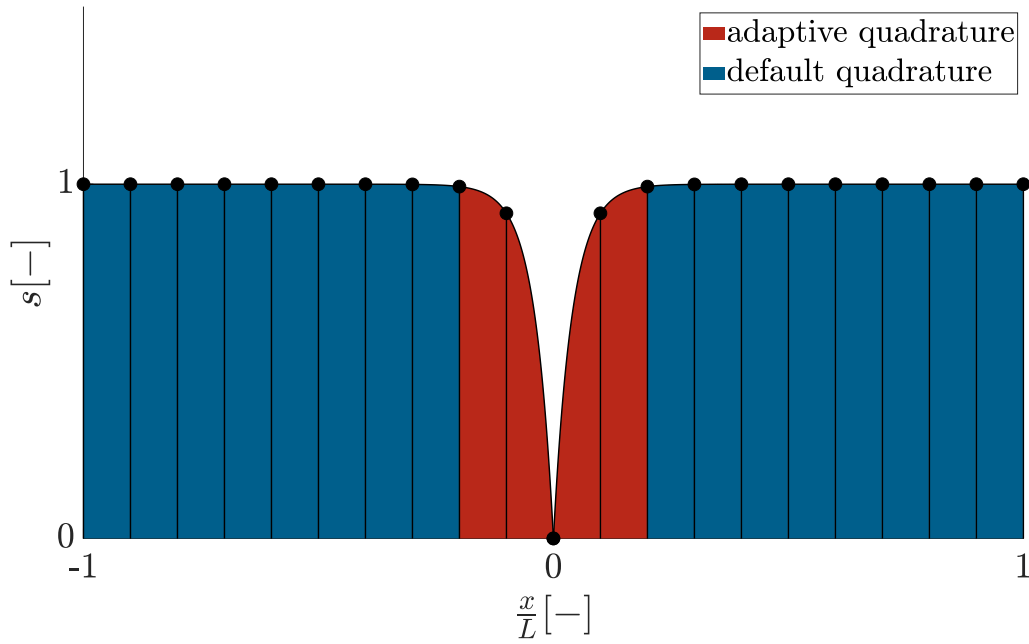


FIGURE 6.3: Local adaptation of quadrature.

### Order Adaptivity of the Numerical Integration

Elements which fulfil the requirement for an adapted quadrature should be checked on their demand for more precise numerical integration. A scalable straightforward approach is the increase of quadrature points. A reasonable value for the determination of the amount of  $n_{GP}$  is the mentioned parameter  $\delta$ . This relation can be expressed by a function

$$n_{GP} = f(\delta_{\max}). \quad (6.4)$$

The parameter  $\delta$  contains the element edge lengths. Depending on the element shape, this can lead to four different values in a quadrilateral element. The following routine chooses the number of quadrature points for all dimensions to be equal. Thus, only one  $\delta$  can be used within the element. Therefore, the largest  $\delta$ ,  $\delta_{\max}$ , is chosen as a parameter for  $f$ , because it permits the highest gradient across the element.

Like in [42], the 2D exponential shape functions have been evaluated in two different test cases for a straight stationary crack.

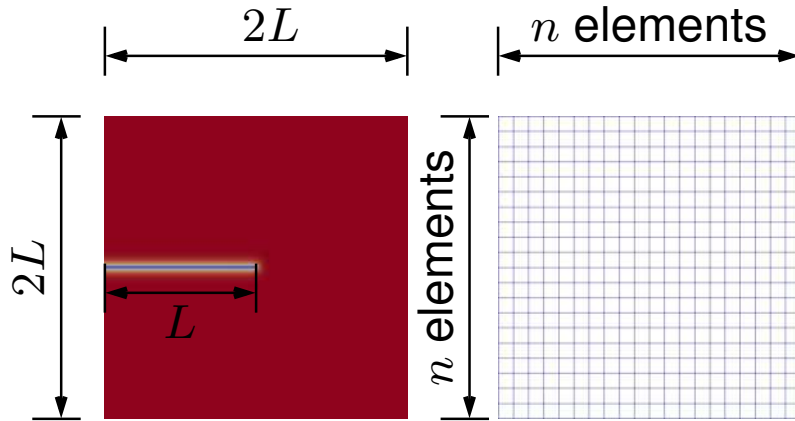


FIGURE 6.4: Test case: stationary crack (fracture field left, mesh right).

The setup for the first stationary test is depicted in Fig. 6.4. The domain is discretized homogeneously with  $n \times n$  elements and contains a horizontal crack of length  $L$ . No mechanical loading is considered.

For the second test case, the mechanical loading is considered and use is made of the symmetry of the problem. The applied load is a displacement constant along the edge parallel to the initial crack, which increases linearly with time. The mesh will be, in contrast to the stationary case, only refined in the direction perpendicular to the crack surface. In the direction of the crack, the edge length of the elements remains constant, like in [42].

The construction of a  $n_{\text{GP}}$ -function requires data points. For this, the case with the stationary crack is utilized in a parameter study. Hereby, the parameters nondimensionalized regularization length  $\bar{l}_c$  and element edge length  $\bar{h}$  as well as the number of Gauß points per spatial direction  $n_{\text{GP}}$  are varied to generate the surface plots in Fig. 6.5. They display the relative error of the surface energy, which is calculated as

$$e = \underbrace{\int \psi^s dV}_{\text{numerical approx.}} - \underbrace{2 l_c L \mathcal{G}_c}_{\text{analytical approx.}} \quad (6.5)$$

From the different subfigures of figure 6.5, it is possible to identify the dependency of the accuracy on the number of Gauß points  $n_{\text{GP}}$ . An optimum function  $f(\delta)$  can be defined, which limits the maximal error for a certain  $\delta$  range.

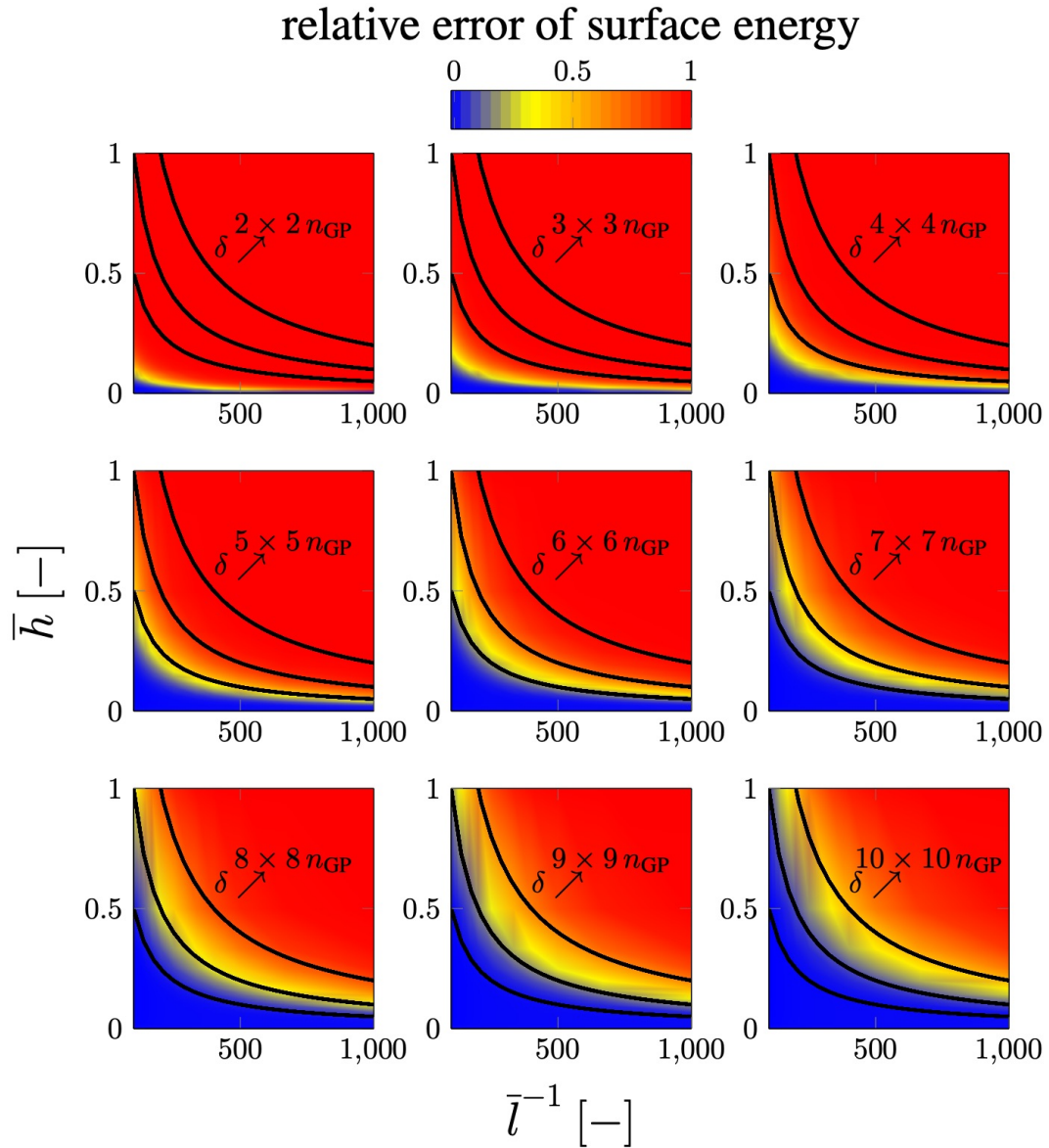


FIGURE 6.5: Parameter analysis for a stationary crack over different element sizes and regularized length.

The values  $\bar{h}$  and  $\bar{l}_c$  are considered by the parameter  $\delta = \frac{\bar{h}}{\bar{l}_c}$ . The generated graphs are then approximated by a linear regression for an error range of 2 – 10 %, see Fig. 6.6a. It is our goal to derive a function  $f(\delta)$  that guarantees an error smaller than 5%.

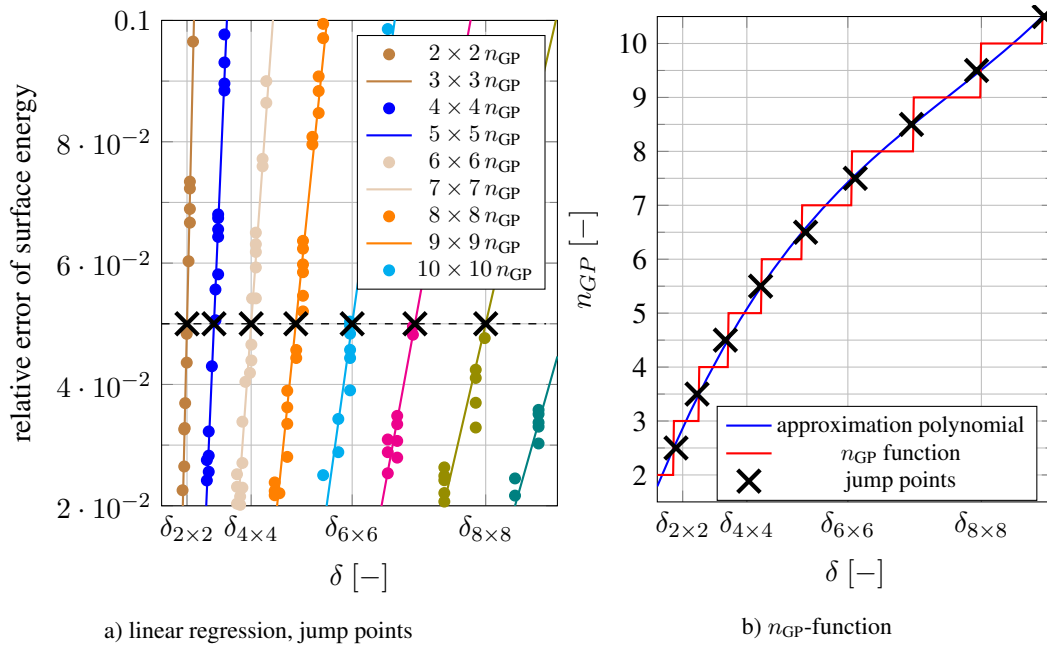


FIGURE 6.6: Formulation of the choice of the number of Gauß points.

The function is interpolated by points of the intersections of a horizontal line, which represent an arbitrary error of 5 %, and the error curves of the different Gauß point numbers. They are the jump points  $\times$  at which a higher number of Gauß points should be chosen. In the next step, the points are used for the interpolated polynomial, see Fig. 6.6b. The functional values are then rounded to provide integer values for  $n_{GP}$ -function, see Fig. 6.6b.

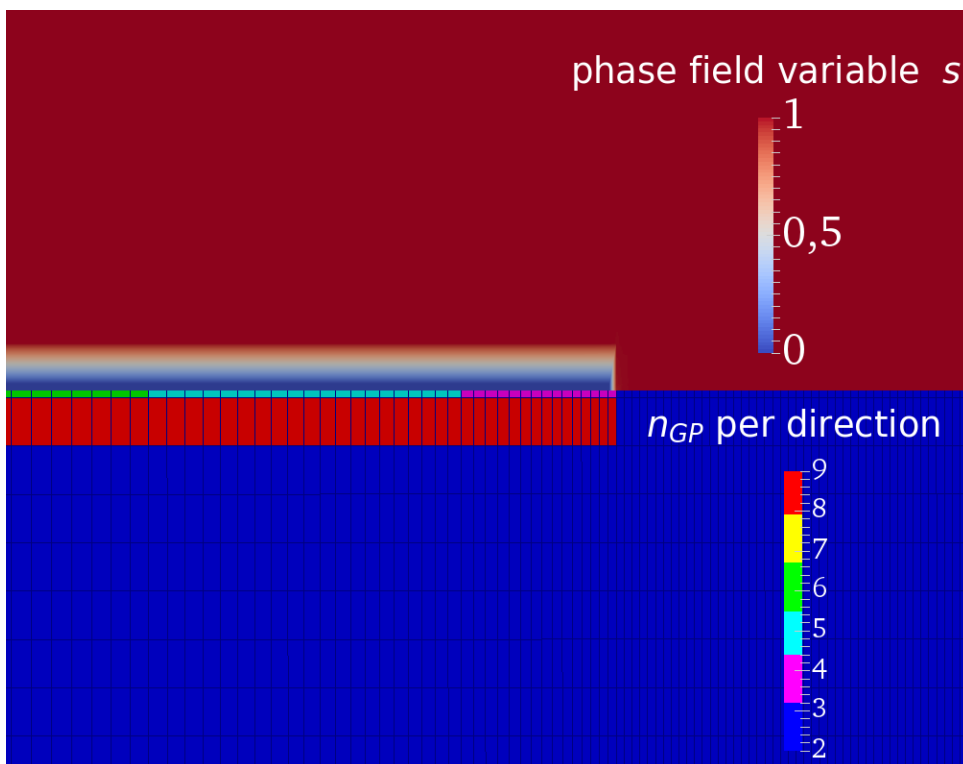


FIGURE 6.7: Local adaptation of the number of quadrature points.

The combination of the condition for adaptivity and an adaptive number of Gauß points generates the local Gauß point adaptivity routine. A representation of the adaptive routine is depicted in figure 6.7. The figure shows a stationary adaptive adjustment of the number of Gauß points  $n_{GP}$  for an initial phase field  $s$ . Most of the elements have  $2 \times 2$  quadrature points, because of the large intact area of the domain. Higher  $n_{GP}$  can be seen at the crack surface as expected. Because of a decreasing mesh size towards the crack tip, the number of Gauß point show the same trend. The elements in the second row at the crack surface are coarser and therefore are integrated by  $9 \times 9$  GP. In practical terms, if an element satisfies Eq. (6.3), the number of Gauß points are altered depending on its greatest  $\delta$ .

### Double Exponential Formula

An improvement of the numerical integration can also be achieved by the usage of a more suitable quadrature scheme. The special shape function inherits characteristics of exponential functions like the infinite number of derivatives. Functions with this property can be more accurately integrated by the Double Exponential (DE) formula, see [71]. It consists of an infinite series of integration points and tends to distribute the major proportion of its quadrature points toward the integration limits, see Fig. 6.8. Due to the infinite series, a truncation is necessary for the application. However, a consequence of this is an occurring residual of the total sum of the weights e.g. Fig. 6.8 (=1.9998). This deviation leads to an error, because of the lower deployed domain size, which is in this case 2 from -1 to 1. This problem can be corrected by normalization. Although the DE formula is on average less precise than the quadrature scheme based on the Gauß rule, it is more accurate for certain types of functions. For instance, the accuracy of the quadrature of functions that possess singularities or infinite derivatives like in our case benefit from the DE formula, see [71]. The equations for the general formula, position and weights of the quadrature points are

$$I = \int_{-1}^1 f(\xi) d\xi = \sum_{-\infty}^{+\infty} w_k f(\xi_k), \quad (6.6)$$

$$\xi_k = \tanh\left(\frac{1}{2}\pi \sinh(kh)\right) \quad \text{and} \quad (6.7)$$

$$w_k = \frac{\frac{1}{2}h\pi \cosh(kh)}{\cosh^2\left(\frac{1}{2}\pi \sinh(kh)\right)}. \quad (6.8)$$

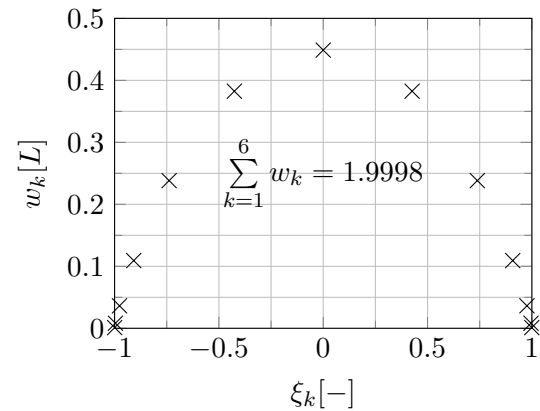


FIGURE 6.8: DE formula: for a 1D-reference domain quadrature point positions and weights

Because of the necessary point in the middle of the domain and the symmetry of the GP positions, the amount of quadrature points is always odd.

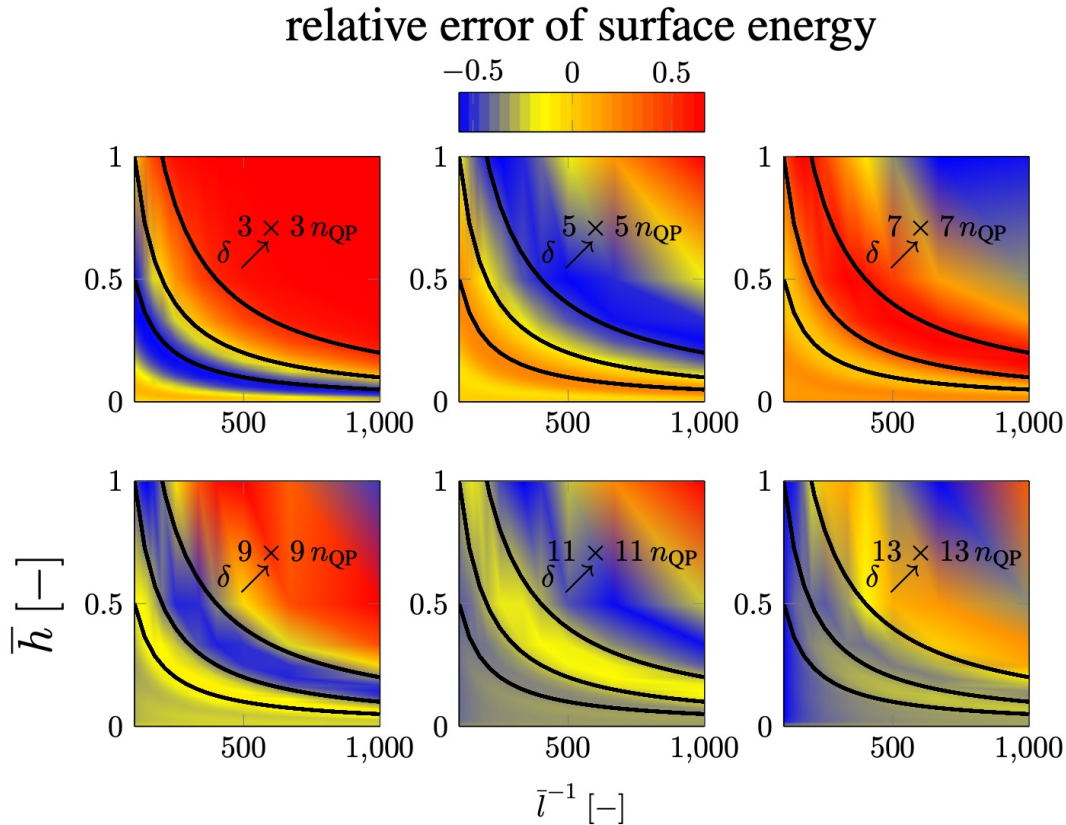


FIGURE 6.9: Parameter analysis for a stationary crack over different element sizes and regularization length.

Similar to the Gauß-Legendre method, the DE formula is also used in a parameter study to observe the correlation of the surface energy with the elements size  $h$  and crack width  $l_c$ . The results are displayed in Fig. 6.9. Unfortunately, different non-monotonous behaviour of the error of the surface energy can be identified. This could originate from the exponential quadrature rule, which is based on trigonometric functions. Therefore, it is necessary to apply at least  $13 \times 13$  quadrature points to achieve an error with a robust precision below 5%, because the error strongly differs for quadrature points under 13 points. The comparison in terms of accuracy shows an advantage of the DE formula but is only beneficial for cases in which the Gauß integration with  $12 \times 12$  doesn't obtain the minimum requirements.

### 6.1.3 Numerical Results

The performance of the numerical integration is tested in a 2D simulation of a fracture mode I, which is introduced as the second test case in section 6.1.2 and replicated from [42]. Thereby the behaviour of the elastic energy  $E^e = \int \psi^e d\Omega$  during the crack propagation is observed. To study convergence, the number of elements normal to the crack surface is varied from two to 100 elements. The important quantities are the load factor and maximal elastic energy at which failure of the specimen occurs. In Fig. 6.10 an overall comparison of the different quadrature concepts is displayed. Also included are the results for standard linear elements. The different variants can be divided by quadrature method and adaptive(adap)/non-adaptive. Furthermore, there are differences between the number of quadrature points of the numerical integration methods. The DE formula uses always 13 points per direction and in the adaptive form switches for elements with low phase field gradient to a Gauß-Legendre integration

with  $2 \times 2$  GP. Furthermore, the  $n_{\text{GP}}$  for the adaptive Gauß quadrature is limited to 10 and starts with the standard 2 per direction.

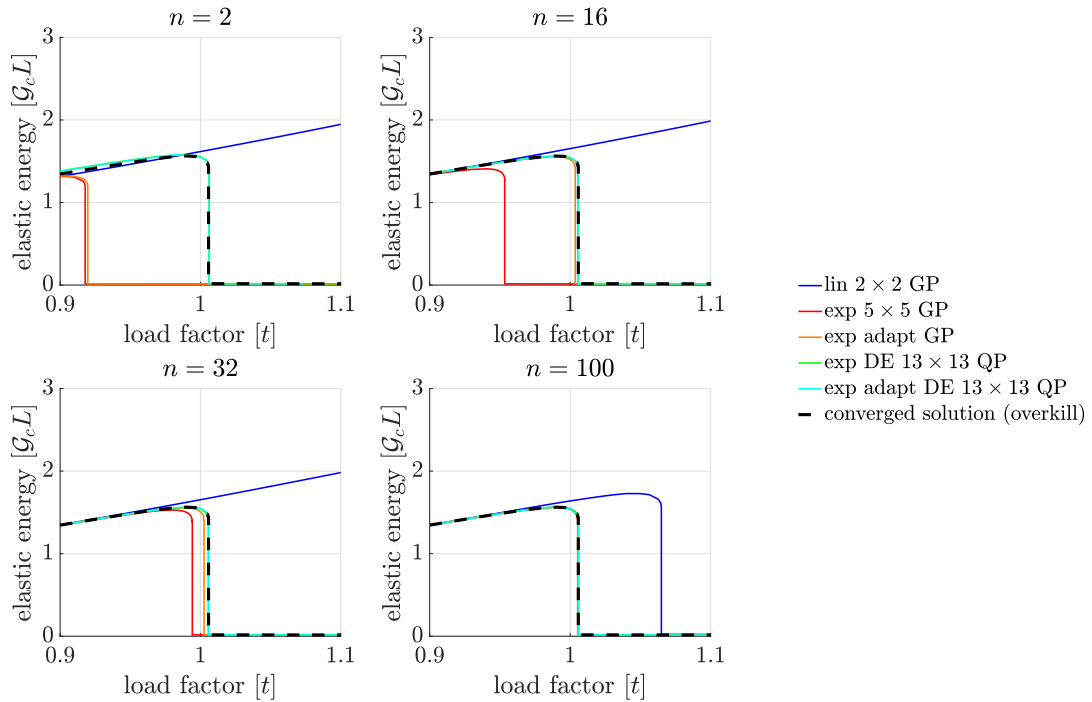


FIGURE 6.10: Elastic energy during a fracture mode I for different implementation.

In this setting the solution of the elements integrated with the DE formula already converges for an extremely coarse mesh. In the case of a static  $5 \times 5$  Gauß points approach the convergence is only obtained for at least 32 elements towards the fracture plane. The improvement by an adaptive number of Gauß points reduces the required mesh density by 50%. The disparity between the integration methods can be partially explained by the lower amount of quadrature points for the adaptive routines, but even with the same number the DE formula is more efficient, see table 6.2.

TABLE 6.2: number of quadrature points of all elements for the different solutions of Fig. 6.10.

	lin $2 \times 2$ GP	exp $5 \times 5$ GP	exp adapt GP	exp DE $13 \times 13$ QP	exp adapt DE $13 \times 13$ QP	
n	2	900	2250	2450	5850	4800
	16	5100	12750	6536	33150	9247
	32	9900	24750	10924	64350	13995
	100	30300	75750	32480	196950	36358

The total number of quadrature points of the models are reported in table 6.2. For the adaptive cases, the numbers of the last load step are considered, because it shows the highest number of quadrature points during the simulation. The focus of the analysis lies on the adaptive solutions. While the adaptive integration with the Gauß-Legendre method uses fewer points, it is also less accurate. When it is used for fine meshes or wide cracks it becomes more

efficient due to the necessary high amount of quadrature points of the DE formula, which is visible in the table 6.2 for  $n = 100$ .

## 6.2 Summary and Outlook

While the numerical integration of the Lagrange elements can be analytically optimal under perfect conditions, the same accuracy can not be achieved for exponential elements. To approximate any phase field transition zone, the exponential term of the shape functions is adjusted by the length parameter  $l_c$ . This ability of the exponential elements to compute any crack independent of the steepness of the phase field or element shape enables the approximation of cracks with a static and coarse mesh. Unfortunately, the more precise numerical integration scheme increases the computational effort.

The adaptive strategy is based on a simple step function, which connects the value  $\delta$ , the ratio of element sizes and regularization width, and the number of quadrature points  $n_{GP}$ . The functions are constructed by an error analysis of the surface energy depending on  $\delta$  and  $n_{GP}$  of a stationary crack. In a similar test to the Kuhn and Müller [42], the adaptive strategy could show a further improvement of the exponential strategy by adapting the numerical integration near the crack surface and therefore reducing computation time and increasing accuracy. Furthermore, two different numerical integration schemes have been tested. The standard approach for the finite element method is in the form of the Gauß-Legendre integration and the DE formulation. Unfortunately, the DE formula requires a higher minimum number of quadrature points for comparable results, because of its formulations as an infinite series and its subsequent requirement of a sufficient number of quadrature points. This flaw makes a computation with the DE formula only computationally efficient for very steep transition zones.

In the preceding paragraph, the goal of increased accuracy of the numerical integration is achieved by an adaptive approach based on a variable choice of the number of Gauß points per element, which is defined through a prior error evaluation. A more suitable numerical integration scheme based on an exponential formulation didn't result in a reduced number of quadrature points. The quantities, which determine the necessity for an increased number of quadrature points depend on the phase field and the crack width. While the phase field values only activate the adaptive numerical integration, the crack width defines the number of quadrature points. This is due to the fact, that the phase field is not reliable as an indicator for the required quadrature points, because for exponential elements approximation of a crack surface is achieved within one element. The parameter  $\delta$ , which contains the element size and the regularization width is a robust quantity for the choice of quadrature points because it is mesh size independent. The maximum number of quadrature points available to the adaptive algorithm is defined arbitrarily. This limitation is not only computationally reasonable but also from the perspective of the phase field approach. Because in order to describe a crack path sufficiently the mesh density has to be small enough. This limits the number of required quadrature points for an appropriate accuracy.



## Chapter 7

# Adaptive Shape Functions

In order to apply exponential shape functions in a fracture phase field model, knowledge of a suitable orientation of the exponential shape is required because its dependency on the crack path or more specifically on the crack field gradient. In general, FEM simulations are performed with static spatial discretization, which means in case of exponential shape functions a fixed orientation from the initial state. For an accurate simulation of fracture scenarios a prior knowledge of the crack path is necessary and only possible for simple cases, e.g. a tension load case with correctly aligned elements and the directions of the crack growth. In more complex cases, the crack path becomes not predictable in its exact phase field representation. This limitation deprives the phase field model of its full potential to compute complex crack patterns with exponential shape functions. The only solution to this dilemma is an adaptive algorithm with the possibility to reorient each exponential shape function appropriately in an efficient manner to make them applicable without losing the flexibility of the fracture phase field model. In order to obtain this goal, the algorithm converts the shape functions from static to adaptive and makes them depend on the field that they approximate. Even if the function of the algorithm for the adaptive shape function can be easily recapitulated, the possibilities of their implementation can vary tremendously. Diverse forms of them are presented in the publications [60], [58] and [44].

### 7.1 Basics of Adaptive FE

In a broader sense, the application of exponential shape functions can be viewed as a refinement technique whereby the spatial approximation of the fracture phase field is improved and by consideration of adaptive numerical integration, it is even scaled. In a mesh with an average element size  $h$  that is bigger than the crack width value  $l_c$ , the fracture phase field in an element is either roughly constant or approximates a fixed gradient for the approximation of a crack surface. Exponential elements can approximate both within one element, while a linear element always requires multiple elements to describe a crack surface. As mentioned in the introduction to the exponential elements, the crack surface can have different orientations. So, in fact, the only necessity of adaptive strategy is caused by the asymmetry of the shape functions. In a broader perspective, the developed adaptive strategy can be seen as an adaptive FE method. To the author's knowledge, the procedure of adaptive exponential shape functions in the framework of the Finite Element method is quite new. For a better implementation, it is therefore advantageous to look at established techniques that have similar goal. Hereby, the adaptive approaches for spatial refinement that are most known are the  $h$ - and  $p$ -refinements. Additionally, the  $r$ -refinement is mentioned, see Fig. 7.1.

A more detailed description of these refinement techniques can be found in [79]. They share the same objective, the local improvement of accuracy by either increasing the number of elements ( $h$ ), the number of nodes ( $p$ ) or local rearrangement without increasing either of

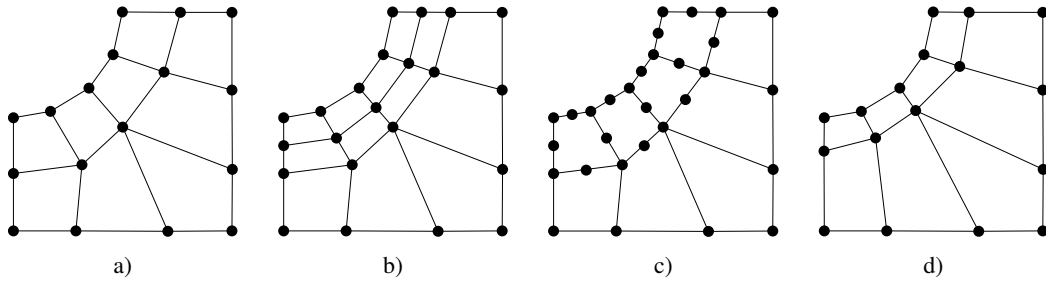


FIGURE 7.1: Original,  $h$ -refined,  $p$ -refined and  $r$ -refined mesh (from left to right).

them ( $r$ ). Even though  $r$ -refinement is mentioned in the research literature, it has low practical relevance and is only mentioned for completeness. One reason for its lack of relevance is the complexity of its application. In contrast to the  $r$ -technique, the  $h$ - and  $p$ -refinements are established techniques, due to their extensive practical use.

The  $p$ -refinement method can be described by the increase in the number of nodes per element, which raises the order of the shape functions of the element. The disadvantage of adding more nodes to the refined area is the enlargement of the system of equations. This increase in the problem size for the system matrix causes an inevitable decrease in efficiency.

The  $h$ -refinement or in a more practical sense, the element size reductions, can be achieved by element subdivision or remeshing. The remeshing process is quite similar for different element types, but the subdivision is not. For example, in the 2d case, two mainly used shapes are triangle or quadrilateral elements. While the subdivision of a triangular shape can be done without increasing nodes on surrounding elements, the quadrilateral elements produce additional nodes by splitting it into sub-elements, thus adding nodes for neighbouring elements. These additional nodes, which are not implemented in the neighbouring elements, are called hanging nodes, and they take more effort to handle, see [78]. In the context of the fracture phase field model, different attempts have been made for an  $h$ -refinement with a subdivision for triangular elements, see [47] [6], [16], [61] and [32], which showed an improvement in the approximation of fracture field models. For quadrilateral elements, a process is presented in [54]. Herein, the domain consists of two different meshes. At the crack, the mesh is finer, and a certain distance from the crack, it is coarser. Further, the areas with different mesh densities are not connected by shared nodes but by a Nitsche method. In this way, hanging nodes are avoided.

The technique most used is the  $hp$ -method, which is another solution to avoid hanging nodes. As the name suggests,  $hp$ -refinement is a combination of  $h$ - and  $p$ -refinement. The area of interest, that is refined for a better approximation increases the element count and subsequently the node count without hanging nodes. In order to avoid them, these nodes are added to the neighbouring elements by increasing their polynomial character, but only on the necessary borders of the element. This opens the possibility to refine quadrilateral elements by connecting  $h$ -refined elements with coarse elements by blending elements. It has already been implemented for fracture phase field models e.g. in [49], [56], and [35].

## 7.2 Concept

The goal of the following adaptive method is to improve the spatial approximation of a fracture field by making the exponential shape function orientation dependent of the crack field. Adaptive refinement techniques in form of  $h$ - or  $hp$ -refinement are generally suitable to improve the spatial approximation independent of the properties of the physical model, so they are also applicable for fracture phase field models to increase their accuracy. Unfortunately, these approaches cause an increased complexity in additional data handling because of a growth in number of elements and nodes. At worst, it can result in an unfavourable efficiency and an increase of the computation time. In phase field models, the area of focus for an accurate spatial approximation is the phase transition zone, or more specifically, for the considered model, the crack surfaces. For standard adaptive methods, this means an increase in the mesh density until the crack surface is approximated sufficiently. The fact that transition zones of phase fields have an approximately exponential shape [42] indicates that a finer discretization through a higher mesh density is counterintuitive and inefficient. Since the gradient to be resolved is already known. Furthermore, the required number of elements can grow rapidly with a decreasing regularization width, so a straight forward approach to circumvent an approximation of a mostly known gradient is the use of exponential functions or, in the case of the Finite Element framework, the application of shape functions, which already fulfil the required shape.

This conclusion led to the idea of exponential elements, which approximate the fracture phase field by exponential shape functions. Their asymmetry and therefore their inability to approximate symmetric cracks require an adaptive strategy. So, the presented approach is called adaptive shape functions. Before the novel adaptive approach is presented in detail, the model is compared with the standard refinement strategy. Thus, the phase field is not relevant and the same original mesh from Fig. 7.1 is compared with the depiction of the example of a refinement with exponential shape functions, see Fig. 7.2. The difference between the original mesh and the adaptive approximation is depicted by colours. Hereby, the shape functions of each edge are marked by their colour blue for linear (—lin) and red for an exponential shape functions (▶ exp). The area of interest is the quadrant of the circle or to be more precise, the spatial direction of the normal vertices to the circle, like for the standard refinement strategies. Therefore, the exponential functions are only used for that purpose. This adaptation of the approximation points out another obvious difference from the classical refinement schemes, it is the unit that is refined. In the adaptive shape function refinement, each edge is adapted separately, which guarantees continuity over the element boundaries.

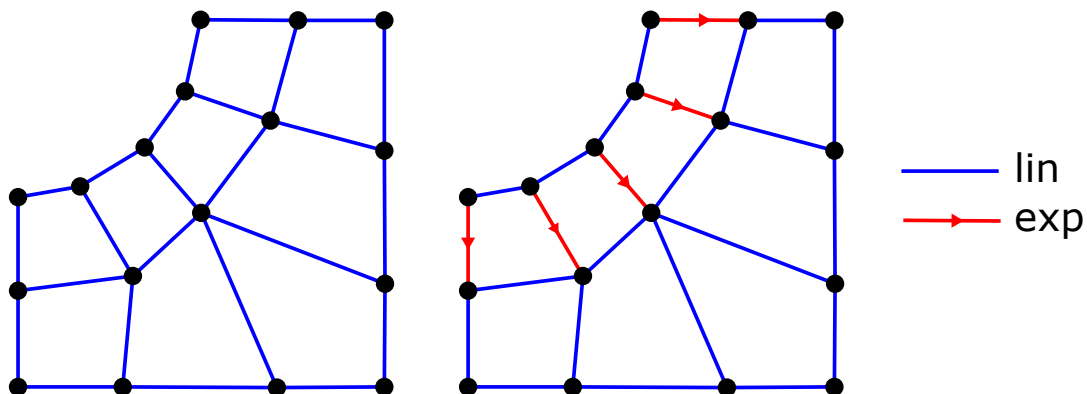


FIGURE 7.2: Example of the adaptive shape function.

An aspect skipped is the orientation of the exponential elements. In the depicted case, the orientation is flagged by the arrow in the middle of the red edges. For a good approximation quality, the exponential elements must be oriented accordingly with respect to the location of the cracks. In the presented example, the fracture field is deliberately ignored for a general description. The details are crucial for the presented algorithm, so in order to be accurate in the description in the next sections, the core features of the adaptive algorithm are explained in depth. Although the essential points of the algorithm depend on each other, they were described separately to give a more precise description. In the first step, the continuity of the shape functions of each edge is outlined, which is essential to fulfilling the properties of the Finite Element method. This property ensures the utilization of the blending elements. They combine linear and exponential shape functions for 2d quadrilateral elements. Furthermore, the exponential shape functions can be chosen in their orientation in order to approximate symmetric cracks. Before the algorithm is described, two practical points are analyzed to improve and circumvent issues that have to be considered in the adaptive algorithm. The core element of this work is the adaptive shape functions algorithm, whose main features are the marking strategy and the process solution level. The marking strategy describes the marking value, and the function defines the choice of shape function. This is computed in the subroutine for the whole simulation. The position in the simulation process is discussed in the section on process level, where the algorithm in the total framework of the FE solver is illustrated.

### 7.3 Continuity

The continuity of the properties of the field is derived by equal shape functions at the element boundaries, for the considerations of 2d cases, the geometric edges. For the case of the presented adaptive shape functions algorithm, two or respectively, three shape functions (linear, positive exponential and negative exponential) are available. So, the challenge is to ensure continuity of the shape functions across element boundaries, which only becomes an issue through the mirroring of exponential shape functions. In extended finite element methods, this issue also arises, see e.g. [18]. The distinctive example stems from the asymmetry of the exponential shape functions and their inability to approximate a symmetric crack. Therefore, the orientation has to be changed depending on the crack's position towards the element edge. This orientation, or shape function alteration, must be consistent across element boundaries, see Fig. 7.3. In most FEM programs, as is also in the present work, each element values are computed to form the relevant matrices without having access to data of neighbouring element and thus also no information of the shape functions of the neighbouring elements can be exchanged. In order to resolve this trivial issue, two data lists are implemented. For the first list, each edge is assigned a unique number and an indicator that describes their shape function (-1: mirrored exponential, 0: linear, 1: exponential). The second list contains, for each element, the edge numbers in form of a coincidence scheme. They are used in combination to always ensure that the shape functions on each element edge/boundary have the same properties and can further be used as a history variable for the shape functions of the last iteration step.

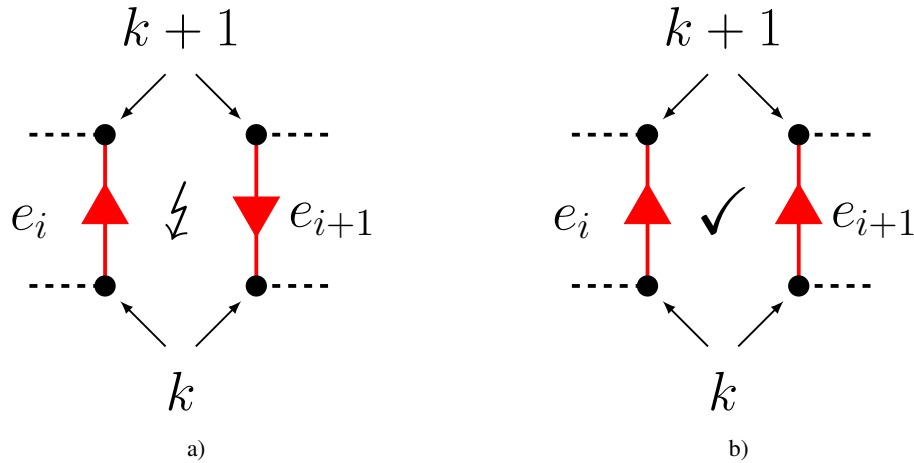


FIGURE 7.3: Incorrect a) and correct b) orientation of exponential shape function continuity problem.

## 7.4 Blending Elements

The application of the exponential shape function reduces the computational effort but only if they are applied in a precise way, so that the orientation of the exponential shape function and the gradient of the fracture field are in agreement with each other. Phase field models are dominated by areas with a constant phase field value. These areas don't provide a determination of the appropriate orientation for the exponential shape functions locally and can be approximately accurately by standard bi-linear elements as well. Furthermore, the usage of linear shape functions in constant phase field areas increase the efficiency, especially by avoiding a more extensive numerical quadrature. Another essential consideration is the stability of the algorithm, which would suffer heavily from the orientation of exponential shape functions in areas without a distinct phase field gradient and would rely on tracking cracks all over the domain. So, in order to decrease the orientation choice to a minimum, the discretization of nearly constant fracture field areas are achieved by the approximation with symmetric bi-linear shape functions.

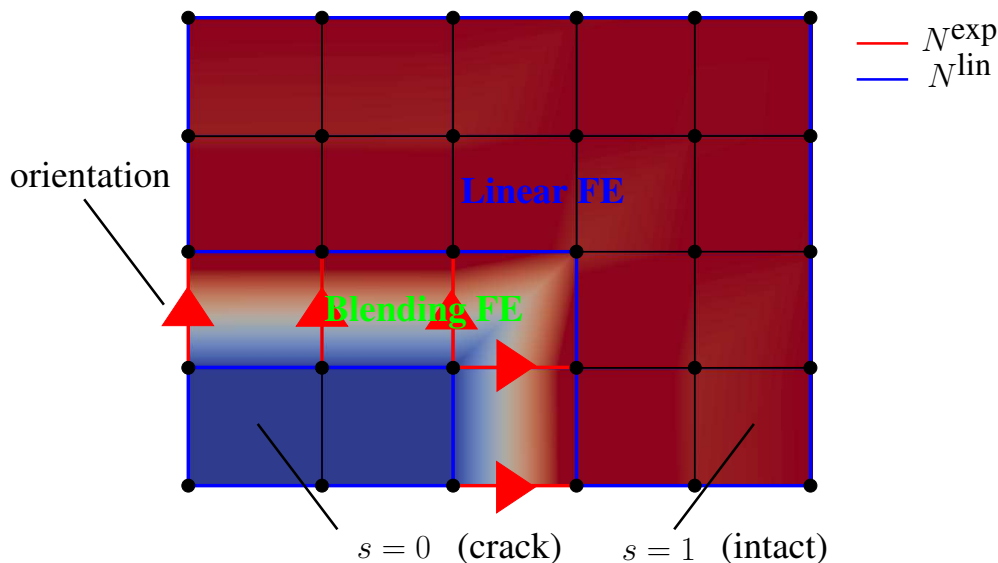


FIGURE 7.4: Scheme of adaptive shape function with blending elements.

For an admissible connection of linear and exponential elements, blending elements are developed. This approach shares most similarities to a local p-refinement, because of the different shape functions, but it doesn't require additional nodes, see Fig. 7.4.

In order to gain maximum flexibility, the proposed blending elements are capable of approximating any combination of linear and exponential properties. This entails that every element edge can become a linear, normal exponential, or mirrored exponential shape function and in the case of a quadrilateral element a total number of 81 different shape functions are possible. But due to restrictions in the orientation, some shape functions are impossible by definition of the gradient, e.g. a fully exponential element with a circular orientation, which would indicate a inconsistency in the phase field. However, most of the 2d blending elements are inversion or rotation of each other and, therefore, are very similar. In order to avoid repetitiveness, only the two most important cases are presented.

The first one is an element with exponential properties in one direction and linear properties in the direction orthogonal to that exponential, i.e.

$$\begin{aligned} N_1^{\text{blend}}(\xi, \eta, \delta_i) &= N_1^{\text{lin}}(\xi) \cdot N_1^{\text{exp}}(\eta, \delta_4), \\ N_2^{\text{blend}}(\xi, \eta, \delta_i) &= N_2^{\text{lin}}(\xi) \cdot N_1^{\text{exp}}(\eta, \delta_2), \\ N_3^{\text{blend}}(\xi, \eta, \delta_i) &= N_2^{\text{lin}}(\xi) \cdot N_2^{\text{exp}}(\eta, \delta_2) \quad \text{and} \\ N_4^{\text{blend}}(\xi, \eta, \delta_i) &= N_1^{\text{lin}}(\xi) \cdot N_2^{\text{exp}}(\eta, \delta_4). \end{aligned} \quad (7.1)$$

This element can be used for vertical crack surfaces, see Fig. 7.5.

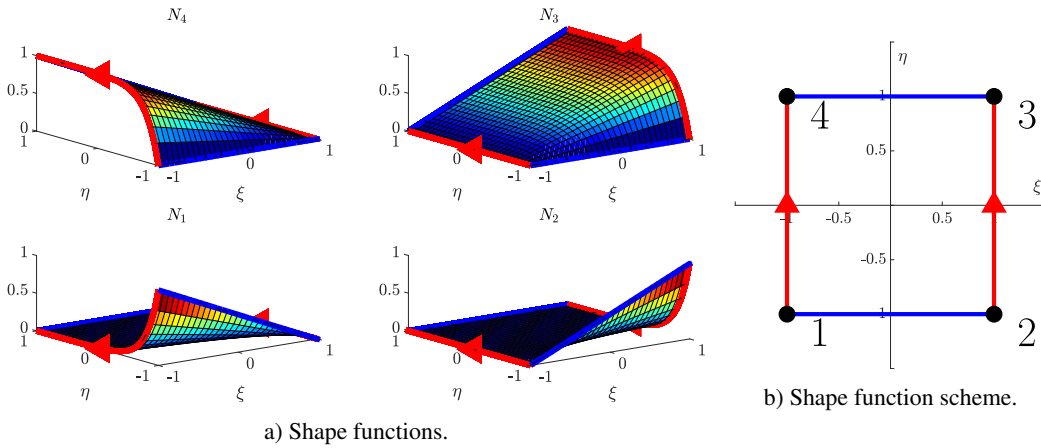


FIGURE 7.5: Shape function combinations for crack surface element with  $\delta_i = 10$ .

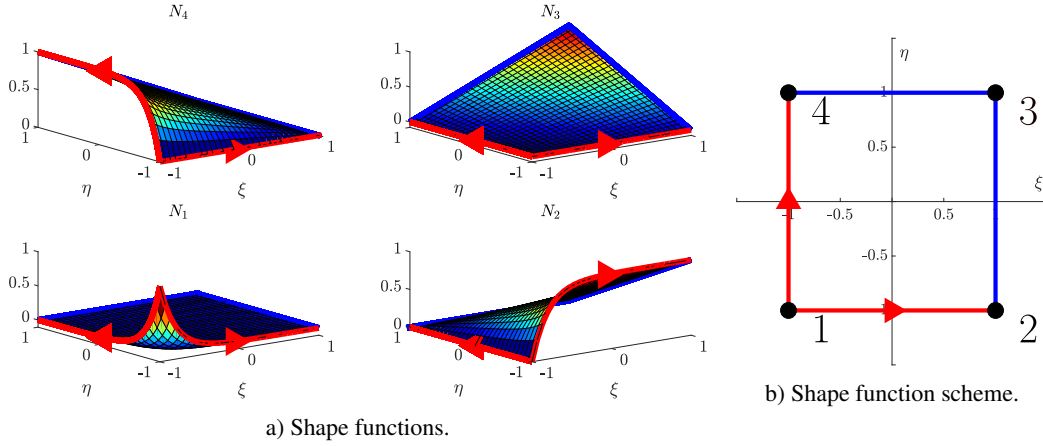


FIGURE 7.6: Shape function combinations for crack surface element with  $\delta_i = 10$ .

The second case is the blending element, with exponential shape functions in one corner with the same orientation and linear shape functions on the opposite edges.

The nodal shape functions are

$$\begin{aligned}
 N_1^{\text{blend}}(\xi, \eta, \delta_i) &= N_1^{\text{exp}}(\xi, \delta_1) \cdot N_1^{\text{exp}}(\eta, \delta_4), \\
 N_2^{\text{blend}}(\xi, \eta, \delta_i) &= N_2^{\text{exp}}(\xi, \delta_1) \cdot N_1^{\text{lin}}(\eta), \\
 N_3^{\text{blend}}(\xi, \eta) &= N_2^{\text{lin}}(\xi) \cdot N_2^{\text{lin}}(\eta) \quad \text{and} \\
 N_4^{\text{blend}}(\xi, \eta, \delta_i) &= N_1^{\text{lin}}(\xi) \cdot N_2^{\text{exp}}(\eta, \delta_4).
 \end{aligned} \tag{7.2}$$

This element is useful for crack tips, here the crack tip is on local node **1**, see Fig. 7.6. Similar to the fully exponential element, the arbitrary blending elements doesn't fulfill the partition of unity. In order to ensure the partition of unity without affecting continuity, every variant of the blending element shape function is modified. The same approach stems from the regular 2d and 3d exponential elements. The residual term

$$R(\xi, \eta, \delta_i) = - \left( \sum_{I=1}^4 N_I^{\text{blend}}(\xi, \eta, \delta_i) \right) + 1 \tag{7.3}$$

of the partition of unity will be used as a correction term. It is equally distributed over all shape functions

$$N_I^{\text{blend}}(\xi, \eta, \delta_i) = N_I^{\text{blend,old}}(\xi, \eta, \delta_i) + \frac{1}{4} R(\xi, \eta, \delta_i). \tag{7.4}$$

The residual term  $R$ , for the first and second case, see Figs. 7.7a and 7.7b. The geometry of the element is approximated by linear shape functions and is the same for both cases. While the combination of the blending elements for a crack tip shows a residual  $R$  similar to that of a fully exponential element, see [42], the blending elements with exponential properties only in one direction fulfil the partition of unity without correction. It is also worth mentioning that the residual term of the crack tip element has a ten times higher residual than the exponential element in this form.

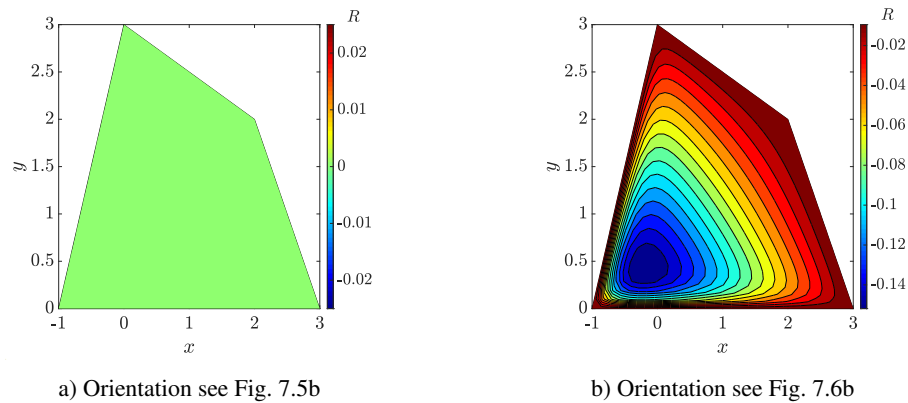


FIGURE 7.7: Contour plot of the residual term  $R$  over the global element geometry.

## 7.5 Application Limits

The exponential shape function's purpose is to approximate the ideal curvature of the crack surfaces in a fracture phase field model. To this point, exponential shape functions, used for the whole model is inefficient and is only possible for a known crack pattern. The developed adaptive strategy has the goal of utilizing the exponential elements where they are required. Thereby, the unnecessary issues like a higher number of Gauß points can be avoided and an ambiguous choice of the accurate orientation of the exponential shape functions are reduced or in the best case scenario, even prevented. In order to evaluate the lower limit for the usage of the exponential approximation of a fracture phase field, a simulation of a crack under tension load is considered, see Fig. 7.16. The mechanical model is a halved quadratic tension probe with a vertically fixed lower boundary and a vertical displacement in the positive direction on the upper side. The phase field of the model is approximated in three different ways, linear, exponential and linear with locally exponential shape functions at the crack surface of the final crack form, see Fig. 7.8. The displacement field is approximated by linear shape functions, so that the number of nodes in the displacement field and phase field are identical. Because of the unambiguous load case, the crack grows on the symmetry line on the lower edge of the model.

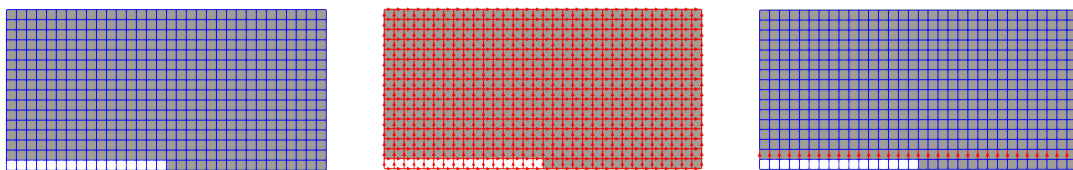


FIGURE 7.8: Different approximated halved tension models with the initial phase field (left: fully lin, middle: fully exp, right: exp only for final crack).

In the test case, the superiority of the exponential shape functions in their approximation of the phase field can be observed, Fig. 7.9. In comparison of the current results with the ones in [42], the used mesh doesn't include an additional element row for the crack path and thus contains the convergence of its reductions in fracture energy and also in elastic energy. The reason for the decreasing effect of the exponential approximation by increasing mesh density is the crack form, which minimally includes one cracked element. This deviates the fracture energy for the crack propagation because the major amount is in this element, see [69]. The model with the local exponential shape functions at the crack surface but only normal to the crack, shows similar results to the fully exponential solution. The example demonstrates that

the full potential of the exponential shape functions lies in their ability to approximate the crack surface. Also, the blending elements show almost the same properties as the computed simulations, which is a proof of their functionality.

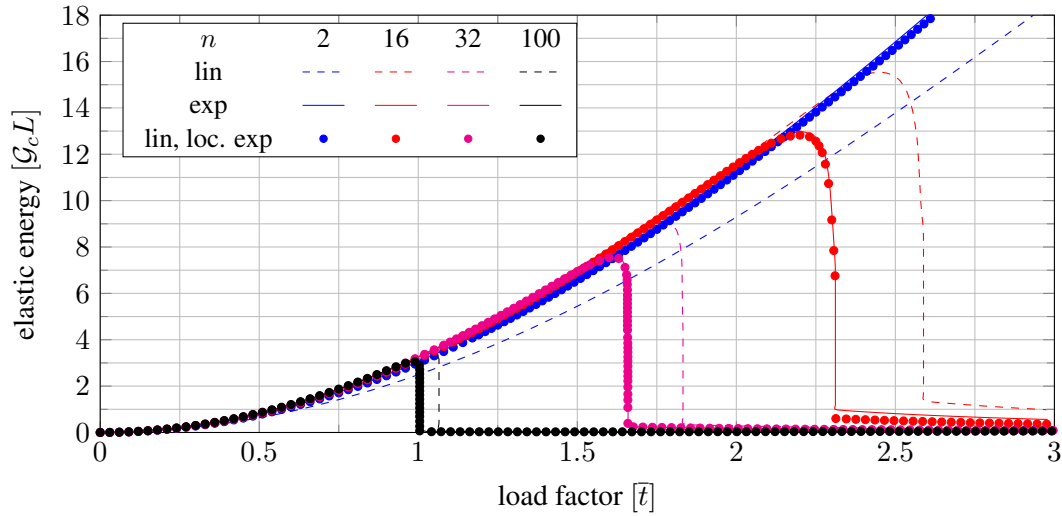


FIGURE 7.9: Surface energy of a halved squared domain under tension for a linear, exponential and linear/local exponential approximated fracture field (only exponential at the final crack) ( $n = 25, 50, 75, 100$ ).

## 7.6 Exponential Crack Tip Influence

The area of interest for the application of the exponential shape function for the approximation of the fracture field is defined by a steep gradient. This includes the crack surface as well as the crack tip. During the development of the adaptive strategy for the usage of exponential shape functions, an unfortunate effect was discovered. This effect causes an undesirable crack growth behaviour or simply put, it causes a crack path that differs from the approximation of the linear fracture phase field solution. Although the crack surface approximation improves with exponentially approximated crack surfaces, there are certain side effects at the crack tip. The crack field at the tip is unstable during crack growth and the emerging crack's development over time does not yield an exponential crack surface solution. Thereby, the solution process becomes unstable under the adaptive algorithm in order to determine the precise crack form. This cause numerical difficulties, like a diverging or oscillating solution. These problems can be handled by the cut off limits of the adaptive algorithm. The second difficulty with the use of exponential shape functions at the crack is their influence on the crack growth direction. Therefore, an example is presented in Fig. 7.10, which displays the final crack path and phase field shape functions for the simple shear test described in subsection 7.9.3. The load case is approximated by a linear fracture field and two adaptive strategies, whereby the two different adaptive strategies differ by an additional rule for the approximation of the crack tip. At this point, it is not yet crucial how the algorithm is structured, since the described influence has been observed consistently in different variations of the adaptive algorithm.

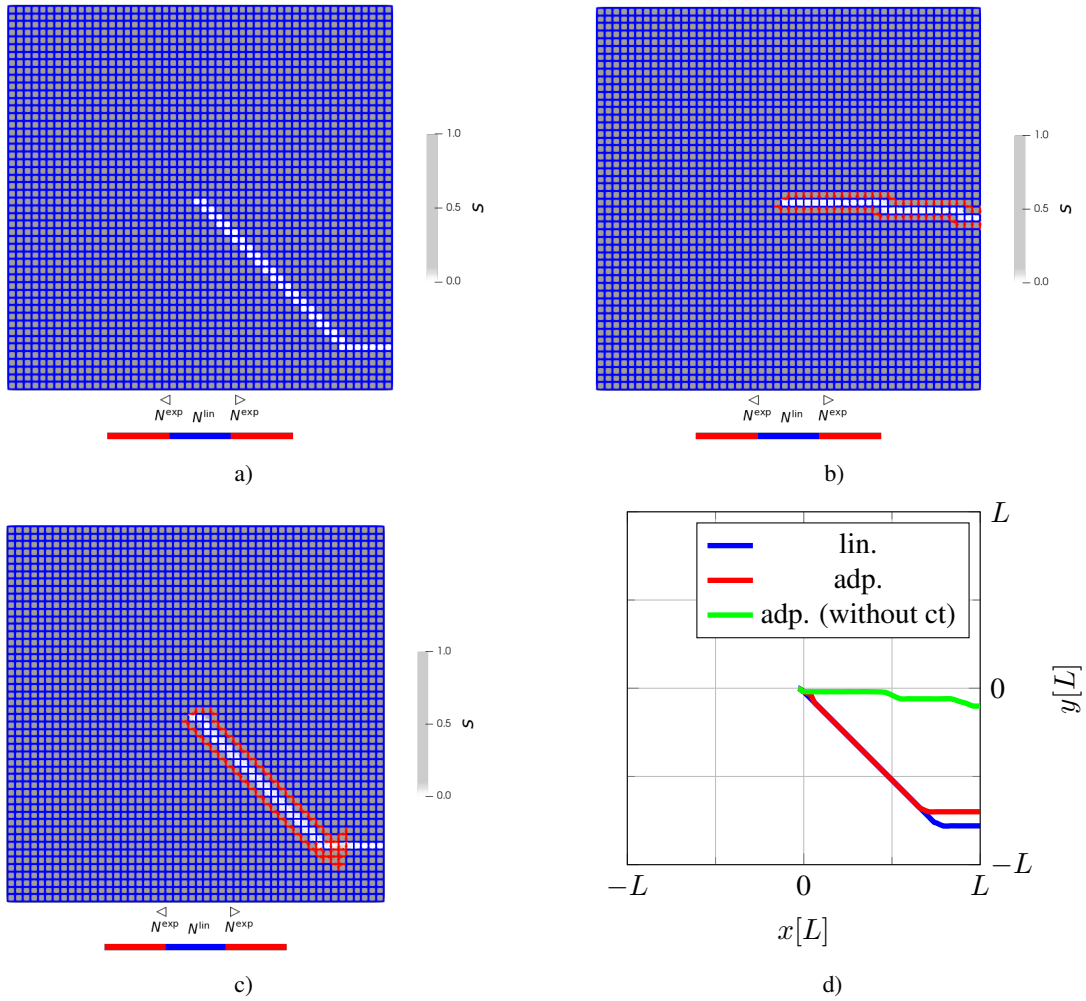


FIGURE 7.10: Different approximated simple shear models with the initial phase field (a) fully lin, b) adp, c) adp without crack tip).

The adaptive algorithm shows in Fig. 7.10d, compared to the linear solution, a different crack path. This outcome is undesirable, because the deviated solution does not allow for a comparison. Therefore, a solution of this issue is the exclusion of the crack tip from the adaptive algorithm to circumvent the varying crack growth path. Of course, with the rising complexity of the adaptive algorithm and additional conditions, the application becomes more cumbersome. The algorithm thus requires two more steps, a tracking of the crack tip and a computation of the distance between the refined edge and the crack tip. The crack tip tracking is modeled after the strategy by [64]. Thereby, the crack tip is defined by the node with a phase field value lower than a certain limit and has the farthest distance from the initial crack. An issue that arises from the exclusion of the crack tip from the adaptive algorithm is a delay in the accuracy of the approximation of the crack surface.

## 7.7 Marking Strategy

The adaptive shape function algorithm is different in principle compared to standard mesh refinement techniques, but they share the same objective, improving the solution through refined discretization. For a novel algorithm, tailored strategies are applied, which are based on already well known procedures like the marking strategy and the refinement rule, see [73]. They define the criteria that chose the elements, which indicate a defined excess of

inaccuracy and propose an increase in the refinement level. In the case of adaptive shape functions, which only contain two discrete levels of refinement, linear or exponential shape functions, the refinement rule becomes redundant or can simply be viewed as part of the marking strategy. Thus, the focus lies solely on the marking strategy and its algorithm. The term "marking strategy" comes from the marking of elements that are highlighted or recommended for refinement. The evaluation is achieved by the computation of a marking value  $\eta_k$ , which has in general, the form of an error estimator. Definitions for error estimators for fracture phase field models can be found in [74] and [49]. However, the phase field properties also facilitate an approach that utilizes the phase field itself as an error estimator in a broader sense because the phase field requires a refined area in the transition zone, which is indicated by the phase field values between the phase indicating values, e.g. in the used model, 0 for cracked and 1 for undamaged. For a fracture field model in [56], the fracture field is used as an error estimator to refine areas near the crack. Although in the latter case, in which only the phase field is assessed, the error of the displacement field is disregarded. The developed algorithm for adaptive shape functions, where refinement is only applied to the fracture phase field, an error estimator, that contains the displacement field would erroneously apply exponential shape functions to the fracture phase field in areas without any significant gradient. The applied exponential shape couldn't be properly oriented and would be, in the best case, redundant or in the worst case, incorrectly oriented. Therefore, a marker is defined based only on the phase field or its derivative.

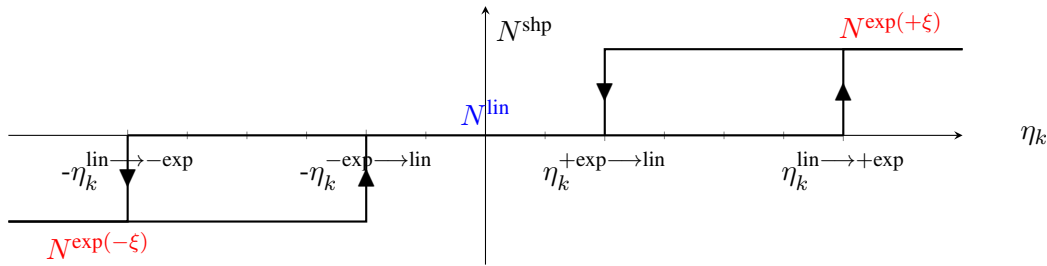


FIGURE 7.11: Schematic for marking strategy.

A schematic function for the choice of shape function, which is applied for each edge of the mesh, is displayed in Fig. 7.11. The function contains two limits for the transition, one for the change from a linear to an exponential and another for the de-refinement from an exponential to a linear shape function. This hysteresis-like characteristic is implemented to avoid oscillation between two differently approximated solutions. Further, the limits  $\eta_k$  for the transition from a linear to an exponential shape function and vice versa are independent of the orientation for a symmetric behaviour of opposite crack surfaces. This marking function, in a sense, also defines the refinement rule. The important point of the marking strategy is the definition of the marking value  $\eta_k$ , whereby the options are limitless and there is no unique property that stands out as the optimal solution. For a visual review of the specification for different marking values, Fig. 7.12 is plotted. Thereby, the main local output values of a phase field fracture model at a single growing crack are depicted, like the fracture field  $s$ , the norm of the fracture field gradient  $|\nabla s|$  and the velocity of the fracture field  $\dot{s}$ . The gradient and the actual phase field are based on the same solution vector. In order for a better geometric visualization of the crack, iso-lines of the fracture field  $s$  with the value 0.25 are included in the plots. The choice of the phase field value of 0.25 is based on the literature [13], where it is described as a sufficient fracture field value for the definition of the crack geometry.

Due to the properties of the phase field  $s$ , the iso-lines of the phase field reveal the transition areas, the crack surfaces and are therefore selected as the main criterion. Unfortunately,

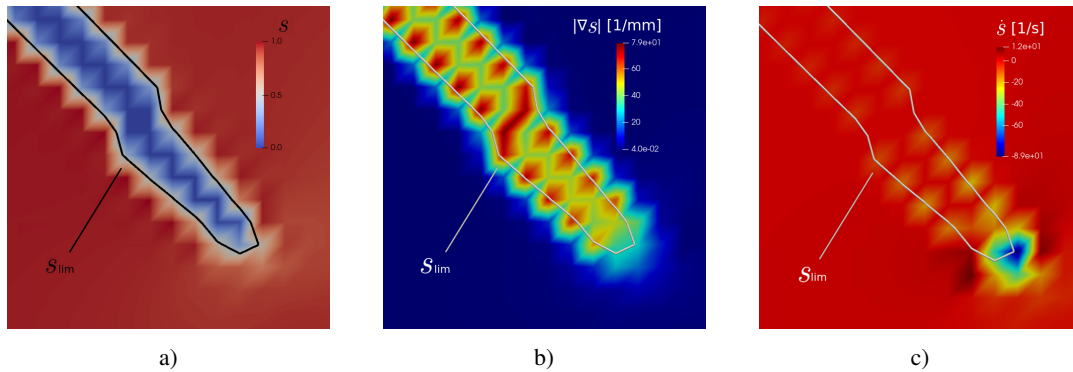


FIGURE 7.12: Fracture field  $s$  a), norm of the fracture field gradient  $|\nabla s|$  b) and velocity of the fracture field  $\dot{s}$  c) displayed for the same crack.

the computation of isolines is rather numerically expensive [69]. The second option is the gradient of the fracture phase field or more specifically, the norm of the gradient extrapolated by the Gauß point values. Corresponding to the phase field  $s$ , the gradient of it also reveals the crack surface and furthermore, a growing crack tip, which differs to an evolved crack surface by a reduced gradient. A gradient based marking strategy could be defined with an additional condition to exclude the crack tip, but the gradient's directional dependence can favour an element edge-dependent crack path and is therefore not recommended. Similar to the gradient, the crack field rate  $\dot{s}$  as a criterion for the adaptive shape functions can also capture crack tips for an exclusion rule. Unfortunately, the rate of the phase field  $s$  has a massive drawback, its highly fluctuating values makes it difficult to define a function for the marking strategy. So, in comparison, the most feasible marking value is the phase field, which is independent of the meshing, automatically normed by definition and contains information about the orientation direction.

## 7.8 Process Sequence

The adaptive shape function algorithm is yet to be presented, but besides its process, its position in the sequence of the FEM program should be discussed first. Thereby, the established adaptive refinement methods serve as a comparison. In general, the first step of a Finite Element program is the pre-processor, whereby input data, e.g. material and mesh properties, are defined. For the developed adaptive algorithm, additionally, the initial shape functions need to be selected, and a reasonable choice is linear shape functions. Based on linear shape functions for the whole model as an initialization, the following shape functions are based on the phase field  $s$ . Therefore, the adaptive algorithm is an a posteriori scheme, because it uses the initial shape functions to compute an approximation and then analyzes the solution in order to adapt the shape functions in an iterative process. This is repeated until a user defined criterion is fulfilled. A similar approach is already classified by Babuška et al. [7] and is called a feedback technique. For the fracture phase field model, the simulation is a transient analysis, whereby the load in general is increased over time. The whole process contains two loops, the solution loop and the time step loop. Both are already implemented in the FEM program FEAP, see [72]. The time step loop is adaptively controlled by an algorithm approximated by a heuristic function, which increases or decreases the time step in the case of a converged or non-converged solution step. Within the time step loop, the non-linear equation system for the phase field fracture model is solved using a Newton-Raphson iteration scheme. The method finds the solution  $\underline{d}_{n+1}$  and is described in more detailed form in the chapter 3. The sequence developed and implemented in the general process for this work is the adaptive loop. The options for the position in the simulation process are either during the Newton iteration or during a time step. While the first possibility seems to be more efficient, because of the reduced loop count, there are some drawbacks. If the shape functions are changed during the Newton iteration, the process requires a staggered solution strategy in order to avoid a dependence of the shape functions  $N^s$  on their approximated solution, the fracture field  $s$ . Therefore, the choice falls on an additional loop outside of the Newton iteration, see Fig. 7.13. The adaptive loop has the loop iterator  $j$  and it wraps the Newton Iteration. In the case of a non-converged Newton step, the time step control reduces the time step size and then repeats the Newton loop. The numeric effort of the adaptive loop compared to the Newton iteration is less because it doesn't involve any matrix computation or time-consuming calculation steps. In the first step after a successful Newton iteration, the fracture phase field is evaluated and the edges are selected for refinement. This is called the marking strategy and is explained in detail in the last subsection. The shape functions of the actual step and the next adaptive step of each edge are then compared and a criterion checks whether certain shape functions fulfill the requirements. After all edges are evaluated, the adaptive algorithm checks for any shape function changes and in the absence of any, the next time step is computed, otherwise the Newton loop is repeated.

The details of the adaptive shape function algorithm, including the specifics of the evaluation of all edges, are separately outlined in Algorithm 1. The algorithm requires the parameters  $s_{\text{lower limit}}$ ,  $s_{\text{upper limit}}$  and  $r$ . The two phase values characterize the mentioned  $\eta$  values. They define the change of the edge shape functions from linear to exponential and exponential to linear shape functions. The parameter  $r$  is a radius for the circle around the crack tip, which restricts any exponential shape function to a certain distance from it. Before each edge is evaluated, the crack tip is defined. So, in total, the edge shape functions depend on the distance of the crack tip, the phase field values and the shape function in the last adaptive iteration step.

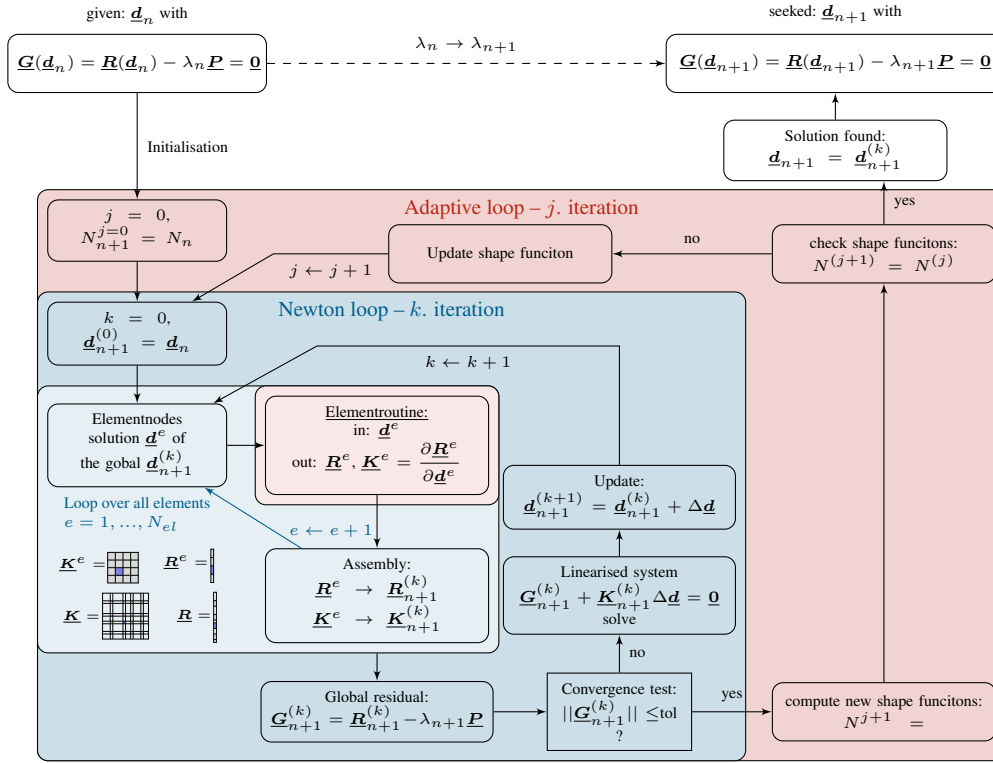


FIGURE 7.13: Schematic solution process.

**Algorithm 1** Adaptive Shape function algorithm

---

```

load parameter  $s_{\text{lower limit}}$ ,  $s_{\text{upper limit}}$ ,  $r$ 
load  $\text{shp}_n$ 
Find  $\vec{x}_{\text{crack tip}}$ 
for  $i \leftarrow 1$  to total number of element edges do
  load phase field value  $s_i(1, 2)$  of edge  $i$ 
  compute position edge centre  $\vec{x}_{\text{edge}}$ 
  sort  $s_k(k = 1, 2)$  by size
  if  $\text{shp} = \text{lin}$  then
    if  $s_{\text{min}} < s_{\text{upper limit}}$  and  $s_{\text{max}} > s_{\text{lower limit}}$  and  $\|\vec{x}_{\text{crack tip}} - \vec{x}_{\text{edge}}\| > r$  then
       $\text{shp}_{n+1} = \pm \exp(\pm \text{defined by sign}(s_1 - s_2))$ 
    else
       $\text{shp}_{n+1} = \text{shp}_n$ 
    end if
  else if  $\text{shp} = \text{exp}$  then
    if  $s_{\text{min}} > \beta \cdot s_{\text{upper limit}}$  or  $s_{\text{max}} < \beta \cdot s_{\text{lower limit}}$  then
       $\text{shp}_{n+1} = \text{lin}$ 
    else
       $\text{shp}_{n+1} = \text{shp}_n$ 
    end if
  end if
end for
  
```

---

## 7.9 Evaluation

In the original paper on the exponential shape functions for a phase field fracture model [42], the comparison of different simulations is done for a linear and exponential approximation of the fracture phase field. Their proposed approach with a different approximation of the actual and virtual fracture fields is disregarded, because of the loss of symmetry of the tangent matrix. In order to evaluate the adaptive strategy, both linear and exponential solutions are required for a proper estimation of the effectiveness of the adaptive solution in terms of accuracy increase. The simulation of an exponentially approximated fracture phase field requires a proper orientation. For cases with a straight growing crack under tension, the orientation of the exponential shape functions can be predefined, but for more complex load cases, the right orientation needs to be gained. So, the first step is the generation of an exponential solution. The objective of this work is the evaluation of an adaptive approximated phase field. The expected results are an interpolation of a linear and an exponential solution. This should be predictable, because of the nature of the algorithm. The algorithm should approximate an almost fully developed crack surfaces with exponential shape functions and use linear shape functions in any other part of the domain for the phase field  $s$ . Of course, the algorithm repeats iterated steps to refine each time step in terms of the advantageous shape function, but a delay in the algorithm can be expected. Another important point for the comparison is the high ratio  $\delta = h/l_c$  of the element size  $h$  and the crack width  $l_c$ . In cases with a ratio equal to one or smaller, exponential functions lose their necessity because the characteristics of an exponential shape function change with a lower ratio to a linear function. In order to meet this condition, the crack width is chosen lower than the recommended ratio of one to ten for the smallest geometrical dimension. The model/material parameters are listed in Tab. 6.1. They are adopted from [42] for all subsequent simulations. The main aspects are that  $\lambda = \mu, \eta$  and  $M$  are relatively small.

### 7.9.1 Local Exponential Solution

As mentioned in the introduction of this chapter, exponential shape functions were used in models with a unique crack path, which only applies to straight growing cracks in a tension test. The elements have to be oriented in the direction of the crack in order to avoid the influence of the discretization on the crack's growth. In any case, if it does not fulfill this premise, the crack path becomes ambiguous and e.g. depends on the mesh, especially for the high ratio of element edge size  $h$  and regularization width  $l_c$ . As an illustration of the dependency of the crack growth on the mesh, a simple shear load case is considered. The analyzed load case, with a uniform mesh, is presented in detail in subsection 7.9.3. In general, the crack grows under roughly  $45^\circ$ , where the angle and form also depend on the mesh density. For comparison, the discretization is changed in density and form, while the boundary condition and geometry are not altered. The example for the form alteration of the mesh is done by orienting the elements in the domain of the crack growth in the direction of the crack propagation. In order to avoid significant changes in the mesh density, the element count is only doubled. The results of the final crack shape are depicted in Fig. 7.14 by displaying the fracture phase field of the finite element solution and a sharp crack approximation. The difference in the crack path reaches its maximum at the end of the crack, or more accurately, at the domain borders. The mesh with a different form compared to the original mesh reinforces the crack to grow into the lower left domain corner, while the different mesh density moves the crack end closer to this position, but continues a similar path compared to the less dense mesh. Of course, the geometry in this case is simple in comparison with real structures. Therefore, this model is only viewed as a study to demonstrate the effects of different meshes in density and

shape on a solution for a fracture phase field model. Further information about the influence of discretization on the solution of a fracture phase field model can be found in [29].

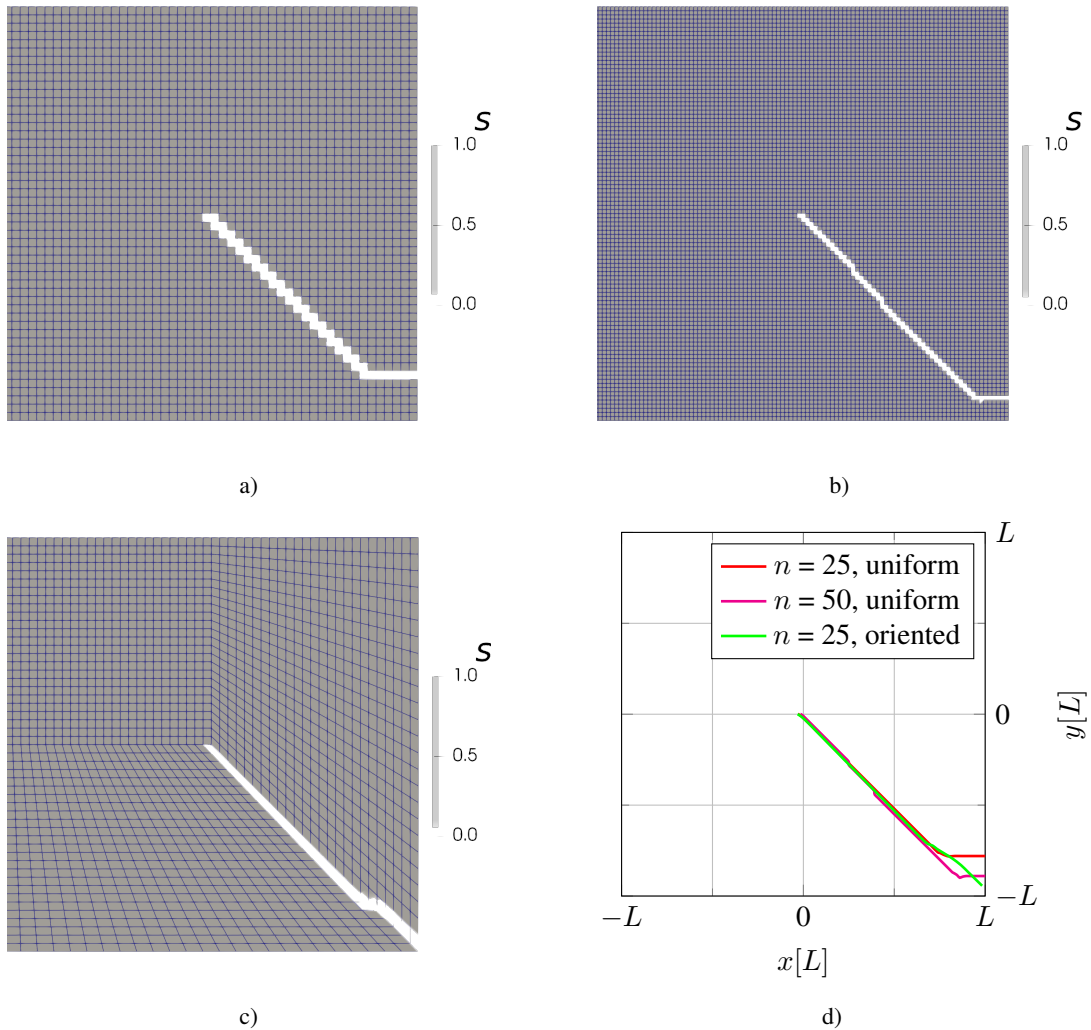


FIGURE 7.14: Final crack from of a simple shear test with an mesh  $50 \times 50$  (upper left), a higher mesh density  $100 \times 100$  (upper right), differently shaped mesh (lower left) and the sharply approximated crack paths in comparison.

The presented simulations with different meshes can be viewed from the perspective of the implementation of exponential shape functions or more specifically, their correct alignment. In essence, without any prior knowledge of the resulting crack path of each individual simulation model, the exponential elements can't be implemented beforehand. In order to evaluate the effectiveness of the adaptive approach, an upper limit of improvement in the exponential elements is required. Therefore, a static exponential solution is searched with the condition of an initial choice of shape functions that approximate the crack surfaces of the final crack a priori without any changes during the simulation. A practical approach is proposed, whose first step includes the computation of the model with a complete linear approximated phase field until the crack is finalized ( $t = t_{\text{end}}$ ). The final fracture phase field serves as an interim solution and is refined with exponential shape functions on the final crack surfaces with the proper orientation. In cases of a converged solution, the adapted discretization with the additional exponential edges at the crack surfaces could be repeated and would result in the same final crack form, where the shape function choice is a quasi static exponential solution.

But an issue that occurs, which is similar to the influence of the different meshes on the fracture phase field solution, is that the repeated computation of the altered model doesn't result in the same crack growth, see Fig. 7.15. The crack in the adapted model with local exponential shape functions produces a different crack. This leads to an approximated phase field with a crack surface that is partially exponential and linearly approximated. In order to gain a solution with a final crack that aligns with all implemented exponential shape functions, the process is repeated. So, in further simulation cycles of solving the model and adapting the shape functions, the final solution reaches agreement with the phase field and its refined crack surface approximation. This procedure offers no security for the optimal solution and can only be used as a comparative result for the adaptive solution. In a way, the generated solution is also the result of an adaptive process, but with the cycle outside the simulation.

---

**Algorithm 2** Generate local exponential solution
 

---

```

1: Initialize:  $k_{\text{adap}} = 1$ 
2:  $\text{shp}_{k_{\text{adap}}=1} = \text{lin} \quad \forall k, \quad N_k^{\text{shp}}(\xi_i, \delta_i)$ 
3: while  $\text{shp}_{k_{\text{adap}}} \neq \text{shp}_{k_{\text{adap}}-1}$  do
4:    $k_{\text{adap}} + = 1$ 
5:   while  $t < t_E$  do
6:     Update:  $t_n + 1 = t + \Delta t$ 
7:     while not converged do
8:       Newton's method
9:     end while
10:  end while
11:  Adaptive Routine
12: end while

```

---

The described process in detail is listed in Algorithm 2. It contains three loops corresponding to the adaptive algorithm. The iterator of the adaptive loop outside the simulation process has the iterator  $k$ . In the following interpretation of the results, the process to generate an exponential solution is successful but requires a higher element count and more cycles. The adaptive approach for the exponential elements is compared to results generated by a semi-adaptive approach. The behaviour observed in the application of exponential elements as static, a priori and adaptive without the exclusion of crack tips show the similar form of the crack path. Only by excluding exponential approximations at the crack tip does the adaptive algorithm keep the crack path closer to the linear solution. Although, in the end, the exponential solution produced by this iterative process is not exclusively exponential and can not be viewed as the ideal approximated exponential solution, the term exponential solution is used in the following analysis for the sake of simplicity.

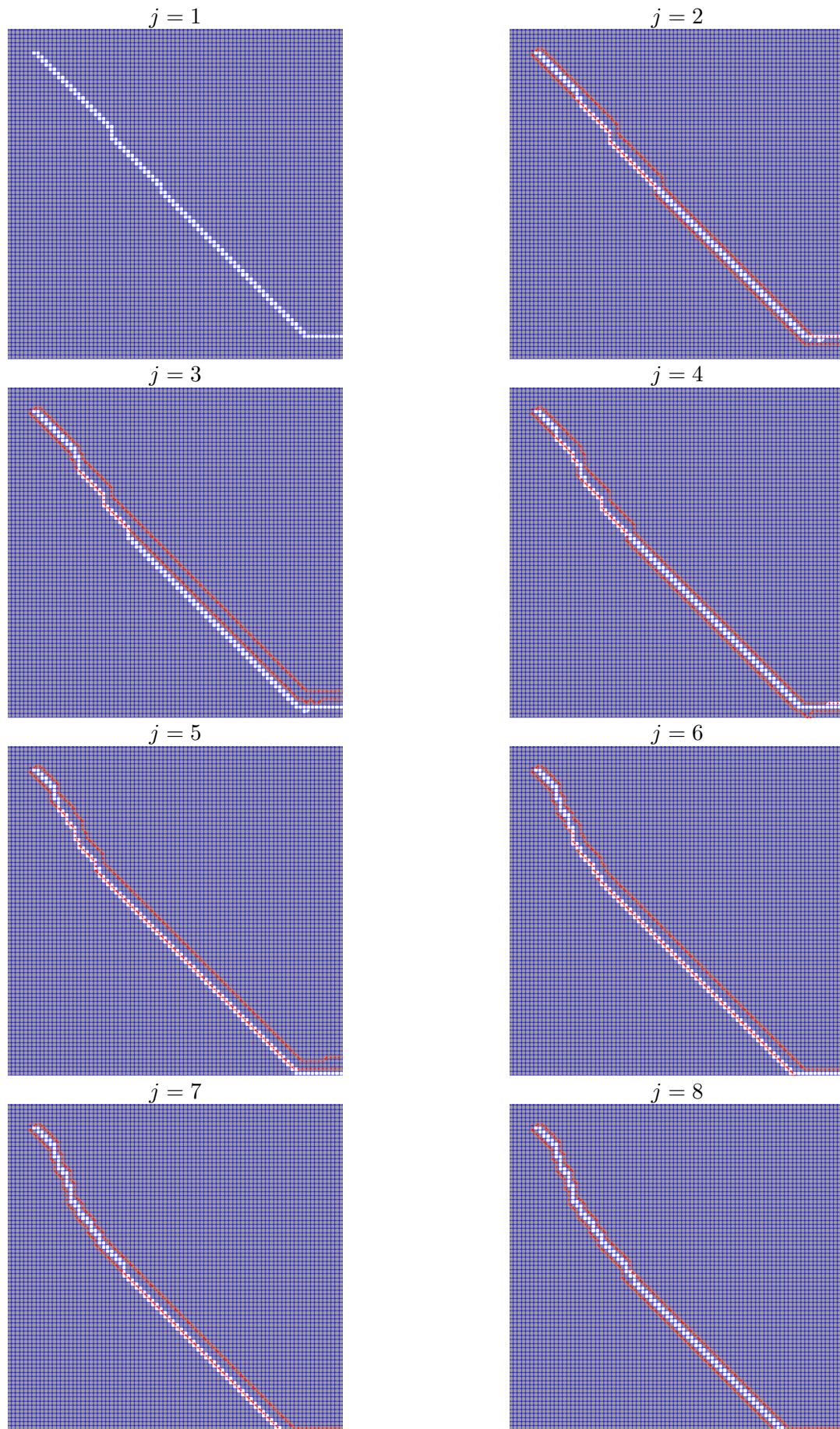


FIGURE 7.15: Results of repeated simulation of the simple shear test with adapted shape functions based on the prior simulation (mesh size:  $n = 75 \times 75$ )

## 7.9.2 Halved Tension Test

The most elementary mechanical test for the analysis of crack growth is a tension test in the form of a quadratic or rectangular probe. The following model is adopted from the peel-off test presented in [42] and has the form of a halved quadratic domain with an initial crack half the size of the domain at the symmetry border. The used model differs from the original model in its meshing that it doesn't contain an additional row of very fine elements for the crack, as well as no bias element size towards the crack tip from the left border of the domain. The final crack grows unambiguously in any circumstance, always along the lower border until the initial crack reaches the right border. This is not influenced by any presented approximation, which differs in mesh size and shape functions. Tab. 7.1 contains the parameter chosen for the adaptive algorithm 1. The values  $p_1$  and  $p_2$  are limits for the phase field of each edge and are closer to the undamaged value of 1 to capture the crack surface near the crack tip in an early stage of its propagation. In simulations, limits lower than 0.5 showed less exponential shape functions near moving crack tip, which results in an adaptive scheme without any improved approximation of the crack propagation. Basically, the influence on the improvement of the approximation of the exponential shape functions depends highly on captured amount of emerging crack surface. Unfortunately, accruing crack surfaces in fracture phase field models are less unambiguous in their orientation, therefore an adaptive algorithm without limits at the crack tip can result in convergence difficulties.

TABLE 7.1: Adaptive shape function parameter.

parameter	value
$p_1$	0.75
$p_2$	0.85
$r$	$5\bar{h}$

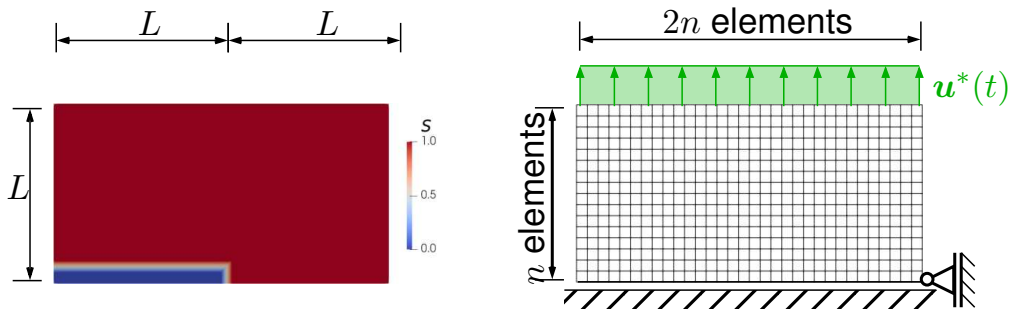


FIGURE 7.16: Contour plot of initial crack field (left) and mechanical model of the tension test (right).

The effect of the adaptive strategy is best illustrated by the elastic energy, see Fig. 7.17. The curves can be divided into shape functions, linear, exponential (local) and adaptive, with mesh densities of 2, 16, 32 and 100 for the variable  $n$ . In the initial prediction, the solution of the elastic energy with an adaptive strategy is assumed to lie between the linear and exponential solutions. The data also supports this presumption. The improvement of the adaptive algorithm declines with a higher mesh density, which is the result of the convergence of the linear solution towards an accurate approximation of the crack surfaces. Compared to the example model with an additional row of elements for the crack path from [42], none of the approximated models present a converged solution. This issue is a consequence of the Finite Element Method, which evaluates the element values in the Gauß points and requires a fully degraded element instead of a fully degraded node. Thus, the crack isn't described

by a single node but by an element, which approximates a bigger crack width than intended. Therefore, the high ratio of element size to regularization width causes a greater error than the improvement through the exponential approximation of the crack surface.

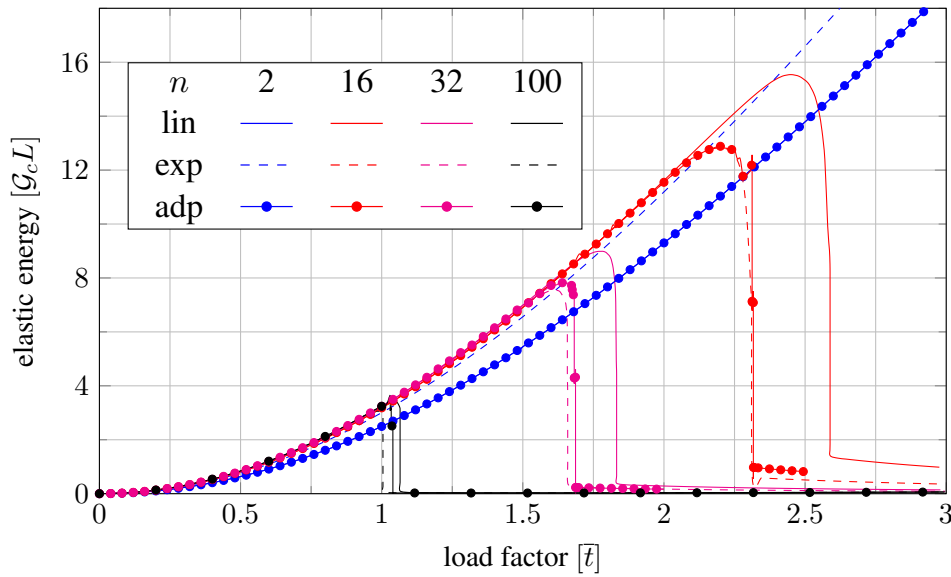


FIGURE 7.17: Elastic energy obtained with linear/local exponential/adaptive shape functions for a halved tension test with a uniform mesh.

The exponential shape functions benefit from a mapped mesh because the correction term is not required, which is also true for most adaptive elements with linear and exponential characteristics. So, in order to provide evidence that the influence of the mesh quality is not paramount for the effectiveness of the adaptive strategy, an altered mesh is tested. The mapped meshes from the analysis before are used for the distorted meshes, that are analyzed in the following, see Fig. 7.18. Therefore, all nodes are altered in  $x$  and  $y$  directions randomly. Thereby, the nodes on the boundaries are altered only tangentially to the boundary in order to avoid any violation of the geometric description of the domain. In comparison, of the elastic energy, the orderly mesh with uniformly sized elements and the linear approximation of the fracture field do not show a singular drop of the energy during crack propagation but a slight step for the drop of the curves, see Fig. 7.19. In the case of the exponential solution, the same behaviour can be observed. This also applies to the adaptive solution, where the discontinuities in the crack growth are very pronounced. It provides a good conception of the influence of the discretization of phase field models, which can also be observed by the results provided by the computation with the presented adaptive strategy with mixed shape functions. The consideration of the elastic energies of the linear, exponential and adaptive approximations in comparison to the unordered network shows the same behavior as in the ordered network. This shows that exponential and mixed-approximate elements improve the approximation despite correction terms.

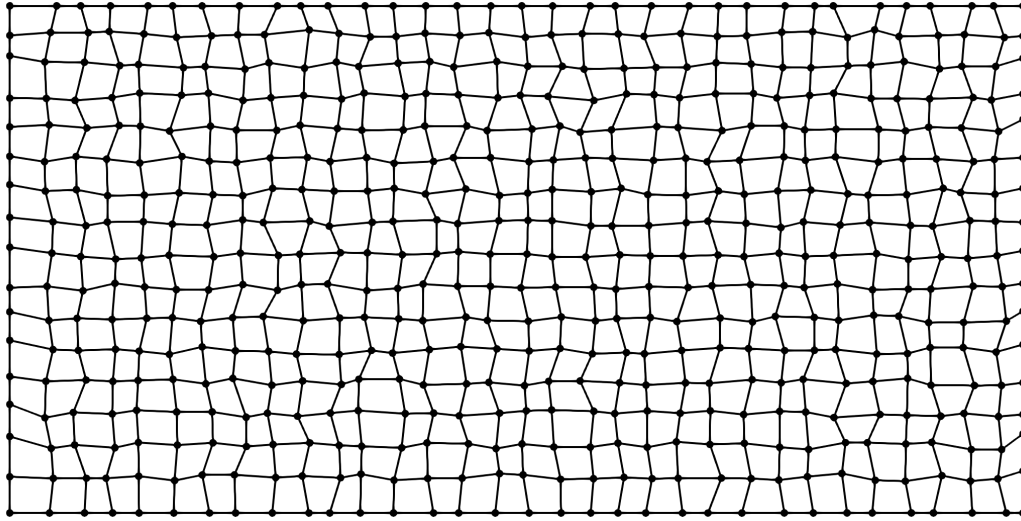


FIGURE 7.18: Irregular mesh of the tension test model comply with the boundary dimension.

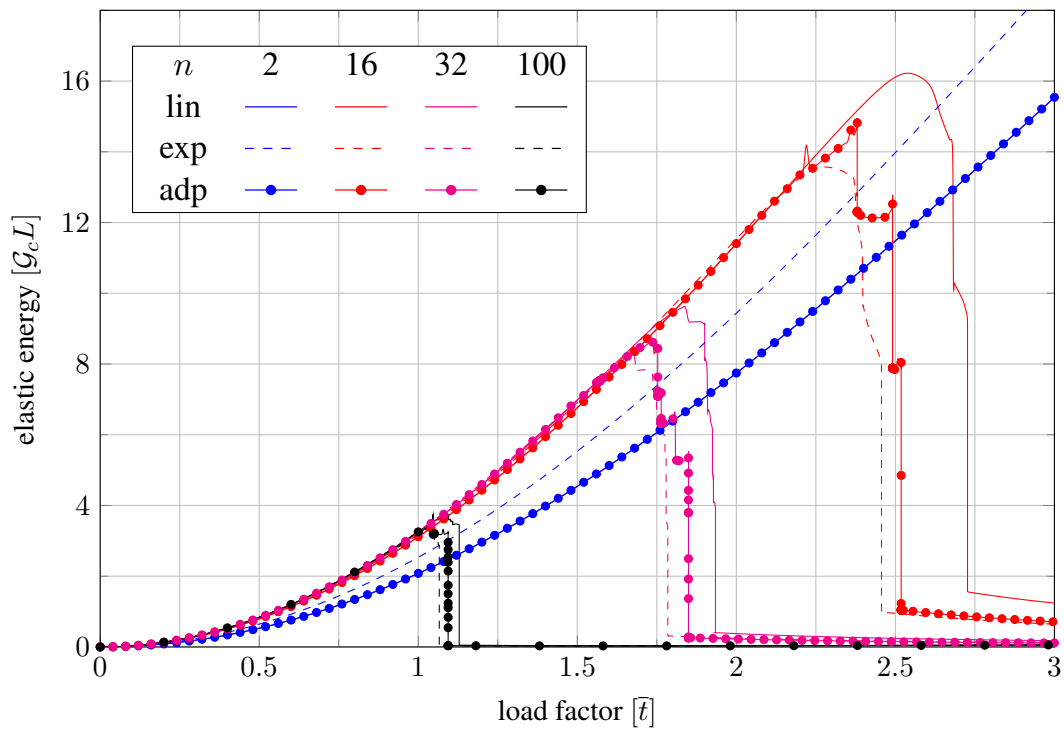


FIGURE 7.19: Elastic energy obtained with linear/local exponential/adaptive shape functions for a halved tension test with a irregular mesh.

### 7.9.3 Simple Shear Test

In comparison to the tension test, the simple shear test is more complex because of the unknown crack path, which can vary with mesh and fracture phase field model parameters. This makes an approximation with pre-defined exponential shape functions impossible without prior results. In order to generate a comparable solution for the results with the adaptive approximation, an iterative strategy is used. Based on the presented approach in subsection 7.9.1, the exponential or more specifically, local exponential solution, is achieved.

The simple shear test is already investigated in other works like [49] and requires a tension-compression split to approximate the crack growth only in the direction of the domain under positive volumetric strain. In the following cases, the split based on the deviatoric decomposition is utilized. The computed load scenario is a squared domain with an initial crack in the form of two geometrically overlapping edges, which has a greater stiffness than a similar phase field crack. On the lower border, the domain is fixed and edges on the left and right are fixed in their parallel directions, which results in a fixed height. On the upper edge, the load is applied in the form of a fixed spatial constant displacement increasing linear in time in the vertical direction and the edge is fixed in its normal direction, see Fig. 7.20. With the crack, the geometric split of the left half of the domain already contains an initial crack, so that the fracture phase field for  $t_0$  is intact over all nodes.

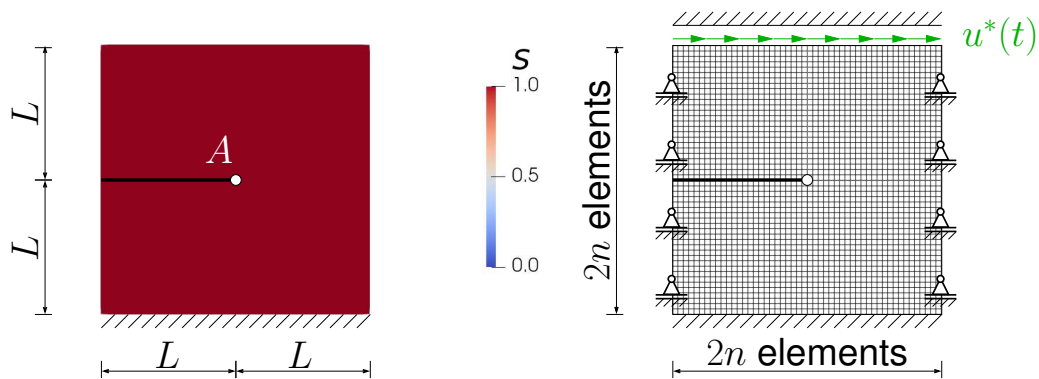


FIGURE 7.20: Contour plot of initial crack field (left) and mechanical model of the simple shear test (right).

The final crack form is displayed in Fig. 7.21 for a discretization with  $200 \times 200$  elements over the domain with a linear approximation of the fracture field. The model parameters are the same as in the tension test and can be found in Tab. 6.1. In the following, the crack paths are compared because, in comparison to the tension test, the shear test in different configurations has an effect on the crack path, which is not unambiguous.

The crack paths for the three different approximations of the phase field are in good agreement with each other, but the adaptive and the linear solutions are a better match, which is an effect of the linear approximation of the crack tip during crack propagation, see Fig 7.22. Discretizing with a mesh that contains elements oriented in the direction of the propagation of the crack, e.g. Fig. 7.14 a smoother curve of the energies can be observed, like the tension test.

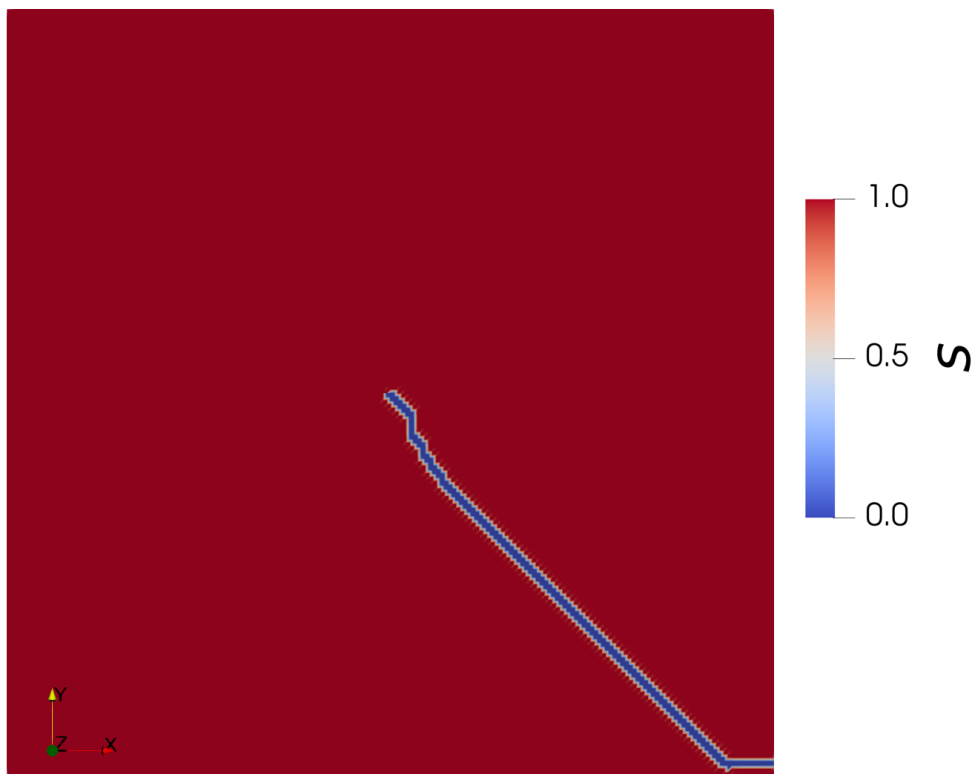


FIGURE 7.21: Simple shear test: Contour plot of the phase field  $s$  displaying the final crack form ( $100 \times 100$  elements).

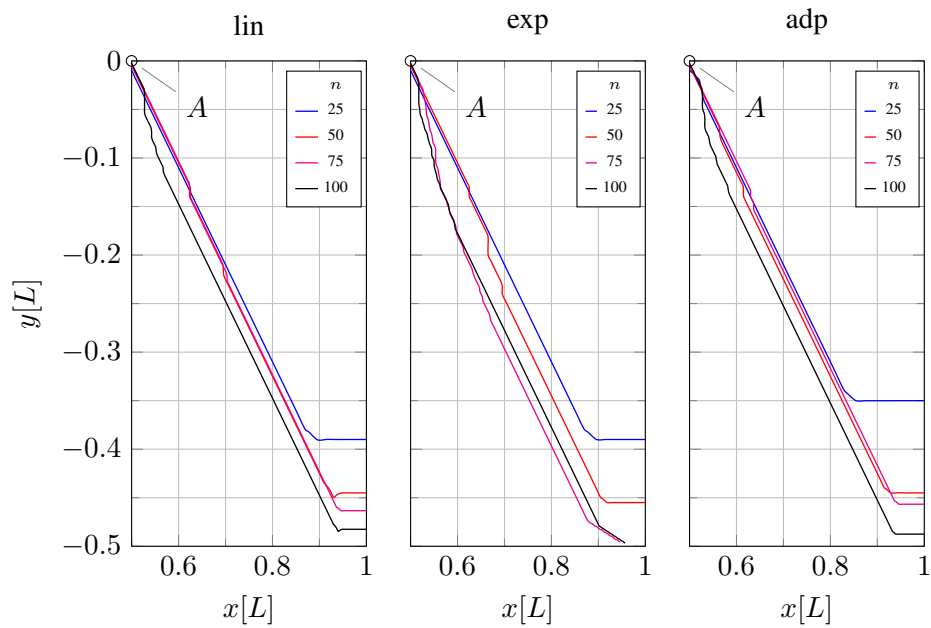


FIGURE 7.22: Crack path of the simple shear test with linear/local exponential/adaptive shape functions over the discretization.

The elastic energy displayed for different mesh densities and discretization gives a similar representation compared to the results of the tension test, see Fig. 7.23. The curves of the adaptive solutions are between exponential and linear ones, as is to be expected. An effect that can be observed for all results is the non-smooth representation of the elastic energy, which was also observed in the irregular mesh, see Fig 7.19.

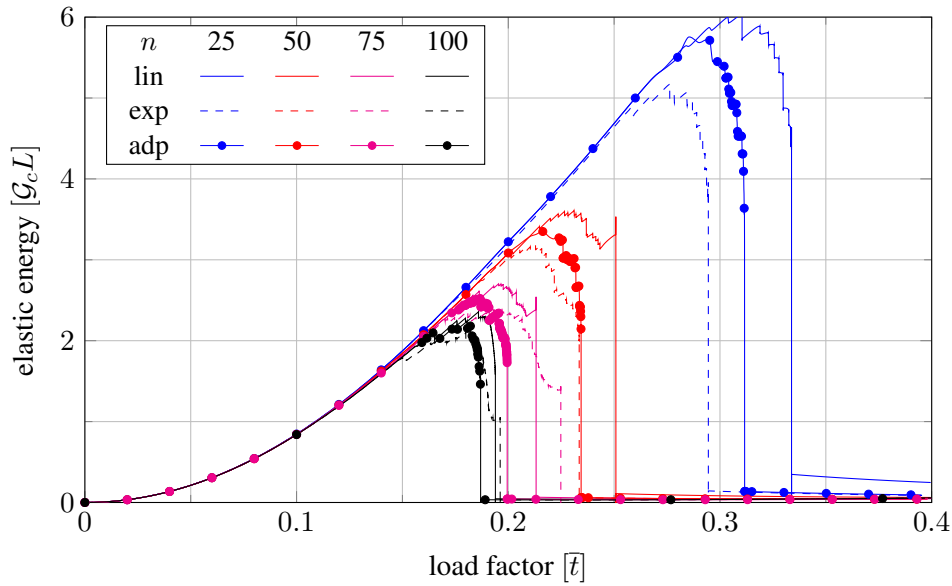


FIGURE 7.23: Elastic energy obtained with linear/local exponential/adaptive shape functions for a simple shear test.

### 7.9.4 Halved Peel-off Test

The tests beforehand dealt less complex load cases, so another more advanced test for the validation of the adaptive shape function algorithm is performed. Therefore, a benchmark problem for a phase field model proposed in [68] describing a 2d peel-off test is employed. The domain of the problem is a rectangle with a ratio of 2:1 for the horizontal to vertical edge size. In the center of the upper side, a displacement condition is applied symmetrically over half its size. The condition defines a uniform displacement of the area in the vertical direction, growing linear with time and functioning as a load on the body. The domain is mounted on the lower side by a rigid clamp, setting all displacements on that side to zero in the vertical and horizontal directions. The body in the initial configuration ( $t = t_0$ ) is entirely intact ( $s(x, y) = 1$ , see Fig. 7.24) and without any deformation or external forces. In contrast to the benchmark problem, the following system is halved for efficiency reasons, see Fig. 7.24. Therefore, the computed 2d domain gains the form of a square and a parallel guide on the symmetry axis. Beside the utilization of symmetry, the parameters of the fracture phase field models are altered compared to the original simulation. Thereby, the changed model parameter with the most impact on the analysis is the crack width parameter  $l_c$ , which also defines the exponential shape functions. While the value for the crack width used in the publication is  $l_c = 10^{-1}$ , the exponential shape functions would be computed automatically with parameter  $\delta$  in the exponent of the shape functions in the range from 1.0 to 0.1 for the element sizes used. In order to benefit from the exponential shape function's ability to approximate the crack surface over one element, the parameter  $\delta$  should be at least one. Therefore, in the following model, in the following model, the crack width is reduced significantly to  $l_c = 10^{-3}$ .

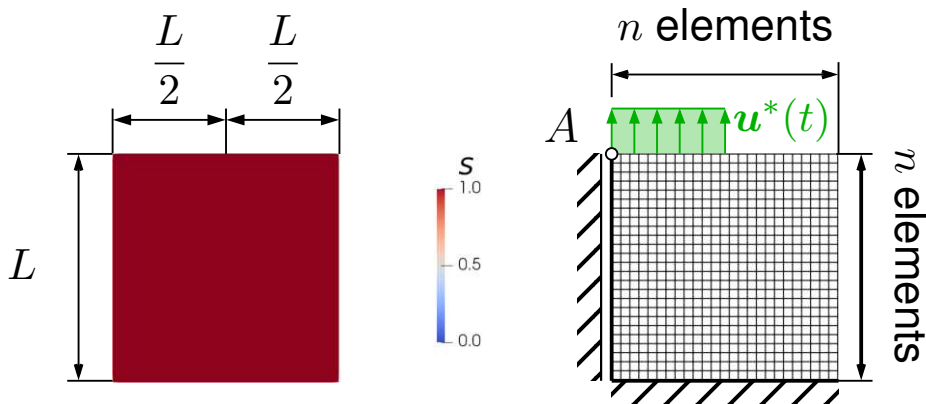


FIGURE 7.24: Load case of the halved peel-off test: contour plot of the initial crack field (left) and finite element mesh with boundary condition (right).

While the model behaviour of halving the domain can be neglected in the evaluation, the smaller crack width influences the result rather significantly. On the one hand, the maximal elastic energy before the emerging of the crack is reduced, and on the other hand, the position of the crack initiation changes. Thereby, the crack doesn't initiate in the bulk but at the transition point of the displacement load  $u^*(t)$  to the unloaded surface on the upper side. The overall crack path stays unchanged and describes a connecting line from the left side to the middle point of the upper side, see Fig. 7.25.

In accordance with the first two tests, the halved peel-off test is carried out with a linear, exponential and adaptive phase field approximation for different mesh densities. The exponential solution is generated in the same manner as explained in the subsection 7.9.1 of Local Exponential Solution. It is the result of an iteration of multiple simulations of the problem with

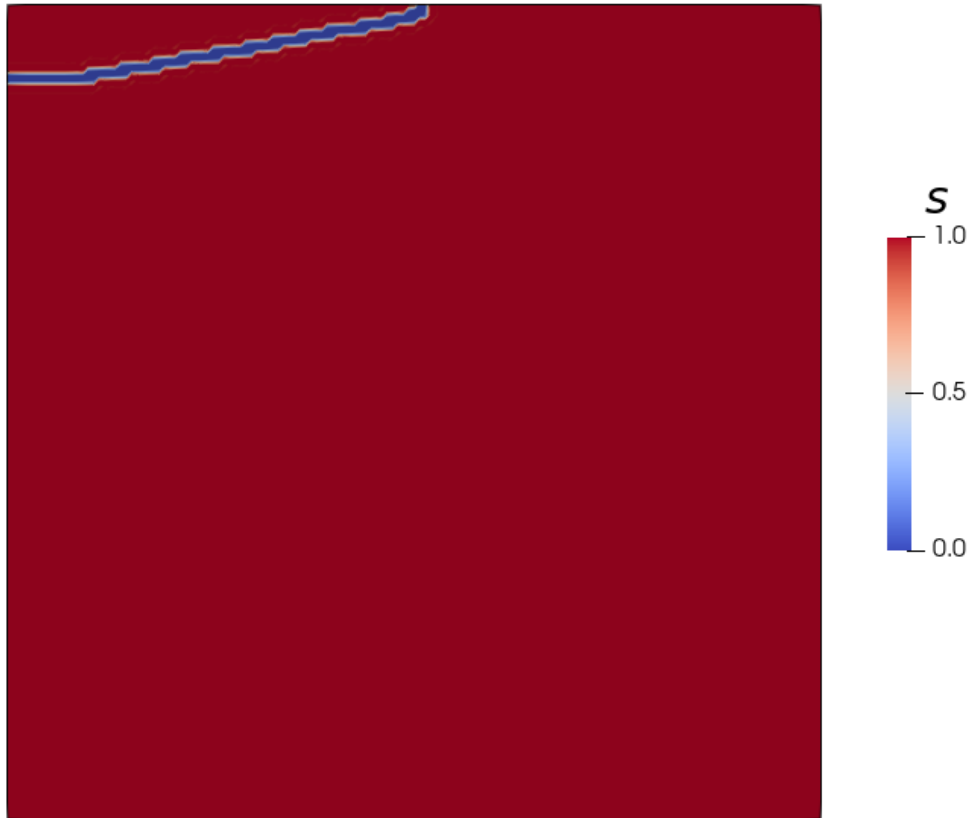


FIGURE 7.25: Halved peel-off test: final crack form ( $150 \times 150$  elements).

adaptive shape functions, which are only allowed to adapt between solution cycles and are repeated until yielding a match between the exponential shape function and the crack surface. The process requires a higher number of iterations with a higher mesh density, equivalent to the shear test. The parameters of the phase field model are adopted from Tab. 6.1 and use a phase field model without a tension-compression split like the tension test to reduce complexity. A reason for the relative higher complexity of the peel-off test compared to the two cases before is the crack curvature. The influence of the approximation of the phase field is depicted in Fig. 7.26. Thereby, the crack in all approximations starts vertically in the middle of the upper side, grows close to the origin boundary side and enters the end of the symmetry boundary horizontally. All approximations (linear, exponential and adaptive) show convergence of crack path. The different approximations don't show an agreement in the  $y$ -position of the end point of the crack. The exponential solution overestimates the position, while the linear solution underestimates the end of the crack compared with the linear solution. Therefore, this leads to crack paths of different lengths. However, the comparison to the reference solution with  $1500 \times 1500$  elements clearly shows that all methods converge to the same crack paths. Furthermore, the adaptive algorithms yields the best results.

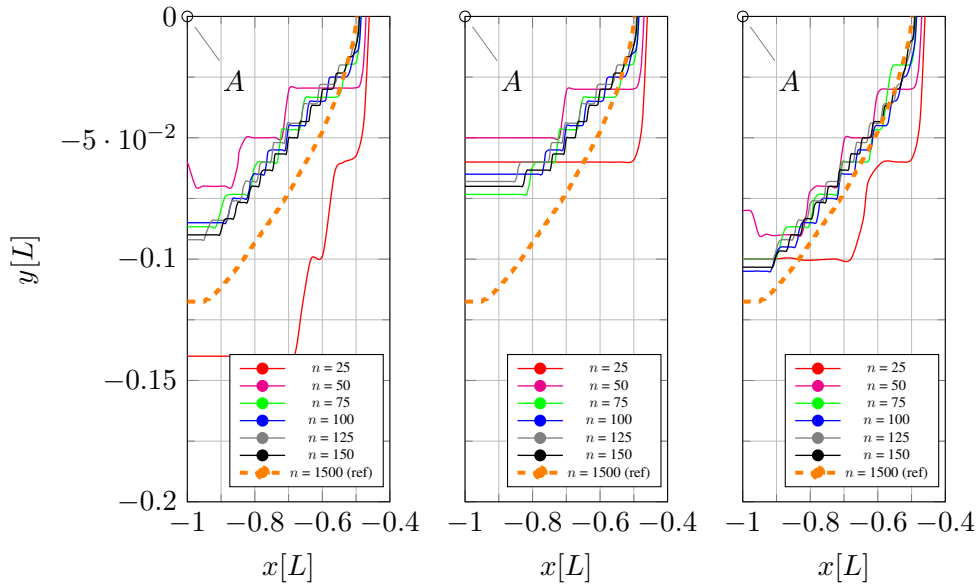


FIGURE 7.26: Crack path of the halved peel-off test with linear/local exponential/adaptive shape functions over the discretization.

Besides the crack path, the elastic energy is discussed, see Fig. 7.27. The elastic energy for different approximations doesn't show the same behaviour as in the two other tests. While in the tension and shear test the elastic energy curve of the adaptive solution lies between the linear and exponential ones, in the peel-off test the adaptive and linear curves are very close and the exponential solutions of the elastic energy are lower. This behaviour could indicate that the adaptive algorithm does not work properly for this example.

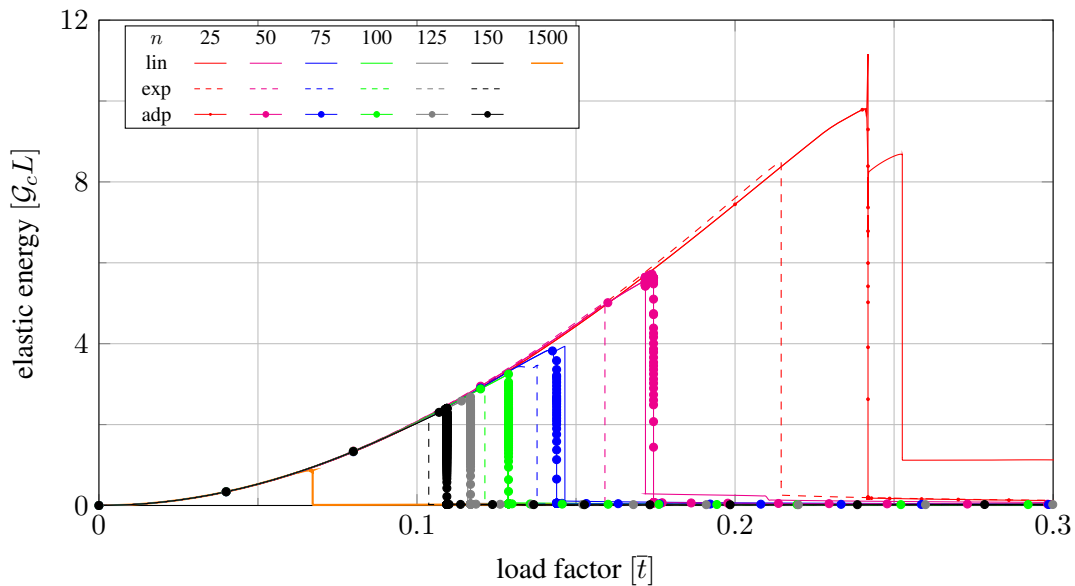


FIGURE 7.27: Elastic energy obtained with linear/local exponential/adaptive shape functions for a peel-off test with a irregular mesh.

Due to the large deviation in the elastic energies, a comparison of the crack depth in the plane of symmetry is preferred. For this purpose, the graph of the error penetration depth is considered, in which the y-position of the crack in the plane of symmetry is plotted against

the mesh size of the number of elements per dimension, see Fig 7.28. The error is computed by considering the solution with  $1500 \times 1500$  linear elements as the exact solution, which most likely yields the results with the highest accuracy under reasonable computing time. The crack depth shows a different picture compared to the elastic energy curves that all solutions show a similar progression in convergence, but the adaptive solution shows higher accuracy even with coarser meshes. The exponential approximation might converge with a higher mesh density towards a different result compared to the linear and adaptive approximations.

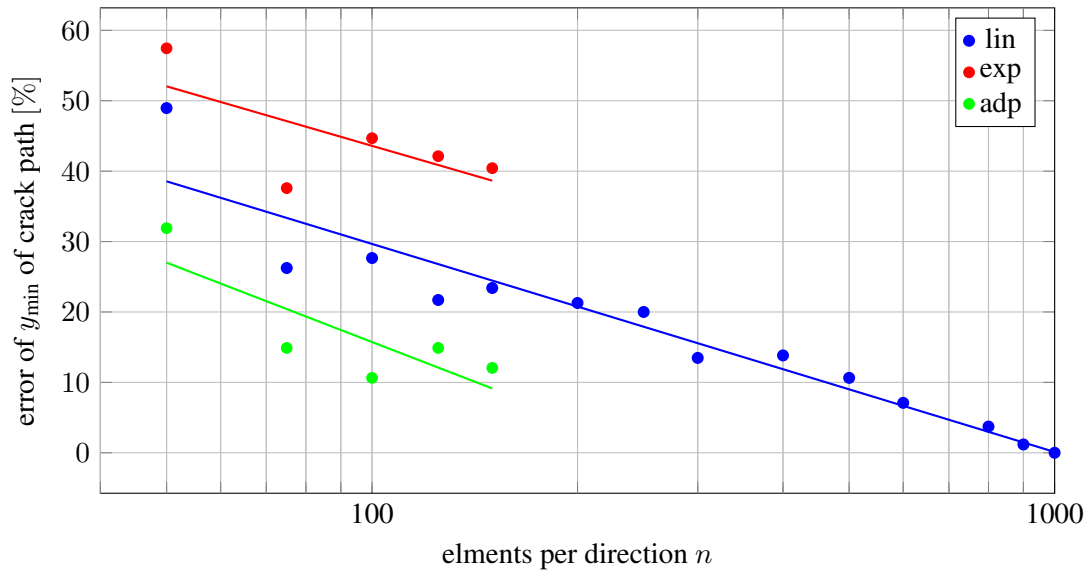


FIGURE 7.28: Error of the crack depth during the halved peel-off test with linear/local exponential/adaptive shape functions over the discretization.

## Chapter 8

# Conclusion and Outlook

The present work investigates an improved approximation for a fracture phase field model by utilizing special shape functions. The model used defines fracture behaviour by an auxiliary field variable called fracture field for linear elasticity in a FEM framework. Further, the fracture field is a smooth field with a high gradient at the crack surfaces, which requires an increased amount of Finite Elements to approximate sufficiently. To circumvent this, Kuhn and Müller [42] employed exponential shape functions with the ability to describe crack surfaces in the 1d space ideally with only one element. Their investigation also provides evidence for the proof of concept in 2d, which showed an improvement in the approximation of the fracture phase field for static cases and multiple crack propagation simulations.

The exponential shape functions, which are at the centre of this work, are straightforward to implement. So, for future work and analysing spatial load cases with exponential shape functions could be implemented and tested in 3d.

Even though an improvement in the approximation of the fracture phase field is at hand, issues arise due to the properties of these special shape functions, which restrict the number of possible fracture problems that can be tackled without further consideration.

Before touching upon the major issue of the exponential shape functions, a comparably minor working point is investigated. This is numerical integration, which is less accurate as a generally used scheme due to the high gradient of the exponential characteristic. Therefore, a different numerical integration scheme in the form of a tanh-sinh quadrature and an adaptive form of the Gauß-Legendre quadrature are tested. Both are adapted in their number of quadrature points, which is the case for a standard linear Lagrange element  $2 \times 2$  in a 2d domain. Additionally, both approaches contain a standard quadrature at elements with an intact phase field, increasing the accuracy only where required. For the Gauß-Legendre quadrature, a rule is defined to choose the number of quadrature points by the ratio of element size  $h$  and regularization width  $l_c$ . Therefore, data curves are fitted to generate third-degree polynomial step functions in the variable  $\delta = h/l_c$ . This approach is effective, and the approximation of the fracture surface reaches an accuracy of 5%. While this approach proves to be an adequate method to improve the accuracy by increasing the number of Gauß points depending on the ratio of crack width to element size  $\delta$ , the quadrature method is less optimal for the numerical integration of exponential functions. Thus, the tanh-sinh quadrature rule is implemented and tested. Although this numerical integration rule is better suited for exponential functions, it requires a minimum of 13 quadrature points per direction to achieve adequate results. This drawback makes it less favorable for elements with an intact phase field for integration and becomes only relevant for meshes with very coarse discretizations.

The main issue of the exponential shape functions is their asymmetrical shape. Unfortunately, this missing property is necessary to approximate crack surfaces correctly, as opposite fracture surfaces have to be symmetric. Therefore, an adaptive scheme is developed and analysed, that orientates exponential shape functions according to their orientation towards

crack surfaces by mirroring the nodal shape functions. In areas with a constant phase field, an orientation is cumbersome, because it requires in the case of an uncracked domain an initial guess or search of the nearest crack surface, which can become more difficult in case of multiple cracks in the same proximity. To avoid ambiguous orientation choices based on lower phase field gradient, linear shape functions are utilized for these areas. This requires blending mixed elements with linear and exponential characteristics at different element edges for the transition of exponential elements at the crack surface and linear elements in constant phase field areas. This ability is implemented in the adaptive algorithm, which not only decides the orientation but also the type of shape functions and has three options a regular exponential, a mirrored exponential or a linear shape function. Thereby, quadrilateral elements are expanded with the adaptive strategy, which enables a variety of element formulations for the fracture phase field approximation from fully linear to exponential and a mixed for the transition elements.

In the static case, the adaptive routine is generally stable and yields good results, but in transient phase field simulation, the choice of shape functions requires multiple iterations for the choice of shape functions for each converged Newton iteration of the degrees of freedom ( $\mathbf{u}$ ,  $s$ ) with a propagated crack. A propagating crack with a moving crack tip also yields difficulties in the choice of an appropriate orientation of the exponential shape functions. So, the exclusion of the crack tip area becomes necessary for a stable computation with the adaptive approach.

For an evaluation of the magnitude of the accuracy increase solution via the adaptive strategy in transient load cases, a "pure" exponential solution is reasonable. Since the crack path is usually unknown in most cases before the computation with a fracture phase field, the approximation by exponential shape functions requires an initial choice. Thereby, the straightforward solution is a computation of the analyzed case study by utilizing linear shape functions for the fracture phase field the first time and then using the phase field of the final step and employing the exponential shape functions according to the gradient. Unfortunately, in a re-run of the same load case with the adapted exponential approximation, the result with the linear approximation does not achieve the same crack path, so the orientation of the exponential shape functions does not incline with the fracture field. As a solution for this mismatch, the process of computation of the load case and adaptation of the exponential shape functions is repeated until congruity is achieved. In a sense, the adaptive routine is compared to an adaptive result based on a loop outside the computation, while the true adaptive routine operates within the simulation process. This is carried out for a shear load case and the peel-off test. The results of the tension, simple shear and peel-off tests are compared in two categories: the crack path, in the case of the tension test because of the absolute congruity, and the elastic energy. The three compared approximations are equal in the approximation of the displacement field and only diverge in the approximation of the phase field by a purely linear, local exponential and adaptive. As expected, the crack paths computed by linear and adaptive shape functions show a higher agreement because the adaptive routine contains functionality, excludes the crack tip for stability reasons, and promotes the crack growth direction of a linear phase field. It also improves the accuracy of the crack surfaces by changing the linear shape functions to exponential shape functions and reducing the required elastic energy for crack propagation. The solutions with the static local exponential approximation decrease the elastic energy even more than the adaptive algorithm, and therefore the adaptive curves of the elastic energy lie between the two other approximations, as might be expected.

To sum up, the exponential shape functions in the form of a mixed shape function containing linear and exponential functions allow a flexible and improved approximation of a fracture phase field transition zone independent of the crack form. An adaptive algorithm, which controls the choice of the element shape functions on each element edge, can compute any propagation but requires an additional restriction of the crack tip area and therefore limits the

advantage of the fracture phase field to avoid tracking of cracks.

The goal of the exponential shape functions in the form of an adaptive strategy can be further expanded with an hp-adaptivity approach to improve not only the crack surface approximation but also the crack form, which by implication is the case for exponential shape functions. They are only useful for coarse meshes, which then reduce the number of possible crack sets, i.e. crack paths. The adaptive algorithm is technically sophisticated and could benefit from a more advanced crack tip finder algorithm and interpolated adaptive shape functions with linear and exponential characteristics. From the technical aspect of computer science, it seems the machine learning aspect in the form of an adaptive numerical integration scheme specially tailored for the exponential elements would be an interesting test field.



# Bibliography

- [1] H. Altenbach. *Kontinuumsmechanik: Einführung in die materialunabhängigen und materialabhängigen Gleichungen*. Springer, 2012.
- [2] M. Ambati, T. Gerasimov, and L. De Lorenzis. “Phase-field modeling of ductile fracture”. In: *Computational Mechanics* 55 (2015), pp. 1017–1040.
- [3] M. Ambati, T. Gerasimov, and L. Lorenzis. “A review on phase-field models of brittle fracture and a new fast hybrid formulation”. In: *Computational Mechanics* 55 (2015), 383–405.
- [4] L. Ambrosio and V. M. Tortorelli. “Approximation of functional depending on jumps by elliptic functional via t-convergence”. In: *Communications on Pure and Applied Mathematics* 43 (1990), pp. 999–1036.
- [5] H. Amor, J.-J. Marigo, and C. Maurini. “Regularized formulation of the variational brittle fracture with unilateral contact: Numerical experiments”. In: *Journal of the Mechanics and Physics of Solids* 57 (2009), pp. 1209–1229.
- [6] M. Artina, M. Fornasier, S. Micheletti, and S. Perotto. “Anisotropic Mesh Adaptation for Crack Detection In Brittle Materials”. In: *SIAM Journal on Scientific Computing* 37 (2015), pp. 633–659.
- [7] I. Babuška and A. Miller. “A feedback finite element method with a posteriori error estimation: Part I. The finite element method and some basic properties of the a posteriori error estimator”. In: *Computer Methods in Applied Mechanics and Engineering* 61 (1987), pp. 1–40.
- [8] K. Bathe. *Finite Element Procedures*. Prentice Hall, 2007.
- [9] W. Becker and D. Gross. *Mechanik elastischer Körper und Strukturen*. Springer, 2002.
- [10] T. Belytschko and T. Black. “Elastic crack growth in finite elements with minimal remeshing”. In: *International Journal for Numerical Methods in Engineering* 45 (1999), pp. 601–620.
- [11] W. J. Boettinger, J. A. Warren, C. Beckermann, and A. Karma. “Phase-Field Simulation of Solidification”. In: *Annual Review of Materials Research* 32 (2002), pp. 163–194.
- [12] M. J. Borden, T. J. Hughes, C. M. Landis, and C. V. Verhoosel. “A higher-order phase-field model for brittle fracture: Formulation and analysis within the isogeometric analysis framework”. In: *Computer Methods in Applied Mechanics and Engineering* 273 (2014), pp. 100–118.
- [13] M. J. Borden, C. V. Verhoosel, M. A. Scott, T. J. Hughes, and C. M. Landis. “A phase-field description of dynamic brittle fracture”. In: *Computer Methods in Applied Mechanics and Engineering* 217-220 (2012), pp. 77–95.
- [14] B. Bourdin. “The variational formulation of brittle fracture: Numerical implementation and extensions”. In: *IUTAM Symposium on Discretization Methods for Evolving Discontinuities*. 2007, pp. 381–393.
- [15] B. Bourdin, G. Francfort, and J.-J. Marigo. “Numerical experiments in revisited brittle fracture”. In: *Journal of the Mechanics and Physics of Solids* 48 (2000), pp. 797–826.

- [16] S. Burke, C. Ortner, and E. Süli. “An Adaptive Finite Element Approximation of a Variational Model of Brittle Fracture”. In: *SIAM Journal on Numerical Analysis* 48 (2010), pp. 980–1012.
- [17] L. Chen, B. Li, and R. de Borst. “Adaptive isogeometric analysis for phase-field modeling of anisotropic brittle fracture”. In: *International Journal for Numerical Methods in Engineering* 121 (2020), pp. 4630–4648.
- [18] J. Chessa, H. Wang, and T. Belytschko. “On construction of blending elements for local partition of unity enriched finite elements”. In: *International Journal for Numerical Methods in Engineering* 57 (2003), pp. 1015–1038.
- [19] B. Coleman and M. Gurtin. “Thermodynamics with Internal State Variables”. In: *The Journal of Chemical Physics* 47 (1967), pp. 597–613.
- [20] F. Dammaß, M. Ambati, and M. Kästner. “A unified phase-field model of fracture in viscoelastic materials”. In: *Continuum Mechanics and Thermodynamics* 33 (2021), pp. 1907–1929.
- [21] L. De Lorenzis and T. Gerasimov. “Numerical Implementation of Phase-Field Models of Brittle Fracture”. In: *Modeling in Engineering Using Innovative Numerical Methods for Solids and Fluids*. Springer, 2020, pp. 75–101.
- [22] G. Del Piero, G. Lancioni, and R. March. “A variational model for fracture mechanics: Numerical experiments”. In: *Journal of the Mechanics and Physics of Solids* 55 (2007), pp. 2513–2537.
- [23] F. Duda, A. Ciarbonetti, P. Sánchez, and A. Huespe. “A phase-field/gradient damage model for brittle fracture in elastic–plastic solids”. In: *International Journal of Plasticity* 65 (2015), 269–296.
- [24] L. O. Eastgate, J. P. Sethna, M. Rauscher, T. Cretegnny, C.-S. Chen, and C. R. Myers. “Fracture in mode I using a conserved phase-field model”. In: *Physical Review E* 65 (2002), p. 036117.
- [25] F. Erdogan and G. Sih. “On the Crack Extension in Plates Under Plane Loading and Transverse Shear”. In: *Journal of Basic Engineering* 85 (1963), 519–525.
- [26] G. Francfort and J.-J. Marigo. “Revisiting brittle fracture as an energy minimization problem”. In: *Journal of The Mechanics and Physics of Solids* 46 (1998), pp. 1319–1342.
- [27] T.-P. Fries and T. Belytschko. “The extended/generalized finite element method: An overview of the method and its applications”. In: *International Journal for Numerical Methods in Engineering* 84 (2010), pp. 253–304.
- [28] T. Gerasimov and L. De Lorenzis. “On penalization in variational phase-field models of brittle fracture”. In: *Computer Methods in Applied Mechanics and Engineering* 354 (2019), pp. 990–1026.
- [29] T. Gerasimov, U. Römer, J. Vondrejč, H. Matthies, and L. De Lorenzis. “Stochastic phase-field modeling of brittle fracture: Computing multiple crack patterns and their probabilities”. In: *Computer Methods in Applied Mechanics and Engineering* 372 (2020), p. 113353.
- [30] A. A. Griffith. “The phenomena of rupture and flows in solids”. In: *Philosophical Transactions of the Royal Society of London* 221 (1921), 163–198.
- [31] D. Gross and T. Seelig. *Fracture Mechanics: With an Introduction to Micromechanics*. Springer, 2011.
- [32] A. Gupta, M. Krishnan, T. Mandal, R. Chowdhury, and V. P. Nguyen. “An adaptive mesh refinement algorithm for phase-field fracture models: Application to brittle, cohesive, and dynamic fracture”. In: *Computer Methods in Applied Mechanics and Engineering* 399 (2022), p. 115347.
- [33] M. E. Gurtin. *An Introduction to Continuum Mechanics. Mathematics in Science and Engineering*. Academic Press, 1981.

- [34] M. E. Gurtin. “Generalized Ginzburg-Landau and Cahn-Hilliard Equations Based on a Microforce Balance”. In: *Physica D* 92 (1996), 178–192.
- [35] T. Heister, M. F. Wheeler, and T. Wick. “A primal-dual active set method and predictor-corrector mesh adaptivity for computing fracture propagation using a phase-field approach”. In: *Computer Methods in Applied Mechanics and Engineering* 290 (2015), pp. 466–495.
- [36] G. Holzapfel. *Nonlinear solid mechanics: a continuum approach for engineering*. Wiley, 2000.
- [37] T. Hughes. *The Finite Element Method: Linear Static and Dynamic Finite Element Analysis*. Dover Publications, Inc., Mineola, New York, 2000.
- [38] G. R. Irwin. “Analysis of stresses and strains near the end of a crack traversing a plate.” In: *Journal of Applied Mechanics* 24 (1957), 361–364.
- [39] J. Kiendl, M. Ambati, L. De Lorenzis, H. Gomez, and A. Reali. “Phase-field description of brittle fracture in plates and shells”. In: *Computer Methods in Applied Mechanics and Engineering* 312 (2016), pp. 374–394.
- [40] C. Kuhn. “Numerical and Analytical Investigation of a Phase Field Model for Fracture”. PhD thesis. Technische Universität Kaiserslautern, 2013.
- [41] C. Kuhn and R. Müller. “A continuum phase field model for fracture”. In: *Engineering Fracture Mechanics* 77 (2010), pp. 3625–3634.
- [42] C. Kuhn and R. Müller. “A new finite element technique for a phase field model of brittle fracture”. In: *Journal of Theoretical and Applied Mechanics* 49 (2011), pp. 1115–1133.
- [43] C. Kuhn and R. Müller. “Exponential Finite Elements for a Phase Field Fracture Model”. In: *PAMM* 10 (2010), pp. 121–122.
- [44] C. Kuhn, T. Noll, D. Olesch, and R. Müller. “Phase Field Modeling of Brittle and Ductile Fracture”. In: *Non-standard Discretisation Methods in Solid Mechanics*. Springer, 2022, pp. 283–325.
- [45] M. Kuna. *Finite Elements in Fracture Mechanics: Theory - Numerics - Applications*. Springer, 2013.
- [46] S. LaZghab, T. Aukrust, and K. Holthe. “Adaptive exponential finite elements for the shear boundary layer in the bearing channel during extrusion”. In: *Computer Methods in Applied Mechanics and Engineering* 191 (2002), pp. 1113–1128.
- [47] Y. Li, L. Wenyu, and Y. Shen. “Variational h-adaption method for the phase field approach to fracture”. In: *International Journal of Fracture* 217 (2019), 83–103.
- [48] Y.-S. Lo, M. J. Borden, K. Ravi-Chandar, and C. M. Landis. “A phase-field model for fatigue crack growth”. In: *Journal of the Mechanics and Physics of Solids* 132 (2019), p. 103684.
- [49] K. Mang, M. Walloth, T. Wick, and W. Wollner. “Mesh adaptivity for quasi-static phase-field fractures based on a residual-type a posteriori error estimator”. In: *GAMM-Mitteilungen* 43 (2020), e202000003.
- [50] C. Miehe, F. Welschinger, and M. Hofacker. “Thermodynamically consistent phase-field models of fracture: Variational principles and multi-field FE implementations”. In: *International Journal for Numerical Methods in Engineering* 83 (2010), pp. 1273–1311.
- [51] C. Miehe, F. Aldakheel, and A. Raina. “Phase field modeling of ductile fracture at finite strains: A variational gradient-extended plasticity-damage theory”. In: *International Journal of Plasticity* 84 (2016), pp. 1–32.
- [52] C. Miehe, M. Hofacker, and F. Welschinger. “A phase field model for rate-independent crack propagation: Robust algorithmic implementation based on operator splits”. In: *Computer Methods in Applied Mechanics and Engineering* 199 (2010), pp. 2765–2778.

- [53] N. Moës, J. Dolbow, and T. Belytschko. “A finite element method for crack growth without remeshing”. In: *International Journal for Numerical Methods in Engineering* 46 (1999), pp. 131–150.
- [54] A. Muixí, S. Fernández-Méndez, and A. Rodríguez-Ferran. “Adaptive refinement for phase-field models of brittle fracture based on Nitsche’s method”. In: *Computational Mechanics* 66 (2020), pp. 1–17.
- [55] D. Mumford and J. Shah. “Optimal approximations by piecewise smooth functions and associated variational problems”. In: *Communications on Pure and Applied Mathematics* 42 (1989), pp. 577–685.
- [56] S. Nagaraja, M. Elhaddad, M. Ambati, S. Kollmannsberger, L. De Lorenzis, and E. Rank. “Phase-field modeling of brittle fracture with multi-level hp-FEM and the finite cell method”. In: *Computational Mechanics* 63 (2019), 1283–1300.
- [57] T. Noll. “A Phase Field Model for Ductile Fracture”. PhD thesis. Technische Universität Kaiserslautern, 2022.
- [58] D. Olesch, C. Kuhn, A. Schlüter, and R. Müller. “Adaptive Exponential Finite Elements for a Phase Field Fracture Model”. In: *PAMM* 21 (2021), e202100077.
- [59] D. Olesch, C. Kuhn, A. Schlüter, and R. Müller. “Adaptive numerical integration of exponential finite elements for a phase field fracture model”. In: *Computational Mechanics* 67 (2021), pp. 811–821.
- [60] D. Olesch, C. Kuhn, A. Schlüter, and R. Müller. “Adaptive Orientation of Exponential Finite Elements for a Phase Field Fracture Model”. In: *PAMM* 20 (2021), e202000140.
- [61] D. Phansalkar, K. Weinberg, M. Ortiz, and S. Leyendecker. “A spatially adaptive phase-field model of fracture”. In: *Computer Methods in Applied Mechanics and Engineering* 395 (2022), p. 114880.
- [62] A. Roberto and F. Francesecco. “Phase-field modelling of failure in hybrid laminates”. In: *Composite Structures* 181 (2017), pp. 9–25.
- [63] M. Sabel, C. Sator, and R. Müller. “A particle finite element method for machining simulations”. In: *Computational Mechanics* 54 (2014), pp. 267–307.
- [64] A. Schlüter. “Phase Field Modeling of Dynamic Brittle Fracture”. PhD thesis. Technische Universität Kaiserslautern, 2018.
- [65] R. Schmitt, C. Kuhn, R. Müller, and K. Bhattacharya. “Crystal Plasticity and Martensitic Transformations - A Phase Field Approach”. In: *Technische Mechanik* 34 (2014), pp. 23–38.
- [66] D. Schrade, R. Mueller, B. Xu, and D. Gross. “Domain evolution in ferroelectric materials: A continuum phase field model and finite element implementation”. In: *Computer Methods in Applied Mechanics and Engineering* 196 (2007), pp. 4365–4374.
- [67] C. Schreiber. “Phase Field Modeling of Fracture: Fatigue and Anisotropic Fracture Resistance”. PhD thesis. Technische Universität Kaiserslautern, 2021.
- [68] J. Schröder et al. “A Selection of Benchmark Problems in Solid Mechanics and Applied Mathematics”. In: *Archives of Computational Methods in Engineering* 28 (2021), pp. 713–751.
- [69] C. Steinke. “On the numerical approximation of brittle fracture evolution at impact loading and realistic post-fracture behavior by the phase-field method”. PhD thesis. Technische Universität Dresden, 2020.
- [70] N. Sukumar, N. Moës, B. Moran, and T. Belytschko. “Extended finite element method for three-dimensional crack modelling”. In: *International Journal for Numerical Methods in Engineering* 48 (2000), pp. 1549–1570.
- [71] H. Takahasi and M. Mori. “Double Exponential Formulas for Numerical Integration”. In: *Publications of the Research Institute for Mathematical Sciences* 9 (1974), 721–741.
- [72] R. L. Taylor. *FEAP—a finite element analysis program*. 2014.

- [73] R. Verfürth. *A posteriori error estimation and adaptive mesh-refinement techniques for Finite Element Methods*. Oxford University Press, 2013.
- [74] M. Walloth and W. Wollner. “A Posteriori Estimator for the Adaptive Solution of a Quasi-Static Fracture Phase-Field Model with Irreversibility Constraints”. In: *SIAM Journal on Scientific Computing* 44 (2022), pp. 479–505.
- [75] K. Weinberg and C. Hesch. “A high-order finite deformation phase-field approach to fracture”. In: *Continuum Mechanics and Thermodynamics* 29 (2015), pp. 935–945.
- [76] P. Wriggers. *Nonlinear Finite Element Methods*. Springer, 2008.
- [77] C. Wu. “Maximum-energy-release-rate criterion applied to a tension-compression specimen with crack”. In: *Journal of Elasticity* 8 (1978), pp. 235–257.
- [78] N. D. Zander. “Multi-level hp-FEM: dynamically changing high-order mesh refinement with arbitrary hanging nodes”. PhD thesis. Technische Universität München, 2017.
- [79] O. Zienkiewicz, R. Taylor, and J. Zhu. *The Finite Element Method: Its Basis and Fundamentals*. Butterworth-Heinemann, 2013.

# Curriculum Vitae

Name: Darius Matthias Olesch  
Geburtsort: Landshut

---

1996 - 2001	Karl-Heiß-Volksschule Landshut
2001 - 2007	Staatliche Realschule Landshut
2007 - 2009	Staatliche Fachoberschule Landshut
03.2007-05.2010	Bachelorstudium in Maschinenbau an der Hochschule Landshut  Bachelorarbeit: <i>Experimentelle und numerische Analyse des Beulverhaltens hybrider Hohlprofile</i>  Abschluss: Bachelor of Engineering
10.2010 - 04.2013	Masterstudium in Leichtbau und Simulation an der Hochschule Landshut  Masterarbeit: <i>Numerische Analyse der Relaxation von Kontaktsystemen</i>  Abschluss: Master of Engineering
01.2018 - 12.2022	Wissenschaftlicher Mitarbeiter am Lehrstuhl für Technische Mechanik, Fachbereich Maschinenbau und Verfahrenstechnik, der Technischen Universität Kaiserslautern